UNIVERSITY OF CALGARY

Processing and Interpretation of Time-lapse Vertical Seismic Profile Data from the Penn West CO_2 Monitoring Project

by

Marcia L. Couëslan

A THESIS

SUBMITTED TO THE FACULTY OF GRADUATE STUDIES

IN PARTIAL FULFILMENT OF THE REQUIREMENTS FOR THE

DEGREE OF MASTER OF SCIENCE

DEPARTMENT OF GEOLOGY AND GEOPHYSICS

CALGARY, ALBERTA

APRIL 2007

UNIVERSITY OF CALGARY

FACULTY OF GRADUATE STUDIES

The undersigned certify that they have read, and recommend to the Faculty of Graduate Studies for acceptance, a thesis entitled " Processing and Interpretation of Time-lapse Vertical Seismic Profile Data From The Penn West CO_2 Monitoring Project" submitted by Marcia L. Couëslan in partial fulfilment of the requirements of the degree of Master of Science.

Supervisor, Dr. D. C. Lawton
Department of Geology and Geophysics

Dr. R. R. Stewart
Department of Geology and Geophysics

Dr. Y. E. Martin
Department of Geography

Date

ABSTRACT

At the Penn West CO_2 Pilot Project in Central Alberta, CO_2 is being injected into the Cardium Formation at a depth of 1620 m in the Pembina Oil Field for enhanced recovery and carbon storage purposes. The reservoir is being monitored using simultaneously acquired time-lapse multicomponent surface and vertical seismic profile (VSP) surveys. These provide lateral coverage of the survey area as well as high-resolution images near the observation well. The baseline survey was acquired in March 2005 prior to CO_2 injection, and the first monitor survey was acquired in December 2005. Both the P-wave and Sv-wave VSP images show excellent ties with the P-wave surface seismic data and have higher frequency bandwidth and resolution. Comparisons between the baseline and monitor borehole seismic surveys show an increase in reflectivity at the reservoir, and crosscorrelations show a time shift of 0.2 ms at the base of the reservoir on one of the walkaway lines.

ACKNOWLEDGEMENTS

I would like to thank the following people for their people for their support over the past 2.5 years. Without their help, I could not have completed this work.

- Thank-you to my supervisor, Dr. Don Lawton, for asking me to work on this important project and for giving me so many opportunities to present my work at an international level. The experience has been invaluable and has given me a sound footing for my career in CCS.

- Scott Leaney for taking the time to teach a fellow Manitoban about wavefield separation techniques, anisotropy analysis, reference recommendations, and how to use Avolog because the instruction manual doesn't do it justice.

- Schlumberger Canada for finding me a space in their office and a computer to work on the VSP data. Access to their software and technical support has been critical to the success of this project.

- Richard Gray at WesternGeco for taking pity on me and helping with the repeatability metrics and cross-equalization.

- Mike Jones for his innumerable technical discussions, valuable advice on presentation skills – despite sleeping through some of them – and for his general interest in my intellectual well-being.

- Louis Chabot and Dwayne Sparks at Penn West Petroleum for all of their assistance and support.

- My CO_2 buddy, Mark Raistrick, for the company on conferences and endless conversations on our favourite topic. We can be really boring at a party.

- To all of my friends in the department, office mates, and those on their high horses for the drinks on Friday nights, skiing on the weekends, the complaints, and the laughter. You've made it a more interesting journey. Shine shine.

I would also like to thank the following organizations for their financial support and for their support of the Penn West Project: CREWES, Alberta Energy Research Institute (AERI), Natural Resources Canada (NRCAN), Western Economic Diversification (WED), and Penn West Petroleum.

DEDICATION

For my husband and family, Richard, Mom, Dad, Aimee, Franz, and Chris. Without their love and support, I couldn't have done this.

TABLE OF CONTENTS

LIST OF TABLES

LIST OF FIGURES

LIST OF SYMBOLS, ABBREVIATIONS, AND NOMENCLATURE

Symbol	Definition
VSP	Vertical seismic profile
EOR	Enhanced oil recovery
EHR	Enhanced hydrocarbon recovery
ECBM	Enhanced coalbed methane
WCSB	Western Canadian Sedimentary Basin
CCS	Carbon Capture and Storage
V_p	P-wave velocity
V_s	Shear-wave velocity
K	Bulk Modulus
μ	Shear Modulus
λ	Lamé constant
NRMS	Normalized root mean square
CMP	Common midpoint
TD	Total depth
PWD	Parametric wavefield decomposition
NMO	Normal moveout
AVO	Amplitude variation with offset
TI	Transverse isotropy
VTI	Vertical transverse isotropy
HTI	Horizontal transverse isotropy

EPIGRAPH

Never doubt that a small, group of thoughtful, committed citizens can change the world.
Indeed, it is the only thing that ever has.

~Margaret Mead

Chapter One: Introduction

1.1 Introduction

Many of the oil and gas fields in the Western Canadian Sedimentary Basin (WCSB) are mature and have been depleted through primary production and secondary recovery methods such as waterflooding. However, water resources are becoming a more contentious issue in Alberta due water shortages caused by drought and the increasing demand for this resource from a number of sectors. Oil and gas companies are now investigating new methods, such as CO_2 flooding, to further enhance oil and gas recovery in the province. Alberta is the largest CO_2 producer in the country in part because of the accelerating oil sands development in the province. It may be possible to increase hydrocarbon production by capturing CO_2 emissions from industrial facilities and injecting the CO_2 into hydrocarbon reservoirs.

Bachu and Shaw (2004) estimate that CO_2 flooding can increase oil recovery by 7 to 23% of the original oil in place (OOIP). CO_2 injection for enhanced oil recovery (EOR) also has the potential benefit of CO_2 storage, which reduces greenhouse gas emissions into the atmosphere. They have also predicted that Western Canada has a practical CO_2 storage capacity of about 3.3 Gt in its oil and gas reservoirs; 450 Mt of this capacity could be from CO_2 enhanced recovery. However, in order to claim a reduction in CO_2 emissions and claim any potential royalty credits, the injected CO_2 must be monitored to prove that it is being trapped in these reservoirs.

In the last five to ten years, time-lapse seismic data has been increasingly used to monitor production-related changes in oil and gas fields. It can be used to monitor activities such as pressure depletion due to production, fluid injection, connectivity within the reservoir, and leakage in the overburden. Time-lapse seismic data has become a powerful tool for monitoring and verification of CO_2 storage at a number of sites around the world. Time-lapse surface seismic and VSP surveys have been successfully used to monitor injected CO_2 in Encana's Weyburn Field (Li, 2003), Anadarko's Patrick

Draw Field (O'Brien et al., 2004), and the Sleipner Project in the North Sea (Chadwick et al., 2006).

1.2 The Penn West CO_2 Injection Project

1.2.1 Field Background

The Pembina Oil Field is the largest onshore oil field in North America and has been in production since the 1950s (Figure 1.1). The Pembina Field has an area of approximately 3000 km^2 and an estimated OOIP of 118 million m^3 (Krause et al., 1987). Waterflooding was initiated early in the life of the field as a secondary recovery method. The peak oil production occurred between the years of 1970-72, and oil production rates are now in decline across the field. The field is a good candidate for further enhanced recovery because the recovery factor after waterflooding is still only 20% (Krause et al., 1987).

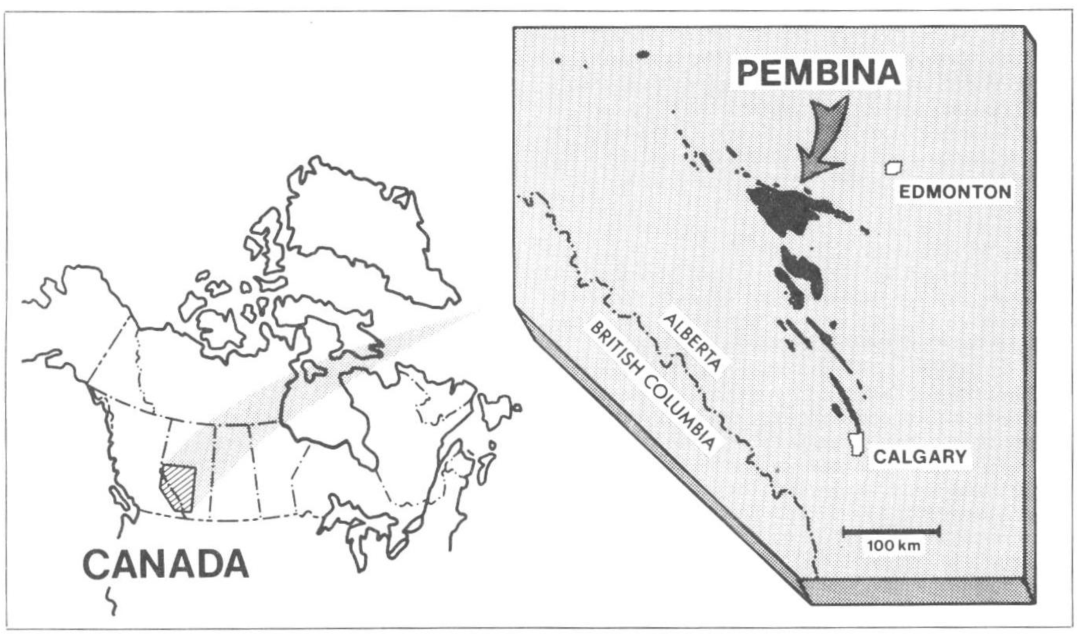

Figure 1.1: Location of the Pembina Oil Field in central Alberta (from Krause et al., 1987).

The Penn West CO_2 Injection Project site is located 100 km southwest of Edmonton, Alberta in the Pembina Oil Field. At this site, CO_2 is being injected into the Cardium Formation for enhanced recovery and carbon storage purposes.

1.2.2 Geology

The Cretaceous-aged Cardium Formation is the main reservoir rock in the Pembina Oil Field containing 82% of the OOIP (Krause et al., 1987). The Cardium Formation can be separated into two separate lithologic units: the Cardium Zone Member and the Pembina River Member. The Cardium Zone Member is characterized by capping siltstones and shales while the Pembina River Member contains the reservoir rocks. The Pembina River Member consists of one conglomerate unit and two or three sandstone units depending upon the location in the field. All of the units have variable permeabilities across the field: 160 md for the conglomerate, 17 md for the upper sandstone, and 2 md for the middle sandstone (Krause et al., 1987). Injected fluids tend to channel through the conglomerates because it is the high permeability layer (Krause et al., 1987). The shale baffle between the conglomerate and the upper sandstone is not always laterally continuous; hence the conglomerate also has a high potential to act as a thief zone in EOR operations.

At the Penn West site, the Cardium Formation has a total thickness of about 20 m and is located at a depth of about 1650 m. It is sandwiched by the marine shales of the Wapiabi Formation and the Blackstone Formation (Figure 1.2). The sandstone units are separated by shale stringers that may limit communication between the units. Figure 1.3 displays the well logs from a production well about 60 m from the observation well for the project and three synthetic seismograms that were generated with filters of varying frequency bandwidth. The reservoir temperature and pressure are $50^{o}C$ and ~19MPa respectively. At this temperature and pressure, the injected supercritical CO_2 will remain in a supercritical state in the reservoir. Supercritical CO_2 has the density of a fluid but expands to fill void space and diffuses through solids like a gas (http://en.wikipedia.org/wiki/Supercritical_carbon_dioxide).

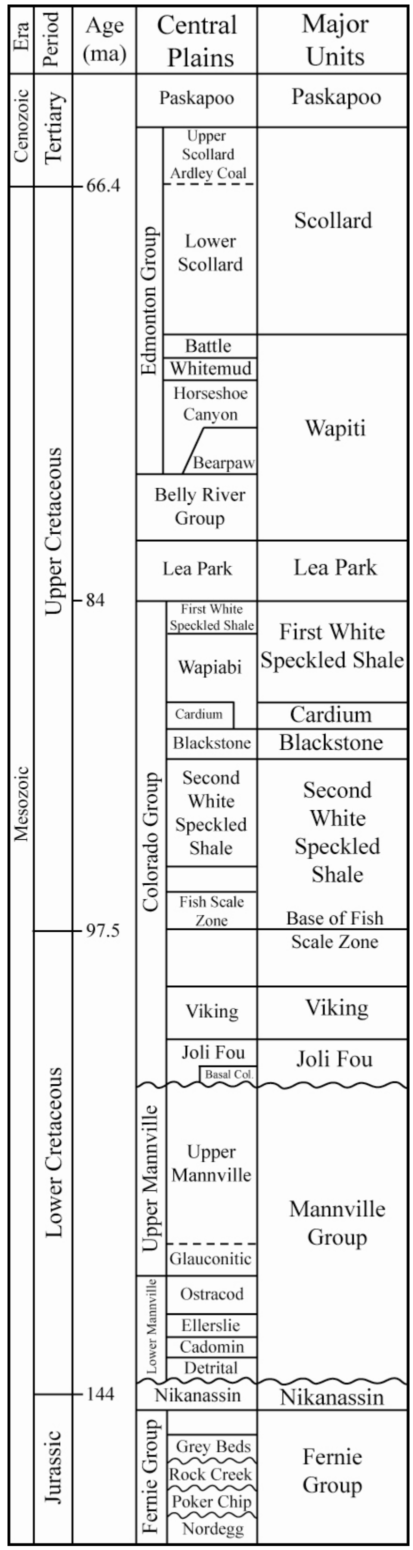

Figure 1.2: Stratigraphic column for the Penn West project (modifed from AEUB, 2002).

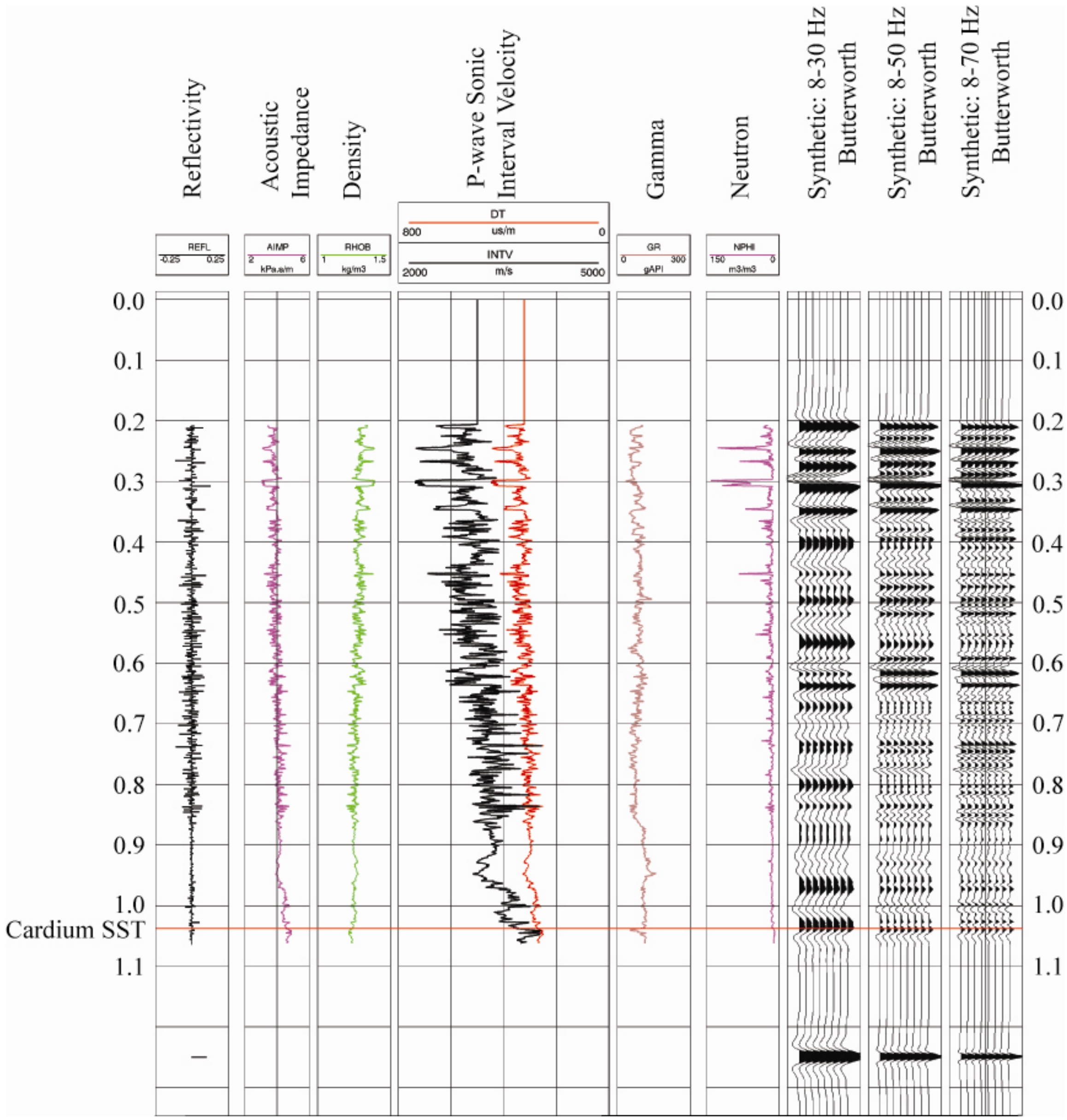

Figure 1.3: Well logs from the nearby production well and synthetic seismograms.

The dominant fracture trend in the area is northeast-southwest (Krause et al., 1987). Bell and Bachu (2003) have determined the stress orientations in the Alberta Basin based on breakouts in well bores, hydraulic fracture axes, and leak-off pressures. The principle horizontal stress direction in the Upper Cretaceous formations is oriented in a northeast-southwest direction (Figure 1.4). Natural and induced hydraulic fractures will align parallel to the principle stress direction.

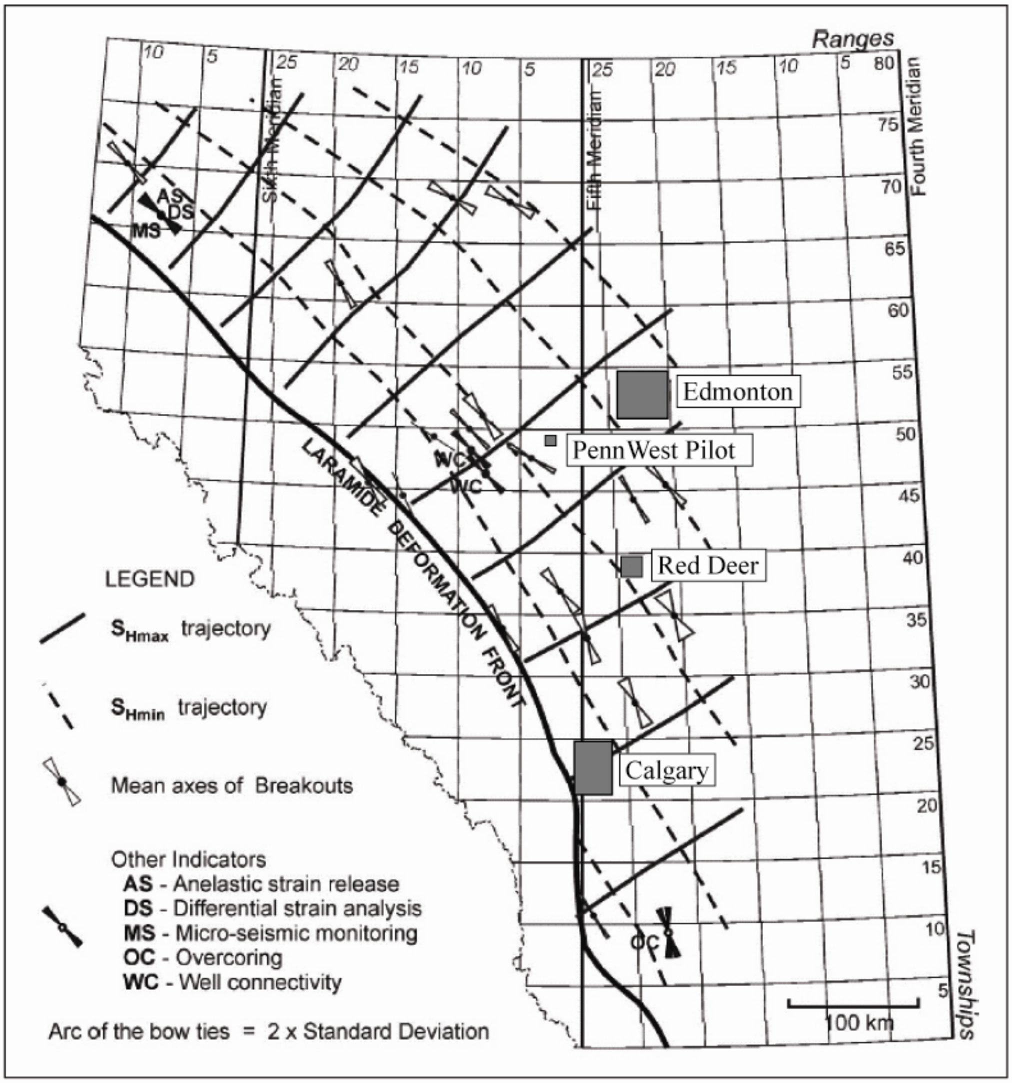

Figure 1.4: Minimum and maximum stress orientations for the Upper Cretaceous rocks in Alberta (from Bell and Bachu, 2003).

The Cardium Formation is a low impedance-contrast reservoir, and the top and base of the reservoir appear as a weakly tuned event in typical seismic data. As a result, exploration in the Pembina Oil Field has historically been driven by well logging and geologic interpretations rather than seismic surveys.

1.2.3 Monitoring Program and Well Instrumentation

Carbon capture and storage (CCS) projects require diverse monitoring programs in order to verify that the CO_2 is being trapped in a storage formation. Penn West Petroleum provided access to an old production well that had been refurbished for use as an observation well for the monitoring program (Figure 1.5). In February 2005, eight three-component geophones, six pressure and temperature sensors, and two fluid sampling ports were cemented into the well near reservoir depths. The geophones were oriented in the same direction when they were strapped to the well casing. However, the geophones were still able to rotate as the casing was lowered into the well, so the exact orientation of each geophone within the well was unknown. The geophones are located between 1497 and 1640 m depth with a 20 m vertical spacing (Figure 1.6); only one geophone is located in the reservoir itself. The pressure-temperature sensors and fluid sampling ports are located in the reservoir and at the top of the Wapiabi Formation.

The monitoring program consists of three main components: geophysical, geochemical, and the pressure-temperature measurements. The pressure-temperature sensors are in place to monitor pressure and temperature changes in the reservoir during CO_2 injection and to monitor changes that may occur in the overburden due to CO_2 leakage up the well. A group at the University of Alberta is analyzing pressure-temperature data. The sampling tubes allow the fluids in the reservoir and in the Wapiabi Formation to be collected and analyzed for ions related to the CO_2 injection. Fluid samples are also being acquired and analyzed from the production wells surrounding the CO_2 injector (Figure 1.5). The geochemical sampling and analysis is being completed at the University of Calgary and the Alberta Research Council (ARC).

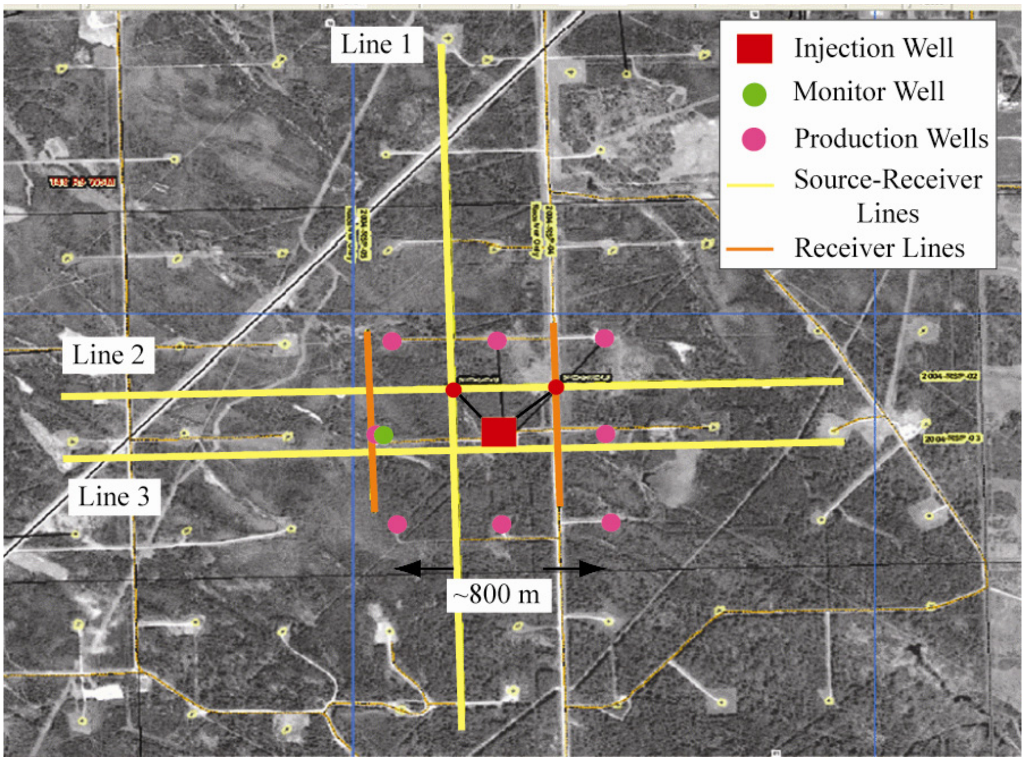

Figure 1.5: Aerial view of the Penn West CO_2 injection site.

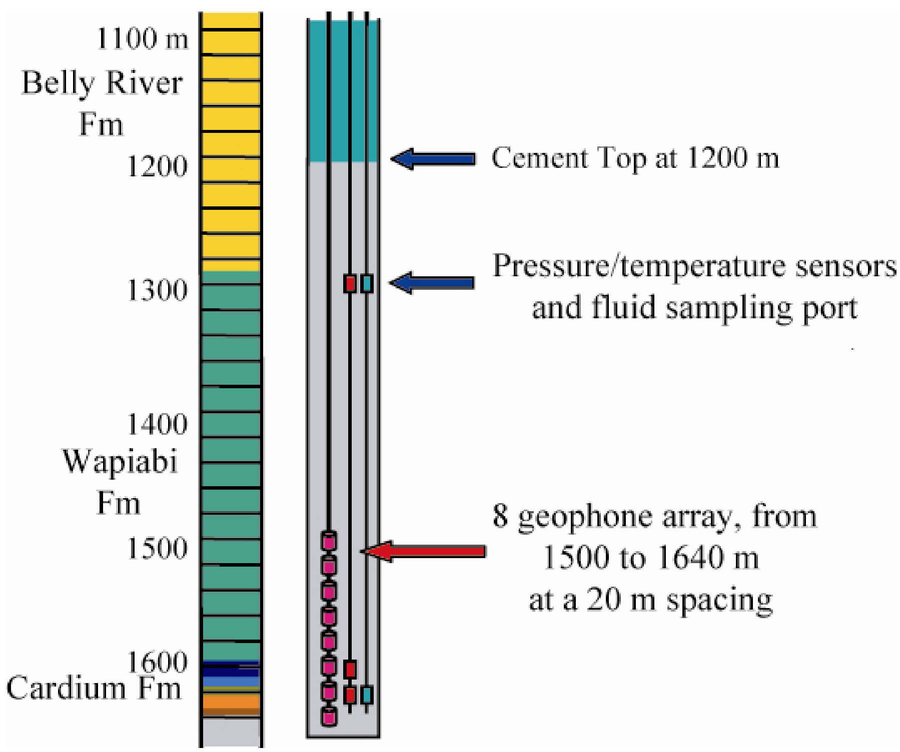

Figure 1.6: Instrumentation in the monitor well (Courtesy of R. Chalaturnyk).

The geophysical monitoring consists of simultaneously acquired time-lapse multicomponent surface seismic and VSP surveys. One of the objectives of the project was to use a series of 2D surface seismic lines with limited 3D subsurface coverage and VSP surveys to monitor the injected CO_2; other successful CO_2 seismic monitoring programs have used 3D seismic datasets. The seismic program aims to monitor the size of the CO_2 plume using the changes in fluid saturation and pressure caused by injection and to identify possible leakage conduits in the overburden.

The seismic monitoring program includes of two east-west and one north-south source-receiver lines (Figure 1.5). The source-receiver lines are 3 km long and provide a good distribution of source-receiver offsets over the survey area. Two additional north-south receiver lines were added in order to improve subsurface fold. The seismic surveys have a nominal source and receiver spacing of 40 m and 20 m respectively, but some locations had to be moved due to pipelines, highways, and production pads. Figure 1.7 shows the actual source positions for all of the lines in the baseline survey. The dynamite charge size was 2 kg, and the shot holes were set at a depth of 18 m for most of the shots. The receivers used in the surface seismic survey were multicomponent geophones.

The baseline seismic survey was acquired in March 2005 by Veritas DGC. All of the shots in the surface seismic program were simultaneously recorded into the downhole geophone array. CO_2 injection commenced a week after the baseline survey at a rate of approximately 35 tonnes/day. The first monitor survey was acquired in December 2005.

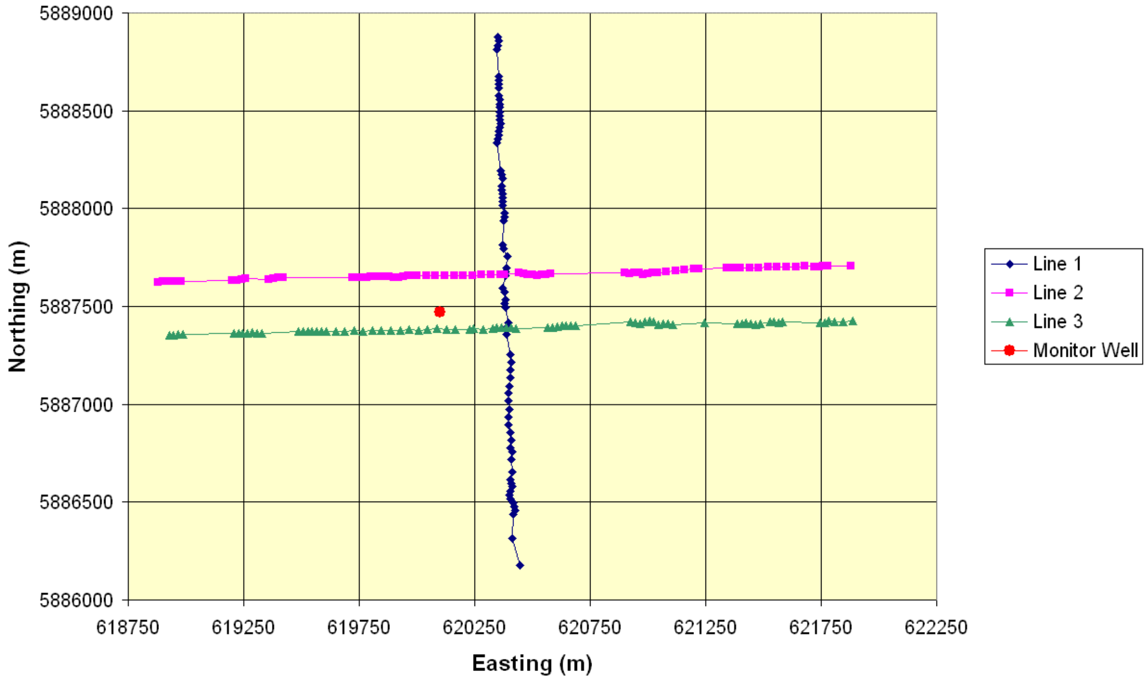

Figure 1.7: Shot locations for the baseline survey.

1.3 Study Objectives

The aim of this particular thesis was to process the VSP data and to interpret the time-lapse changes caused by the injected CO_2. Chen (2006) presents the results from the Gassmann modelling and the analysis of time-lapse surface seismic data.

Chapter Two introduces the concept of carbon capture and storage (CCS) and its importance in reducing greenhouse gas emissions. This chapter looks at how the CO_2 is trapped in a reservoir, the monitoring tools available, the limits of seismic detectability, the storage potential in the Western Canadian Sedimentary Basin, the use of CO_2 for enhanced recovery, and some examples of successful commercial EOR/ CCS projects.

Chapter Three presents the theory behind the rock physics, time-lapse monitoring, and anisotropy. The bulk and shear moduli and density control the seismic response of a formation. When these parameters change as a result of hydrocarbon production or fluid injection so do many measurable seismic attributes. Seismic processing must compensate for anisotropy otherwise errors can be introduced at a variety of points in the processing flow.

Chapter Four focuses on the baseline VSP processing flow. The VSP processing flow included the development of an anisotropic velocity model, 3D wavefield separation, deconvolution, and time migration of the P- and SV-wavefields.

Chapter Five presents the results from the time-lapse processing and analysis. The tools used in the time-lapse analysis include comparisons of the baseline and monitor seismic data, repeatability metrics, cross-equalization results, crosscorrelations, and difference displays to identify changes in the reservoir caused by the injected CO_2.

The conclusions and recommendations for future work with the dataset are contained in Chapter Six.

Chapter Two: Carbon Capture and Storage

2.1 Introduction

As CO_2 emissions increase worldwide and the effects of climate change become more apparent, it is becoming increasingly important to find ways to reduce these emissions through renewable energy sources, more efficient energy production and use, and mitigation measures such as geologic sequestration of CO_2. In the immediate future, carbon capture and storage is one of the most promising options for deep reductions in CO_2 emissions. It is a four step process in which a nearly pure CO_2 stream is separated and captured from flue gas or other industrial processes, it is compressed and transported to a storage site, and then it is injected underground into a geological formation where it can be stored for hundreds to thousands of years (Benson, 2005).

The regions with the highest potential for CO_2 storage are sedimentary basins with thick sequences of sedimentary rocks (Bachu, 2002). Many large sedimentary basins in North America, such as the Illinois, Michigan, and WCSB, are located close industrialized regions (Whittaker et al., 2004). As in the case of hydrocarbon reservoirs and aquifers, the most prospective formations for CO_2 storage are sandstone or carbonate formations with shale or evaporate seals (Benson, 2005). Indeed, some of the geologic formations with the highest potential for CO_2 storage are active or depleted hydrocarbon reservoirs, saline aquifers, and coal seams (Figure 2.1).

This chapter examines the most important trapping mechanisms for CO_2 within a formation, formation characterization and monitoring, the present limits of seismic detectability, the storage potential in the WCSB, how CO_2 can be used to enhance recovery, and some examples of commercial EOR/ CCS projects around the world.

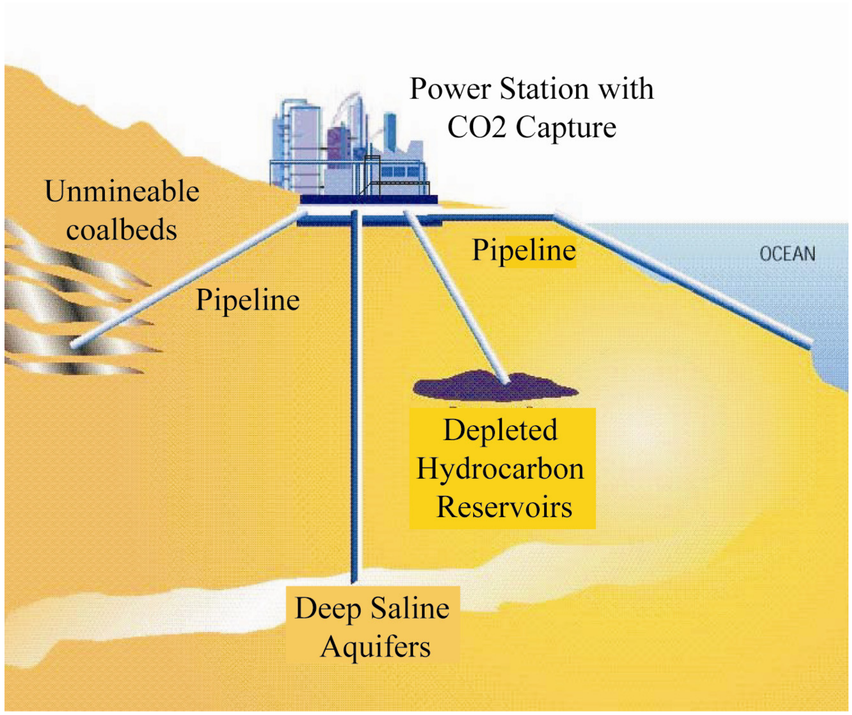

Figure 2.1: Geologic formations with the highest potential for CO_2 storage (from IEA Greenhouse Gas R & D Programme, 2001).

2.2 Trapping Mechanisms

It is critical to determine which trapping mechanisms will be most important at a particular location during the characterization phase of the project. In geologic formations, the trapping mechanisms for CO_2 change with time. Initially, physical trapping is the most important trapping mechanism (Figure 2.2). The injected CO_2 is trapped as a gas or a supercritical fluid under a low permeability cap rock in the same way hydrocarbons are trapped in a reservoir. The injected CO_2 will begin to dissolve into the formation fluids almost immediately; this is referred to as solubility trapping (Benson, 2005). As time goes on and the size of the CO_2 plume increases, it will encounter fresh formation fluid and higher volumes of CO_2 will dissolve into the fluid.

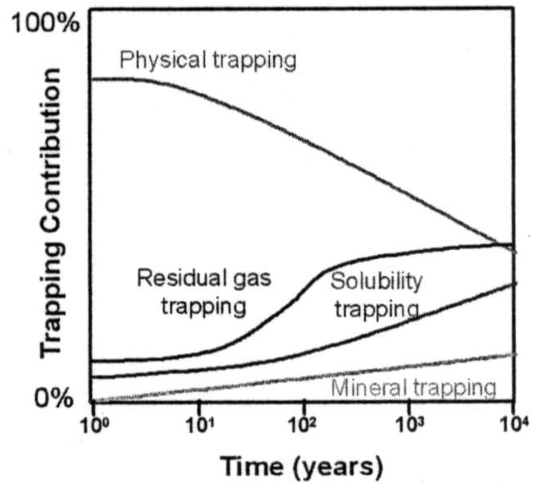

Figure 2.2: Importance of the CO_2 trapping mechanisms with time (from Benson, 2005).

The importance of residual gas trapping also increases with time; the trapped CO_2 may be in a gaseous or supercritical state depending on the depth of the formation. In this case, the CO_2 becomes trapped as the non-wetting phase in the pore space of the rock (Benson, 2005). In a formation, the rock surfaces will be preferentially covered by a certain fluid. If a formation is water-wet, then water will preferentially cover the rock surfaces, and a non-wetting fluid, such as CO_2, will form disconnected blobs in the pore spaces (Figure 2.3). When the CO_2 saturation drops below the residual gas saturation, it is immobilized within the formation. Recent studies have shown that residual saturation within a formation may be as high as 20-30% of the pore space depending on the petrophysical properties of the formation (Benson, 2005). It is believed that this mechanism will play a significant role in immobilizing CO_2 in the long term (Figure 2.2).

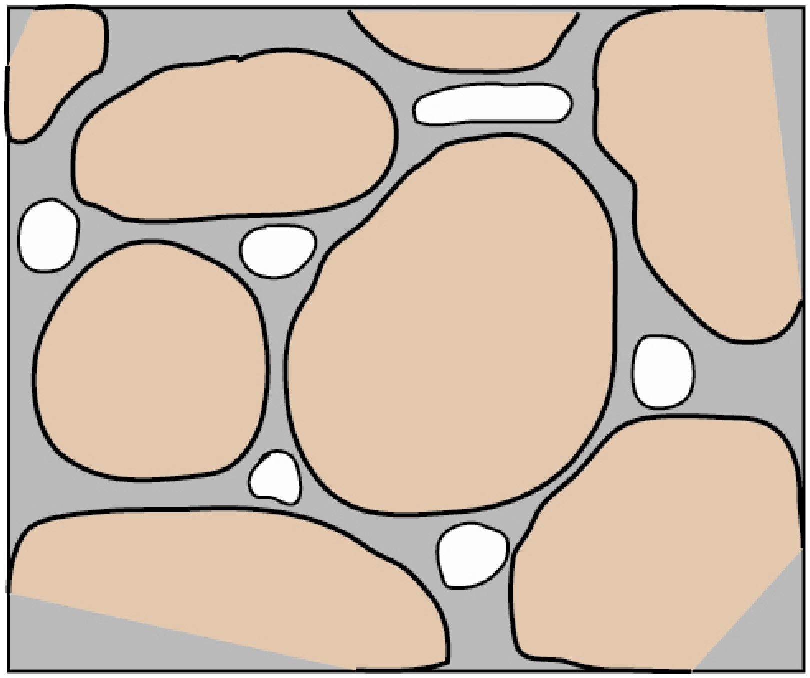

Figure 2.3: Residual CO_2 trapping in a formation. The CO_2 is the non-wetting phase and forms disconnected blobs in the pore space that are very difficult to mobilize.

Finally, the CO_2 may react with the minerals and organic matter in the reservoir and become part of the solid mineral matrix (Benson, 2005). Mineral trapping creates stable forms of carbon, such as calcite, siderite, or alumino-carbonates, which are unlikely to return to the biosphere. In the case of coal seams, the CO_2 adsorbs to the coal matrix which prevents leakage to the surface. Mineral trapping is a slow process, but it expected to trap significant fractions of CO_2 over time – particularly in formations with a high fraction of feldspar minerals (Benson, 2005).

2.3 Characterization and Monitoring

A site must meet certain criteria before it can be considered for long-term storage of CO_2 such as the presence of effective trapping mechanisms, primary and secondary formation seals, hydraulic isolation from overlying aquifers, and a minimal number of pathways for the CO_2 to migrate out of the storage formation (Whittaker et al., 2004). The initial geologic characterization should establish a regional stratigraphic and tectonic framework that extends from the basement structure to surface. Faults and fractures must be identified as they may provide the most direct natural pathways for CO_2 to migrate from the storage formation to shallow aquifers or the surface. It is also important to characterize the components of the subsurface hydrogeologic flow regime because flow pathways may extend hundreds of kilometres in a large sedimentary basin. Components of the subsurface flow regime that need to be characterized include the extent, distribution, and character of the flow units, barriers to fluid flow, potential traps inside and outside of the storage formation, and potential enhanced pathways for fluid flow (Whittaker et al., 2004).

Monitoring injected CO_2 is one of the highest priority requirements for the safe and secure storage of CO_2 (Benson, 2005). It is important not only for the industries that wish to reduce their emissions and gain tax credits for geologic storage, but also for government regulators trying to understand a relatively new science and for overall public confidence and acceptance. Monitoring is required for several reasons: to verify the net quantity of CO_2 that has been stored in the subsurface, to monitor sweep efficiency and to determine whether the storage capacity is being used effectively, to optimize enhanced hydrocarbon recovery (EHR) and enhanced coalbed methane (ECBM) projects, and to demonstrate that the CO_2 is being trapped in the storage formation and is not leaking into the overburden (Benson, 2005).

From a storage and safety perspective, CO_2 leakage from a storage formation is the biggest concern. CO_2 may leak into other geologic formations and contaminate the groundwater supply in an area, or in the worst case scenario, it may reach the surface and vent back to the atmosphere. The CO_2 can leak from a storage formation through geologic pathways or existing wells (Table 2.1). Old, abandoned wells are probably the cause for highest concern; however, exploration, production, and injection wells are all potential leakage conduits to the surface. A monitoring program must be designed with all of these possibilities in mind.

Table 2.1: Leakage pathways in geologic formations and wells (from Arts and Winthaegen, 2005).

Geologic Pathways	Well Integrity
• Fracture or fault activation due to increases in formation pore pressure • Dissolution or dehydration of the seal due to CO_2 • Unidentified faults or fractures in the formation seal	• Casing or cement defects • Deterioration of cement plugs after abandonment due to CO_2 • Corrosion of casing due to CO_2 • Formation damage caused by drilling • Operational failure of the well

Monitoring systems can be classified into three categories: instrumentation in a monitor well, instrumentation at the surface, and sampling to quantify CO_2 concentrations (Arts and Winthaegen, 2005). Table 2.2 is a summary of the different monitoring tools that may be used in each category. Monitoring programs draw from a combination of disciplines including ecology, atmospheric science, geochemistry, geophysics, petrophysics, and engineering. For all of the monitoring techniques, it is essential to obtain a baseline survey to determine the characteristics of the storage formation and the surrounding environment prior to CO_2 injection.

Table 2.2: Monitoring categories and options (from Arts and Winthaegen, 2005).

Well Instrumentation	Surface Instrumentation	Sampling Programs
• Geophones for active and passive monitoring • Pressure-temperature sensors • Time-lapse well logging • U-tubes for fluid sampling	• Time-lapse surface seismic surveys • Gravimeters • Tiltmeters • Atmospheric monitoring	• Geochemical • Atmospheric • Ecological

Geochemical surveys seek to establish the extent of a CO_2 plume in the reservoir and to quantify the CO_2 saturation at a particular location by sampling the reservoir fluids at production and observation wells. Fluids from overlying aquifers may also be sampled to determine if CO_2 is leaking out of the storage formation and into overlying strata. Atmospheric and ecological monitoring can be used to try to identify locations where CO_2 may have migrated to the surface and is venting to the atmosphere.

Well logging techniques can also be used to establish the extent of a plume and quantify the CO_2 saturation at production and monitor wells. Density, neutron porosity, resistivity, and sonic logs can all be used to verify the presence of CO_2 at a specific well and to determine the saturation level. Crosswell electromagnetic surveys can be used to monitor the CO_2 front as it progresses and determine the saturation distribution between wells (Jammes, 2006). The other critical application of well logs is in the evaluation well integrity; this is particularly important in areas with a high density of wells such as Alberta. Sonic and ultrasonic logs can be used to assess the quality of the cement in a well, and caliper and electromagnetic logs can be used to identify corrosion in the well casing (Jammes, 2006).

Time-lapse seismic surveys can be used to delineate the lateral extent of the CO_2 in a formation, identify potential leakage pathways in the overburden, and identify accumulations of CO_2 that may have migrated out of the formation. The advantage of installing geophones into a monitor well is twofold: during an active seismic survey, the geophones will provide a high resolution image around the monitor well, and they can be used for passive seismic monitoring between active surveys. Passive seismic monitoring uses microseismic events caused by pore pressure changes or fracturing in the formation to monitor the CO_2 flood.

Time-lapse seismic data can be used to detect qualitative fluid saturation and pressure changes in the formation, and will be discussed in the next chapter. However, it is very difficult to quantify the amount of CO_2 stored in a reservoir with seismic data alone because V_p becomes less sensitive to CO_2 saturation above values of 30-40%. Figure 2.4 is part of the Gassmann modelling completed for the Penn West pilot by Chen (2006). It demonstrates that V_p shows little variation above CO_2 saturations of 40-50% at the Penn West site. Similar results have been observed at the Weyburn CO_2 Monitoring and Storage Project where the synthetic seismic response to 10% free CO_2 was nearly the same as much larger amounts (Figure 2.5).

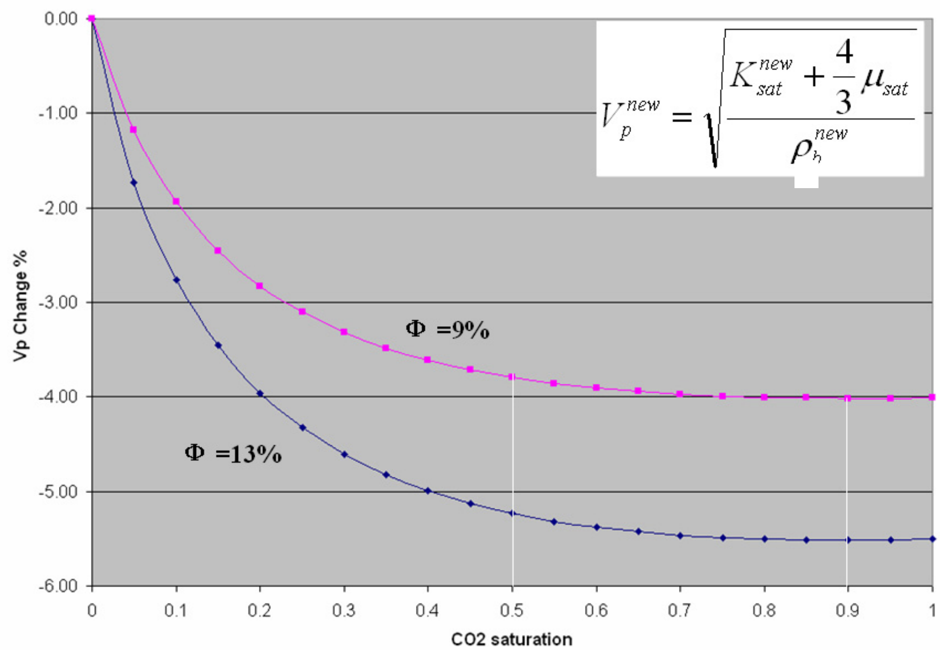

Figure 2.4: Change in V_p versus CO_2 saturation for a CO_2-water system where Φ is porosity, K is the bulk modulus, and μ is the shear modulus (from Chen, 2006).

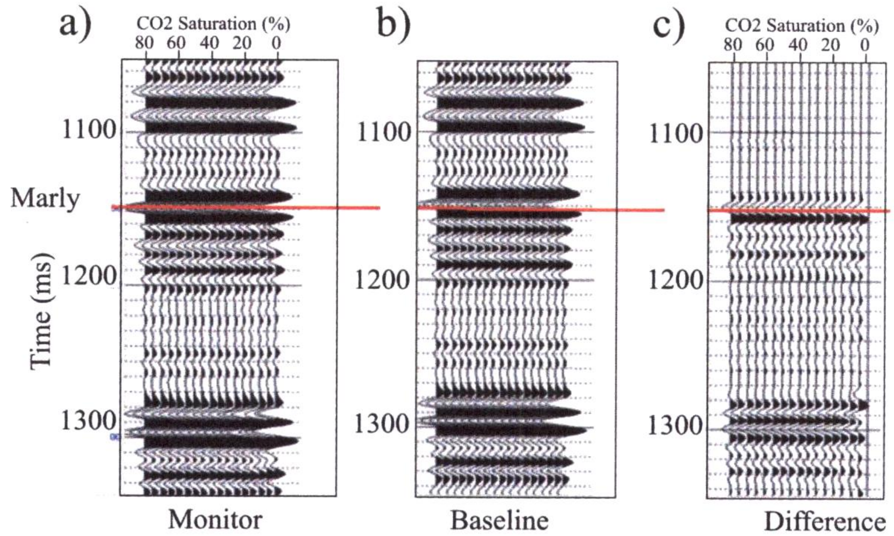

Figure 2.5: Monitor and baseline synthetic seismograms for CO_2 saturations ranging from 80% to 0%. In the model the CO_2 accumulation was 20 m thick. As the CO_2 saturation increases, V_p decreases in sensitivity (from White el al., 2004).

2.4 Seismic Detectability

Seismic data has the greatest probability of detecting CO_2 leakage in laterally extensive storage sites with low well densities. It is important to determine the smallest volume of CO_2 that can be identified with seismic data when designing a monitoring program. The volume of CO_2 that can be detected will be site specific and depend on factors such as the depth, porosity, and fluid saturation in the formation, the physical state of the CO_2, the repeatability of the seismic surveys, the interval velocity of the rocks, and the frequency content of the seismic wavelet (White el al., 2004).

At the Weyburn Project, researchers found that the seismic time shifts and amplitude differences between surveys had different CO_2 detection capabilities (White et al., 2004). CO_2 injection causes velocity to decrease in the reservoir, and this is measured as a traveltime increase through the reservoir. The difference in the measured traveltimes for a particular event from one survey to another is referred to as the time shift or time delay. Time shifts can be used to identify local zones of high fractional velocity change or thick zones with low fractional velocity changes, but they can not be used to resolve thin layers (White et al., 2004). In contrast, amplitude changes are more capable of detecting thin layers. Figure 2.6 is a comparison of the amplitude anomaly and time delay maps from two of the monitor surveys acquired at the Weyburn Project in 2001 and 2002. The amplitude anomaly maps show greater detail than the time delay maps because it is believed that the CO_2 flood has been restricted to thin layers in the reservoir (White et al., 2004). The thin CO_2 banks are not thick enough to produce a measurable time shift.

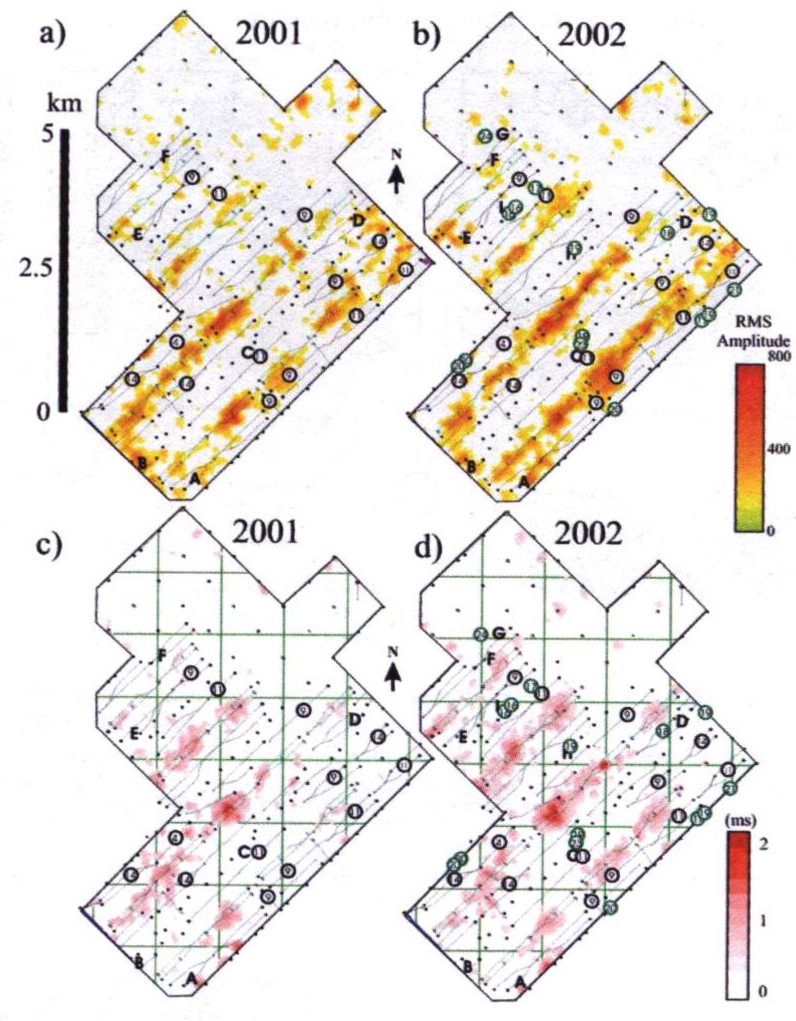

Figure 2.6: Comparison of the P-wave time-lapse anomaly maps from monitor surveys acquired in 2001 and 2002. (a,b) The amplitude difference maps from Monitor surveys 1 and 2. (c,d) The time shift maps from Monitor surveys 1 and 2. The amplitude difference maps show more detail than the time shift maps (from White et al., 2004).

Experience from Sleipner, Weyburn, and the Frio Pilot Test suggest that the lower limit of detection for CO_2 accumulations with seismic data is in the range of several thousand tonnes. Hoversten et al. (2006) have modelled the seismic response of 1000 tonnes of CO_2 at depths of 1300, 1000, 800, and 500 m as it migrates from a storage formation and accumulates in a cone-shaped wedge beneath a secondary trap (Figure 2.7). They found that the seismic data required a high signal-to-noise ratio in order to identify a 1000 tonnes of CO_2 at 1300 m and 1000 m (Figures 2.8c and d). As the CO_2 accumulation rose in the section, and it made the transition from the supercritical to gaseous phase, it became more compressible and expanded in size. Ultimately, this made the plume easier to identify. Further modelling showed that accumulations of as little as 100 tonnes could be detected at a depth of 500 m.

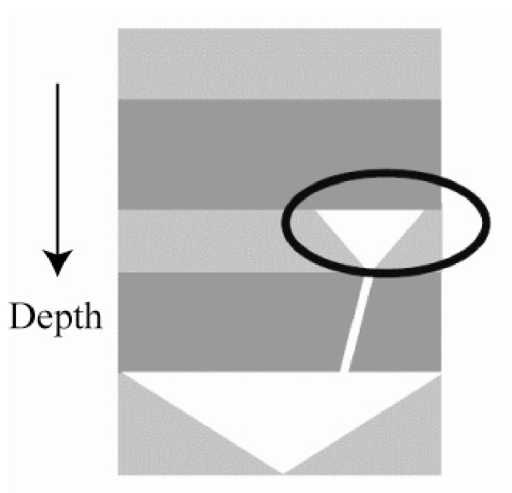

Figure 2.7: The cone-shaped model used to test the seismic response of a 1000 tonne CO_2 accumulation above a CO_2 storage site. The CO_2 accumulates in a wedge beneath a secondary trap above the main storage formation (from Hoversten et al., 2006).

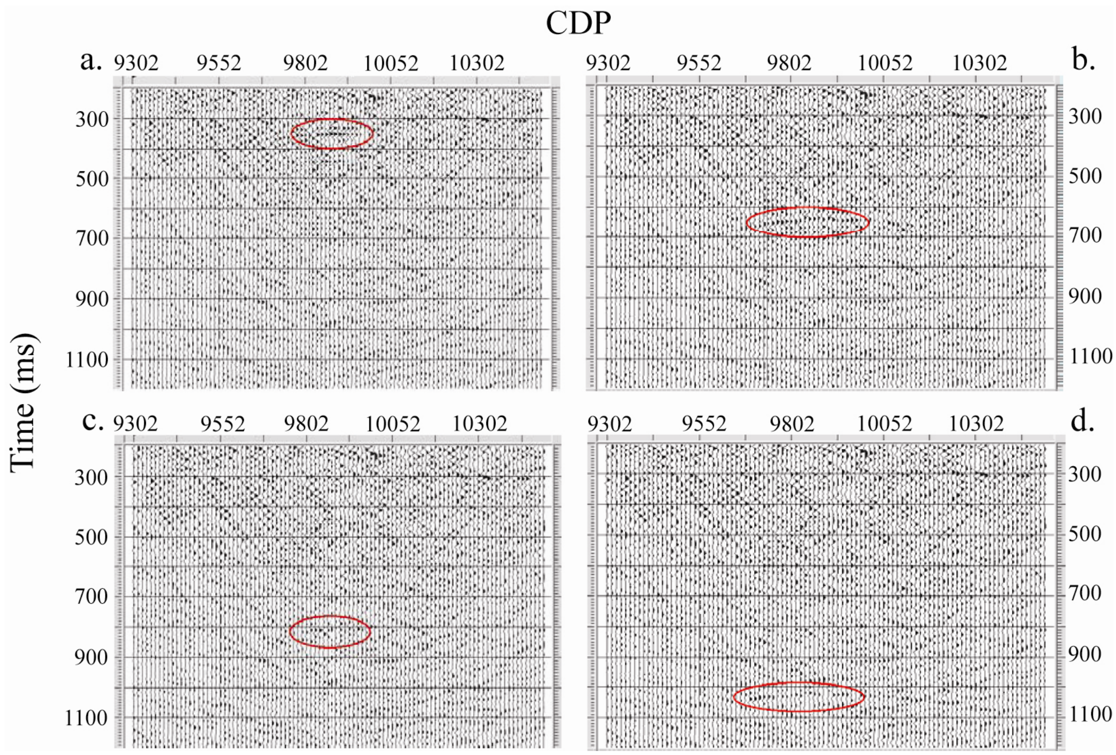

Figure 2.8: Difference displays from the seismic detectability modelling completed by Hoversten et al. (2006). The cone-shaped accumulations are located at (a) 500 m, (b) 800 m, (c) 1000 m, and (d) 1300 m.

The work done by Hoversten et al. (2006) demonstrates that surface seismic data will be an effective tool for identifying small volumes of CO_2 that may have leaked from the main storage formation and accumulated in the overburden. Surface seismic data will be particularly important in areas with low well densities where well-based methods can not be used to delineate the CO_2 plume. To date, the projects at Sleipner, Weyburn, and the smaller pilot projects do not show any evidence of leakage.

2.5 Storage Potential in the Western Canadian Sedimentary Basin

From 1990 to 2000, CO_2 emissions in Canada have risen from 460 Mtonne to more than 700 Mtonne per year (Bachu and Shaw, 2005). Most of the CO_2 emissions in Alberta, Saskatchewan, Manitoba, and northeastern British Columbia come from large stationary sources such as thermal power plants, refineries, oil sands plants, and cement plants. These provinces are located above the WCSB where there is huge potential to reduce CO_2 emissions by capturing and storing the CO_2 in geologic formations. The use of CO_2 for enhanced hydrocarbon recovery (EHR) is an excellent option in Alberta because usable infrastructure is already in place, the geology is already well understood, and the production of additional hydrocarbons will offset the cost of the CO_2 capture and storage.

Bachu and Shaw (2005) examined oil and gas reservoirs in the WCSB with capacities of more than 1 Mtonne of CO_2 and at depths between 900 and 3500 m (Figure 2.9). Reservoirs with a capacity of less than 1 Mtonne were not considered to be economic storage sites because of the fast rate at which they would fill to capacity. They estimated practical CO_2 storage capacities of 3200 Mtonne in gas reservoirs and 561 Mtonne in oil reservoirs; this includes up to 450 Mtonne of CO_2 which could be used for miscible flood EHR. The estimated storage capacity broken down by province is as follows: 2822 Mtonne in Alberta, 800 Mtonne in northern British Columbia, 118 Mtonne in Saskatchewan, and 1 Mtonne in Manitoba.

However, the active oil and gas reservoirs in Alberta will not be available for CO_2 storage immediately. Dahowski and Bachu (2006) examined 227 of the largest oil and gas pools with capacities greater than 5 Mtonne in Alberta and northern British Columbia, and only 25 of these pools could be used for CO_2 storage in the near future. In the next 15 years, 60% of these pools will become available as pools deplete; although some of these pools will be available for CO_2 EHR projects earlier. This database suggests that deep saline aquifers and coal seams may initially play an important role in storing CO_2 near large emitters. Deep saline aquifers in the Alberta Basin are estimated to have 100s of Gtonne of storage capacity while unmineable coal beds in the southwestern corner of Alberta may provide another 1-2 Gtonne of storage (Dahowski and Bachu, 2006).

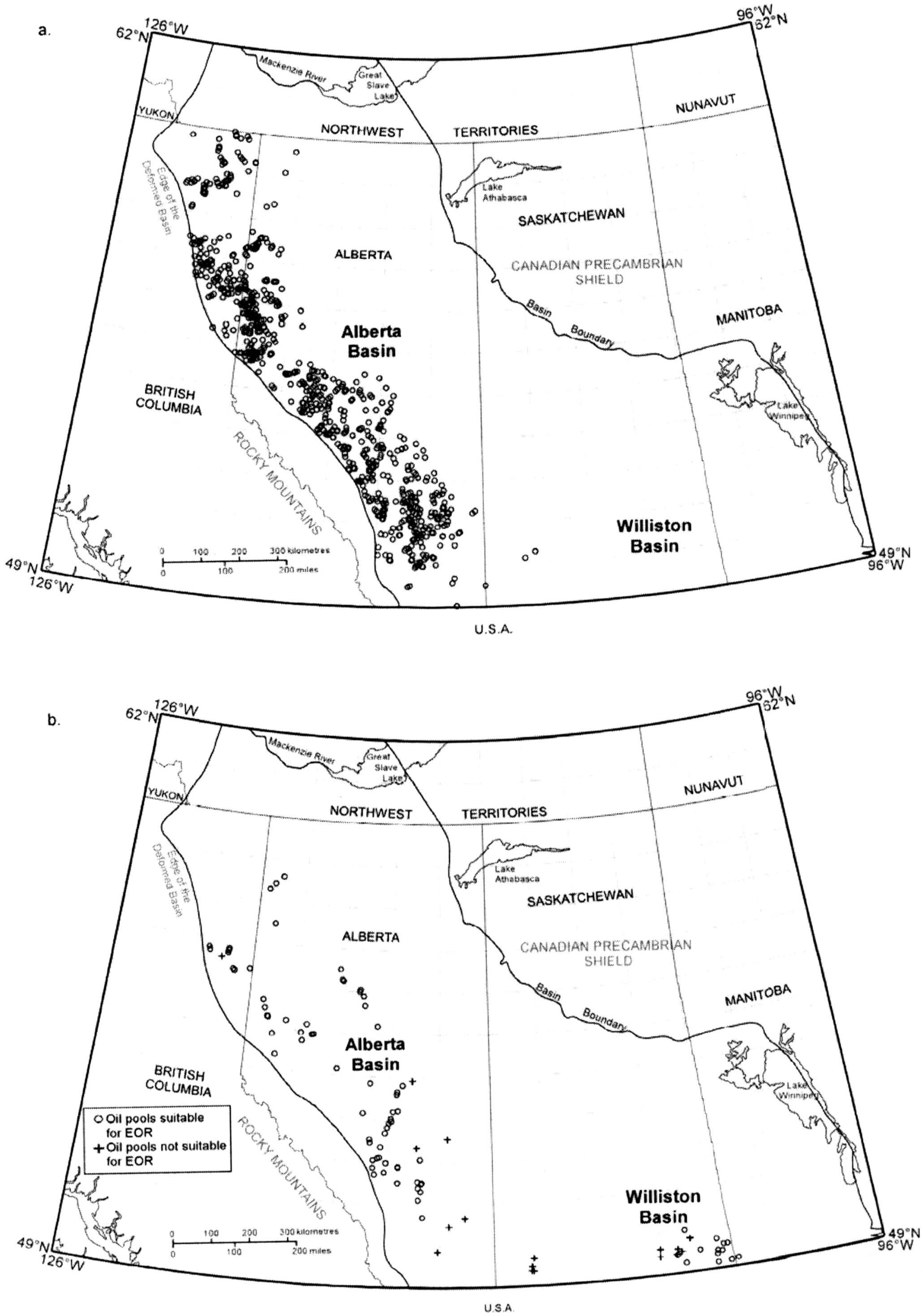

Figure 2.9: Distribution of gas and oil reservoirs in the Alberta and Williston Basins with a storage capacity of more than 1 Mtonne of CO_2: (a) gas reservoirs and (b) oil reservoirs (from Bachu and Shaw, 2005).

2.6 CO_2 For Enhanced Recovery

Pressure and temperature conditions determine the physical state of CO_2 (Figure 2.10). Generally, CO_2 will remain in a supercritical state if it is injected into a formation at or below 800 m because of the temperature and pressure conditions below that depth (Hoversten et al., 2006). The research completed at the Weyburn Project completed by White et al. (2004) demonstrated that injected CO_2 immediately begins to dissolve into the oil to form an oil-rich phase. If the reservoir pressure is stays above the minimum miscibility pressure, the CO_2 will capture vapourized intermediate hydrocarbons from the oil forming a CO_2-rich phase. Eventually, the CO_2-rich and oil- rich phases become miscible at which point the capillary forces holding the oil-rich phase in place drop so that the trapped oil can be swept from the pores. The estimated incremental oil recovery from CO_2 EHR for the Alberta Basin is between 7 to 23% of the original oil-in-place (Bachu and Shaw, 2005).

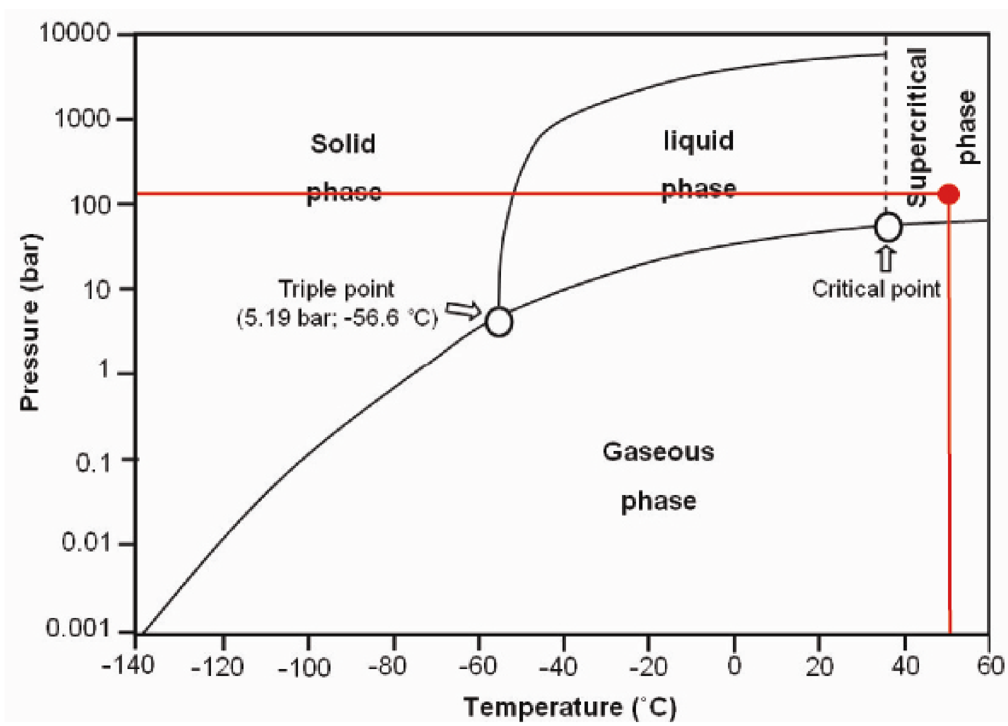

Figure 2.10: Phase diagram for CO_2 where 1 MPa = 10 bar (from www.acpco2.com). The red dot indicates the pressure – temperature conditions within the reservoir at the Penn West site.

CO_2 flooding has proved to be a very successful tertiary recovery method in the Weyburn Field. The field was discovered in 1954 and held an estimated 1.4 billion barrels of oil (Majer et al., 2006). In 1964, waterflooding commenced and oil production peaked at 46,000 barrels/day shortly afterwards. By the late 1990s, the field was again in decline with approximately 24% OOIP recovered. The CO_2 flood was initiated in 2000 and has resulted in a 24% increase in oil recovery. Oil production rates are now at the same level they were at in the early 1970s, and the field has exceeded initial oil production forecasts.

2.7 Large Scale CCS and EOR Projects

The world's first industrial-scale CCS project was the Sleipner project in the Norwegian North Sea. Statoil has been injecting about 1 million tons of CO_2 per year into a saline aquifer since 1996 (Benson, 2005). The CO_2 is being stripped from natural gas that is being produced at the Sleipner West Field and is re-injected into the Utsira Sand Formation. As of 2002, 4 Mtonne of CO_2 had been injected into the formation and the final storage target is for 20 Mtonne of CO_2 to be stored (Chadwick et al., 2003). The baseline 3D surface seismic data were acquired in 1994, and repeat surveys were acquired in 1999, 2001, 2002, and 2004 (Chadwick et al., 2006). Surface seismic imaging has been successfully used to map the CO_2 plume as it increases in size with time. Figure 2.11 displays seismic sections from Sleipner for the 1994 baseline survey and 1999 monitor survey.

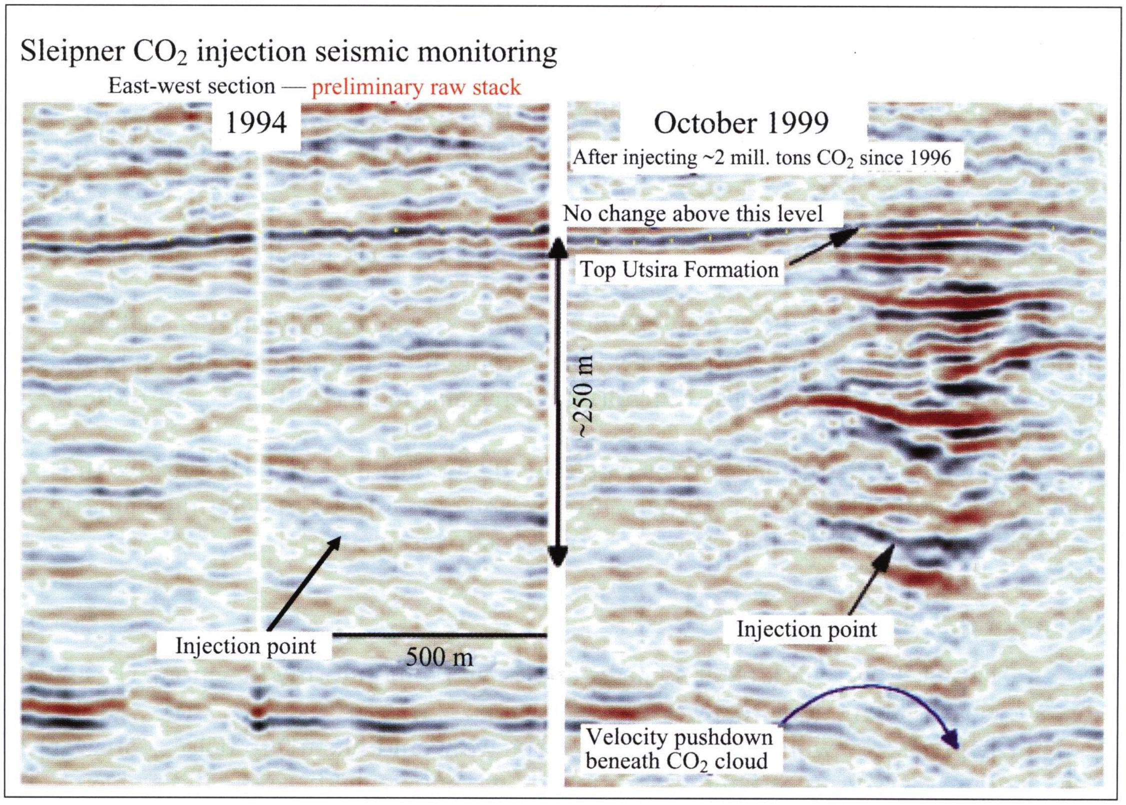

Figure 2.11: The baseline seismic survey (left) acquired in 1994, and the first monitor survey (right) acquired in 1999 at the Sleipner project (from Calvert, 2005).

A relatively new commercial scale CCS project, operated by BP, Statoil, and Sonatrach, commenced in 2004 at the In Salah Field in Algeria. The natural gas produced from three fields contain relatively high concentrations of CO_2. The CO_2 is captured from the gas stream and injected in an aquifer downdip from the gas pool (Figure 2.12). CO_2 injection rates here are also about 1 Mtonne/ year. The monitoring programs will include the installation of a permanent 3D surface seismic array, VSP, and well logging. Other CCS projects that should come on line in the next 5 years are the Gorgon Project in Australia operated by ChevronTexaco (http://www.chevron.com/cr_report/2003/co2_sequestration.asp), the Mongstad Energy Project in Norway (www.statoil.com), and the Latrobe Valley Project in Australia (http://www.co2crc.com.au/PUBS/brochures.html).

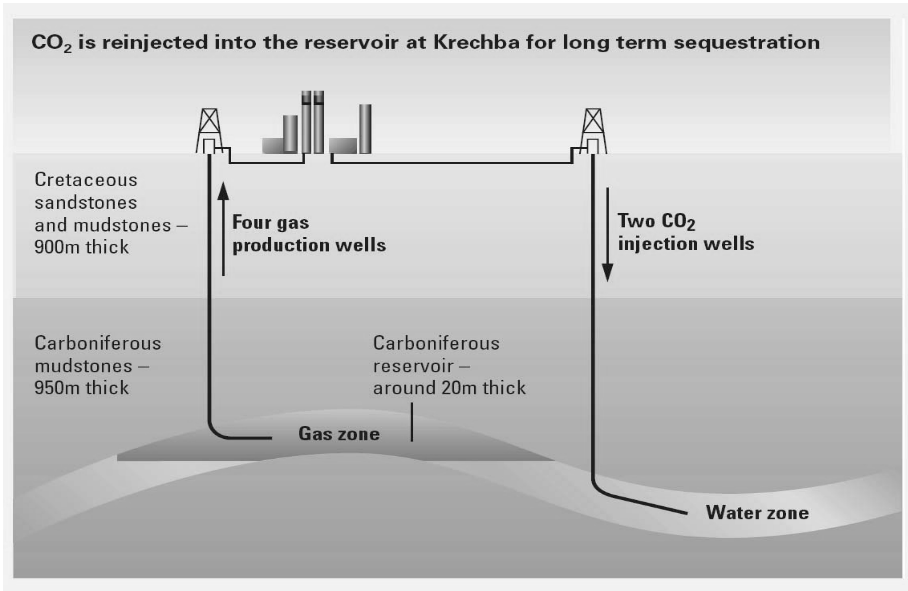

Figure 2.12: Schematic of the CO_2 injection at In Salah (from Ebrom et al., 2006). CO_2 is re-injected downdip from the gas reservoir.

The Weyburn Field is a large scale CO_2 EOR project with the final goal of geological storage of CO_2 over the long term. Approximately 1.7 million tons of CO_2 have been injected per year since 2000 (Benson, 2005). The CO_2 is transported via a 320 km pipeline from the Dakota Gasification Company's synthetic fuel plant in Beulah, North Dakota (Majer et al., 2006). Encana started the CO_2 flood in September 2000 with a series of 19 injection patterns. Over the next 15 years, they plan to add another 75 injection patterns to the field (Majer et al., 2006) and to store 20 Mtonne of CO_2 over the life of the project. In this field, the monitoring program consists of time-lapse 3D surface seismic surveys, crosswell seismic and VSP surveys, well logging, and geochemical monitoring.

Several more combined EOR/ CCS projects are in the planning stages. CO_2 from a gas power plant in Tjeldbergodden, Norway will be transported offshore for EOR in the Draugen and Heidrun Fields (www.statoil.com). BP plans to use CO_2 generated at a hydrogen plant located in Scotland for EOR in the Miller Field in the North Sea (http://www.bp.com/).

Chapter Three: Rock Physics, Time-lapse Monitoring, and Anisotropy

3.1 Introduction

In order to understand the time-lapse changes occurring in a reservoir, it is important to understand the rock physics behind the measured seismic parameters. The bulk modulus, shear modulus, and density of a formation are three of the most important rock physics parameters affecting time-lapse changes. These three parameters are controlled by the rock matrix, the pore fluid in the formation, and effective stress inside and outside of the formation. They can be used to predict the seismic response of a formation using the Gassmann equations, and they directly control the velocities of the seismic waves travelling through a formation.

The main objective of time-lapse surveys is to monitor small changes that are occurring in a formation as a result of production or fluid injection. Data repeatability is a critical factor that determines whether or not a time-lapse project is successful. Some of the tools used to identify time-lapse changes in a formation are difference displays, amplitude changes, and time shifts.

The final section of this chapter examines the causes and some of the types of anisotropy encountered in exploration seismology. Anisotropy can have a strong effect on seismic data and must be taken into account during processing. The elastic constants used to measure anisotropy are presented as well as a comparison of Thomsen's and Schoenberg's parameters.

3.2 Rock Physics

3.2.1 Fluid Saturation

As the fluid composition of a reservoir changes, so do the overall reservoir properties. The bulk modulus and density of the reservoir as a whole are affected by fluid saturation while the shear modulus may not be affected by formation fluids. In turn, these influence measurable seismic parameters, namely P-wave velocity (V_p) and S-wave velocity (V_s).

The most widely used and successful method used to predict fluid saturation effects in a reservoir are the Gassmann equations (Calvert, 2005):

$$K_{sat} = K_{dry} + \frac{(1 - \frac{K_{dry}}{K_s})^2}{\frac{\phi}{K_{fl}} + \frac{(1-\phi)}{K_s} - \frac{K_{dry}}{K_s^2}} \tag{3.1}$$

$$\mu_{sat} = \mu_{dry} \tag{3.2}$$

where K_{sat} is the bulk modulus of the fluid saturated rock, K_{dry} is the bulk modulus of the dry rock, K_s is the bulk modulus of the rock matrix, K_{fl} is the bulk modulus of the fluid, ϕ is porosity, and μ_{sat} and μ_{dry} the shear moduli of the fluid saturated and dry rocks respectively. The Gassmann equations make several important assumptions: 1. the rock is isotropic and monomineralic, 2. all pores are interconnected and communicating, 3. the pores are filled with a frictionless fluid, 4. the rock-fluid system being studied is closed, and 5. the pore fluid does not interact with the rock matrix in a way that hardens or softens the frame (Wang, 2001). As a result, Gassmann modelling may in fact underestimate the effects of fluid saturation changes in a reservoir (Schütt et al., 2005; O'Brien et al., 2004).

The bulk modulus of a reservoir is a measure of its incompressibility. It is affected by both the compressibility of the rock framework and the fluid filling the pore space (Figure 3.1). The overall bulk modulus of a high porosity rock is strongly influenced by the composition of the pore fluids. In general, the saturating fluids have a greater effect on the bulk modulus than changes in reservoir pressure (Schütt et al., 2005).

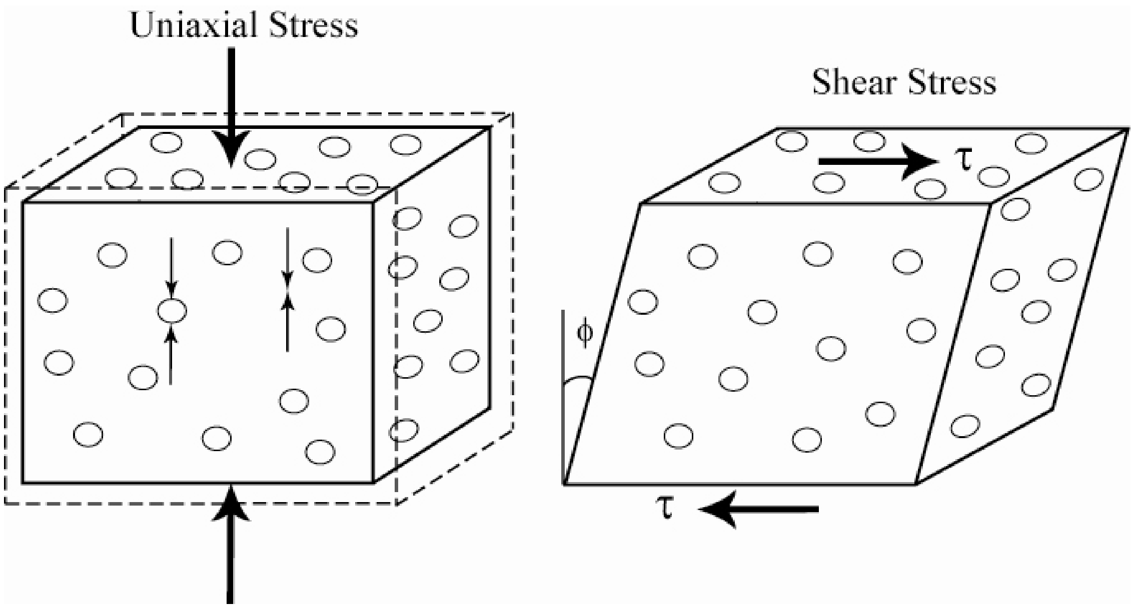

Figure 3.1: Effects of uniaxial versus shear forces on a rock body.

The least compressible fluids are brines. Oil can be twice as compressible as brine depending on its gravity value, and pure, supercritical CO_2 is 15 times more compressible than a brine (White et al., 2004). In a multi-fluid system, if one of the fluids is significantly more compressible than the other fluids, then it will dominate the effective compressibility of the fluids as a whole (White et al., 2004). Highly compressible fluids will decrease the bulk density of the reservoir as a whole and result in an observable decrease in V_p through the reservoir. So, as the injected CO_2 dissolves into oil, it can dramatically reduce the bulk modulus of the oil mixture and of the total bulk modulus of the fluid saturated rock (Figure 3.2).

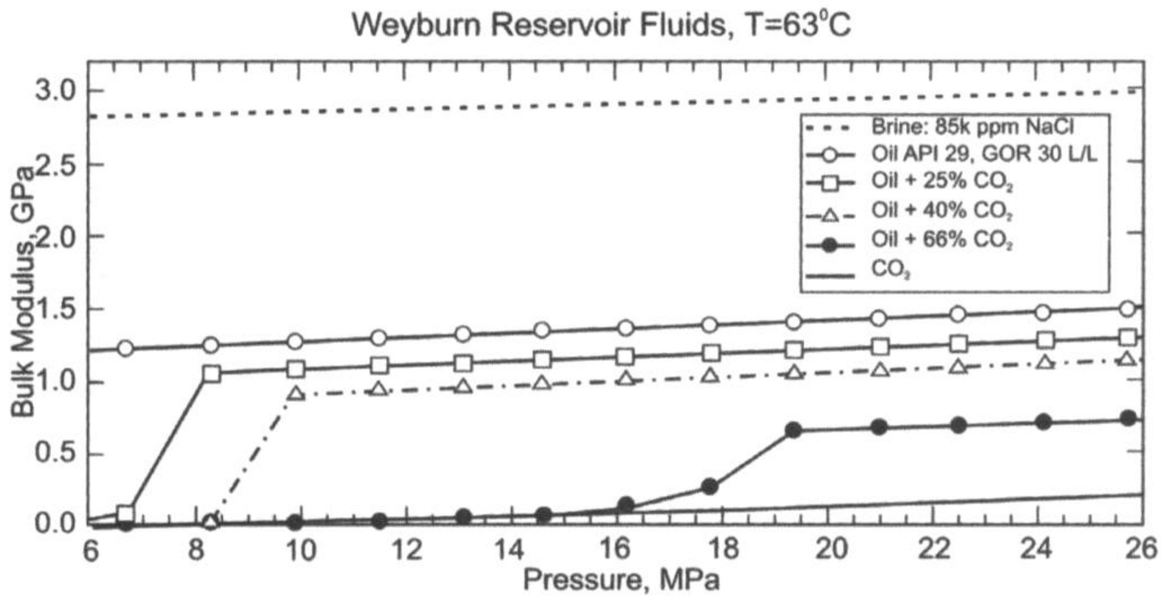

Figure 3.2: Effect of CO_2 saturation on fluid bulk modulus based on the Weyburn Project reservoir fluids (from White et al., 2004).

The shear modulus is a measure of the rigidity of a rock (Figure 3.1). The Gassmann equations assume that the shear modulus should not be affected by the saturating fluids in isotropic media because shear forces do not change the volume of the pore space or affect the pore fluid, and S-waves are unaffected by pore fluids. However, Schütt et al. (2005) conducted laboratory tests in which supercritical CO_2 was used to displace brine in sandstones. They found that the shear modulus varied by 4 to 7% depending on the saturating fluid in the pore space (Figure 3.3). They attributed this variation to anisotropic effects within the sandstone. Vernik and Liu (1997) have made velocity and anisotropy measurements on shale core. They discovered that saturant had a strong effect on V_s when the shales contained smectite. They attributed this effect to chemical and interfacial softening mechanisms rather than changes in fluid density.

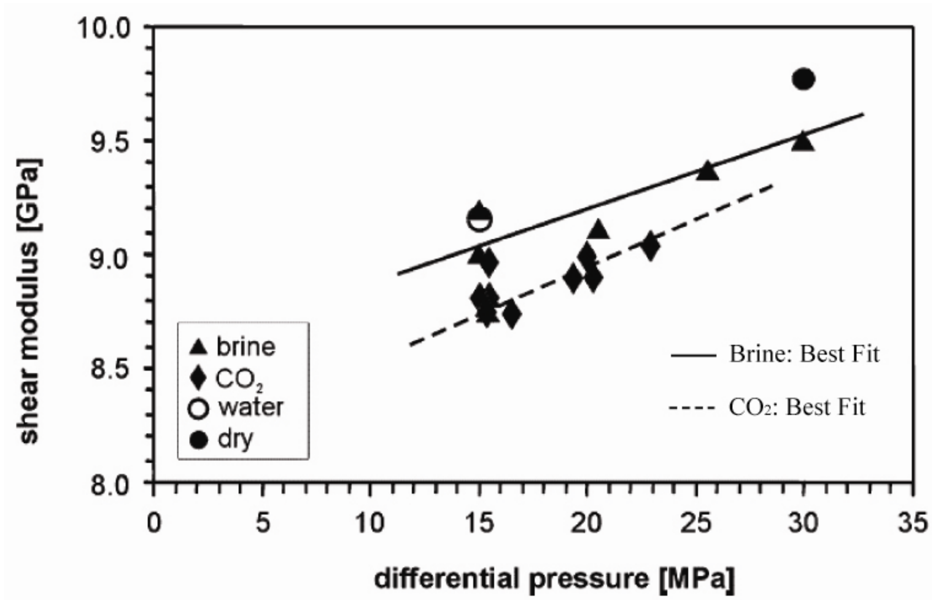

Figure 3.3: Measured shear moduli from a sandstone sample as a function of differential or effective pressure and fluid saturation (from Schütt et al., 2005).

Equations 3.3 and 3.4 express V_p and V_s in terms of the bulk modulus (K), shear modulus (μ), and density (ρ). Seismic wave speeds are usually dominated by the rock moduli, and the density effects tend to be secondary. For isotropic rocks, the 4D change in V_p depends on the magnitude of the change in fluid compressibility relative to the compressibility of the reservoir rock (Johnston and Terrell, 2006). When a highly compressible fluid, like CO_2, displaces water in an oil reservoir or saline aquifer, it will lower the P-wave velocities in the formation and may result in large impedance contrasts (Arts and Winthaegen, 2005). However, if gas is already present in a reservoir and CO_2 is injected, then V_p will not decrease to the same degree because the gas in the reservoir has already lowered the overall compressibility of the reservoir fluid. Hence, a large change in impedance will not be observed.

$$v_P = \sqrt{\frac{K + (4/3)\mu}{\rho}} \tag{3.3}$$

$$v_S = \sqrt{\frac{\mu}{\rho}} \tag{3.4}$$

3.2.2 Pressure Response

The velocities in a formation are affected by confining pressure or overburden weight, pore pressure within the formation, and effective stress. Effective stress is defined as the difference between the confining pressure and the pore pressure. The bulk modulus of a formation generally increases with depth and confining pressure. According to Equation 3.3, an increase in the bulk modulus will cause an increase in V_p while an increase in density will cause a decrease in V_p. The observed impedance contrast reflects the changes in V_p. Fluid injection increases the pore pressure in a formation and causes a relative decrease in the formation density which results in an increase in V_p and the impedance contrast. Velocity is more sensitive to pore pressure increases than it is to pore pressure decreases caused by hydrocarbon production (Calvert, 2005).

Pressure depletion is unique in that it can affect the rocks both inside and outside of a reservoir. Stress arching will occur as the reservoir compacts and the overburden begins to stretch vertically (Calvert, 2005). Compaction reduces the thickness of the reservoir, increases the reservoir density, and increases the seismic velocities. The combination of these effects results in a decrease in traveltimes through the reservoir. Above the reservoir, the overburden stretches and becomes thicker, so the velocities decrease and the traveltimes increase (Hatchell and Bourne, 2005). It can be difficult to separate the changes occurring outside of the reservoir from those in the reservoir.

Schütt et al. (2005) have shown that the shear modulus has higher pressure sensitivity than the bulk modulus. This means that V_s is also more sensitive to pressure changes caused by fluid production and injection. V_s is also very sensitive to fractures (White et al., 2004). Changes in the effective stress in a formation can cause fractures in the formation to open or close. When the fractures in a reservoir close due to an increase in effective stress, the shear modulus and the resulting V_s also increase.

3.3 Time-lapse Seismic Monitoring Attributes

3.3.1 Repeatability

The goal of time-lapse seismic surveys is to measure small changes that occur in the earth in relation to oil and gas production or enhanced recovery methods such as waterflooding or CO_2 injection. Seismic repeatability is the ability to replicate data from one survey to another and is one of the key factors that controls whether a time-lapse survey will be successful. It is affected by source-receiver geometry, consistency of the source signature, random noise, and shot-generated noises such as multiples and scattering. These variables contribute to many of the residual differences seen in time-lapse data (Kragh and Christie, 2002).

The time-lapse repeatability depends strongly on repeating the acquisition geometry of the baseline survey in subsequent monitor surveys because a significant part of what is considered noise on seismic data is caused by distortions related to subsurface heterogeneities (Calvert, 2005; Smit et al., 2005). As an example, if the source-receiver geometry is repeated for two locations, the raypaths of the two recorded traces will be the same and the coherent and apparent random noise will be repeated. When those two traces are subtracted, the repeated noise should cancel. Shot locations that are removed or relocated in a monitor survey will result in differences that are not related to changes in the reservoir, and these differences may overwhelm the subtle amplitude and time shift differences that need to be identified.

On land, a high degree of source-receiver repeatability can be achieved when GPS technology is used to position the sources and receivers. If the surveys use dynamite as a source, the shot locations can be cased so the positions are fixed from survey to survey. The corresponding increase in time-lapse sensitivity may allow changes in a reservoir to be monitored even when it is difficult to image the reservoir with standard methods (Calvert, 2005).

Landrø (1999) examined the issue of trace repeatability with 3D VSP data acquired over the Oseburg Field in the North Sea. He found that positioning errors on the order of

5-10 m significantly affect the repeatability of traces. As the distance between shots increases from 10 to 40 m, the repeatability decreases by a half. Figure 3.4 shows some of the difference traces obtained for trace pairs from the vertical or z-component of the data with the distance between shots ranging from 5 to 50 m. The difference traces were created using a sample by sample subtraction. As the offset between shots increases, the difference traces have higher amplitudes.

The x-component of the data proved to be as repeatable as the z-component of the data. However, the x-component is more sensitive to positioning errors because the positioning errors occur in the x and y directions rather than the z direction.

The source signature can vary from shot to shot as well as from survey to survey due changes in the ground condition, thickness of the weathering layer, depth of the shot holes, or the type of source. Waveshaping deconvolution is used to try to remove the effect of source variability from the data. One of the advantages of a permanently emplaced receiver array is that the actual downgoing wavelet is recorded at each geophone for each survey. The deconvolution operator is designed on the downgoing wavefield and is used to remove the effect of source variability from the upgoing wavefield. It is important to note that the deconvolution operator is less effective when it is applied to data below the geophone array, as a direct arrival is not recorded for formations beneath the receiver array.

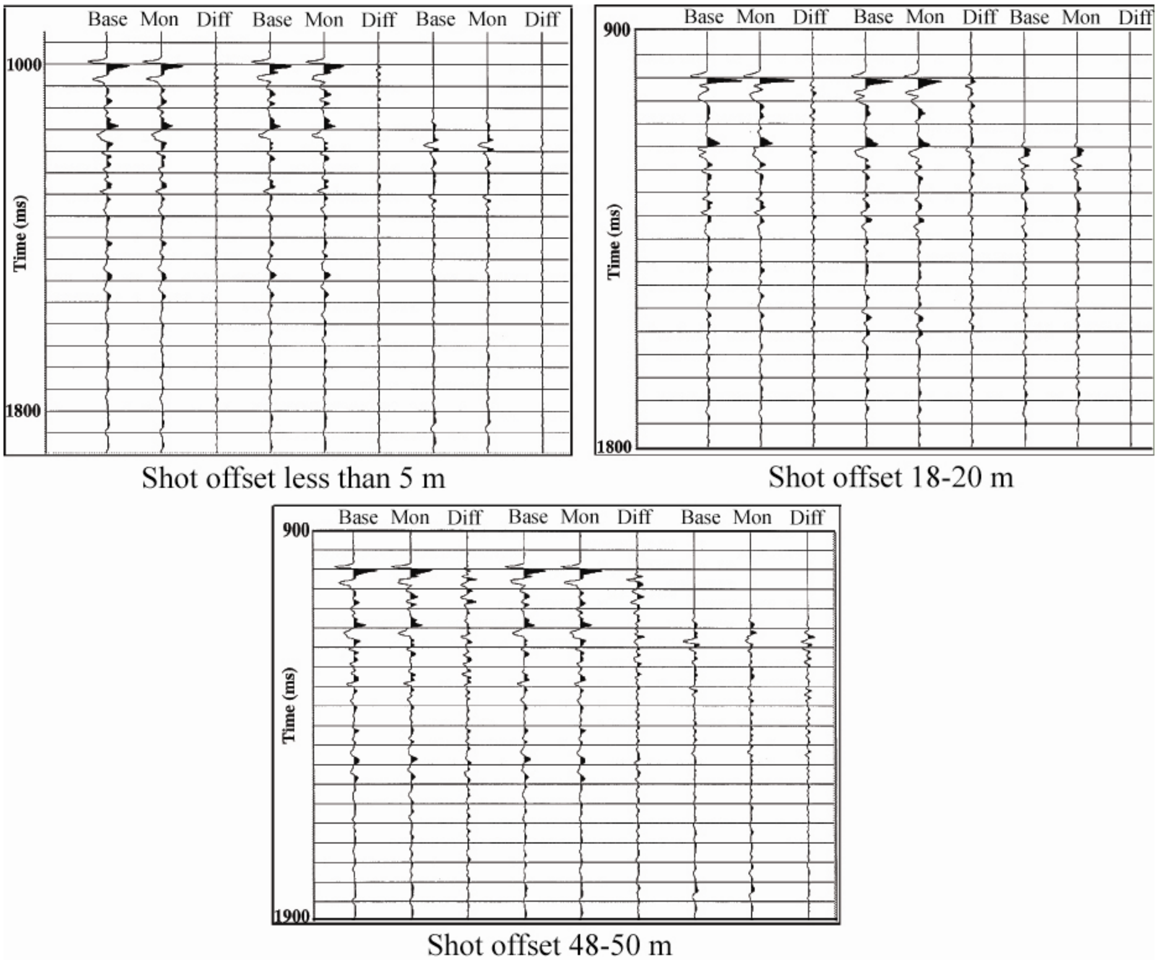

Figure 3.4: Difference traces from the z-component of 3 trace pairs with varying shot offset. As shot offset increases, so does the noise on the difference traces (from Landrø, 1999).

Since deconvolution is rarely perfect, seismic data should be cross-equalized as well. Cross-equalization is a statistical method used to minimize the differences in the data that are not related to production and processing (Johnston and Terrell, 2006). Ideally, the cross-equalization filter should be designed on a section of the data above the reservoir that has not been affected by production or fluid injection (Calvert, 2005). Some of the tools used in cross-equalization include residual time alignment, amplitude normalization, residual matching of amplitude and phase spectra, and repeatability estimates such as the normalized root mean square difference (NRMS) and predictability (Johnston and Terrell, 2006). It is important to note that surveys with well-repeated geometries will require less cross-equalization that those with poorly repeated geometries.

NRMS and predictability are two commonly used repeatability metrics that were developed to quantify the likeness between two traces. They were first presented by Kragh and Christie (2001) and are complementary measures of repeatability that are sensitive to different data attributes. They can be used to analysis the repeatability of two traces at any point in the processing flow.

NRMS is a percentage that is defined as the RMS amplitude of the difference divided by the mean RMS of the two traces (Calvert, 2005). It is defined by the following equations:

$$NRMS = \frac{200 \times RMS(a_t - b_t)}{RMS(a_t) + RMS(b_t)}, \tag{3.5}$$

where a_t and b_t represent two traces within a given window t_1-t_2, and the RMS operator is defined as:

$$RMS(x_t) = \sqrt{\frac{\sum_{t_1}^{t_2} (x_t)^2}{N}} \tag{3.6}$$

where N is the number of samples within the window t_1-t_2. NRMS values range from 0 to 200%. If the traces are identical NRMS = 0%, and if they anti-correlate NRMS = 200% (Kragh and Christie, 2001).

Predictability is defined in terms of correlations in the following equation:

$$PRED = \frac{100 \times \sum \Phi_{ab}(\tau) \times \Phi_{ab}(\tau)}{\sum \Phi_{aa}(\tau) \times \Phi_{bb}(\tau)} \tag{3.7}$$

where Φ_{ab} denotes the crosscorrelation between traces a_t and b_t. In this case, the values for predictability range between 0 and 100%. If the traces are uncorrelated PRED

= 0%. Amplitudes do not affect predictability, so if the traces are anti-correlated or the amplitudes do not match then predictability will still be 100%

NRMS is very sensitive to small changes in amplitude, phase, and time shifts in the data. For example, a 10^{o} phase shift, which is equivalent to a 0.55 ms time shift at 50 Hz, will result in an NRMS = 17.4% (Kragh and Christie, 2001). Koster et al. (2000) reported the NRMS values for two towed streamer 4D surveys in the North Sea. The surveys over the Draugen Field had an NRMS of 35% while surveys acquired over the Gannet C Field had NRMS values of 20%. Predictability is not sensitive to these changes; instead it is sensitive to the amount of noise in the data and changes in reflectivity in the data. Kristiansen et al. (2000) calculated the predictability for a towed streamer survey vs. a seabed survey over the Foinaven Field in the North Sea. The predictability of the towed streamer surveys was 93%, and the predictability of the seabed surveys was 99%.

Figure 3.5 is an example of the NRMS and predictability values calculated on for each CMP trace on a 2D line from the Gulf of Mexico. The predictability values are high and the NRMS values are low between CMPs 1400 to 1700 where few differences can be seen in the difference display. In this interval, NRMS ranges from 18 – 30% and the predictability ranges from 93 – 99%. However, the strong coherent events on the difference display between CMPs 2400 to 2700 correlate to poor repeatability results where NRMS is greater than 100% and predictability is less than 50%.

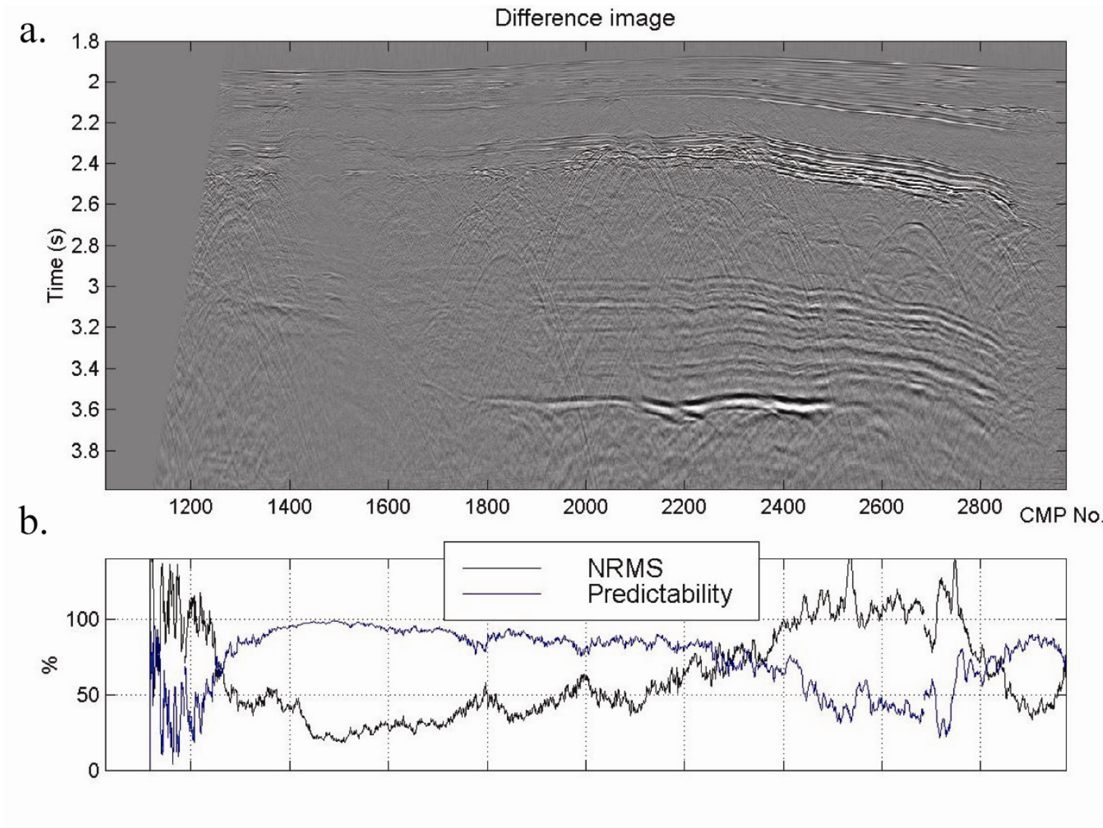

Figure 3.5: (a.) The difference data from a 2D repeated line. (b.) The NRMS (black) and predictability (blue) values for each CMP trace one the line. The NRMS and predictability values show a negative correlation (from Kragh and Christie, 2001).

3.3.2 Difference Data

If a reservoir is thin or if it is within the tuning range for a strong reflector, then any amplitude or traveltime changes that occur from survey to survey will be difficult to identify on the seismic sections alone (Calvert, 2005). Differencing the baseline and monitor survey data is a powerful tool when looking for changes in time-lapse data. Reservoir changes become much easier to identify when a difference section is created and the geology, multiples, and repeatable shot noise are removed. Other details, such as small faults, in the reservoir may also be more visible on difference displays (Calvert, 2005). Finally, difference data provides repeatability information on the datasets; if there is a significant amount of coherent noise in the areas away from the reservoir, it could indicate that there are problems with the acquisition geometry or the processing.

3.3.3 Amplitude changes

The time-lapse amplitude response of a reservoir may be affected by a variety of factors: fluid saturation and pore pressure changes, reservoir compaction, and extension of the overburden due to reservoir compaction (Tura et al., 2005). However, changes in the seismic amplitudes are most often used as an indicator of fluid saturation changes in a reservoir. Large amplitude changes are expected when CO_2 is injected into a saline aquifer because of the contrast in compressibility between the two fluids.

Amplitude changes have been used to track waterfloods in many fields in the North Sea including Draugen, Valhall, and Gannet (Calvert, 2005). In the case of CO_2 flooding for enhanced recovery, amplitudes have been used to map the CO_2 flood at Encana's Weyburn Field in Saskatchewan and at Anadarko's Patrick Draw Field in Wyoming (Li, 2003; O'Brien et al., 2004). At the Weyburn Field, the amplitude changes have been observed at the reservoir interval (Figure 3.6) and are related to fluid saturation changes within the reservoir (White et al., 2004). Similar amplitude changes have not been identified in the overlying strata (Figure 3.7). Large amplitude differences have also been observed at the Sleipner and Frio CO_2 storage projects where CO_2 is being injected into saline aquifers (Chadwick et al., 2006; Daley et al., 2006).

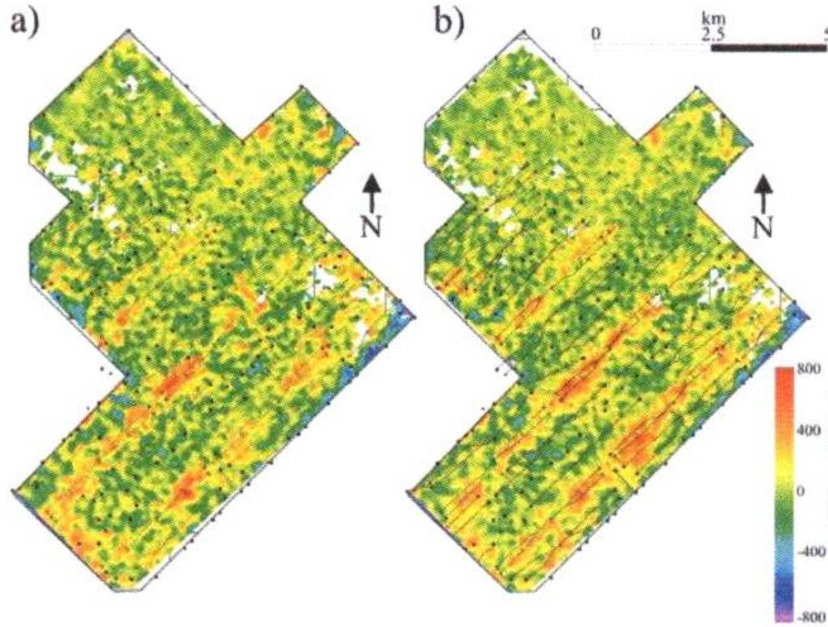

Figure 3.6: Amplitude difference maps from the Midale Marly horizon for (a.) Monitor Survey 1 acquired in 2001 and (b.) Monitor Survey 2 acquired in 2002. The amplitude anomalies are associated with the horizontal CO_2 injector wells (from White et al., 2004).

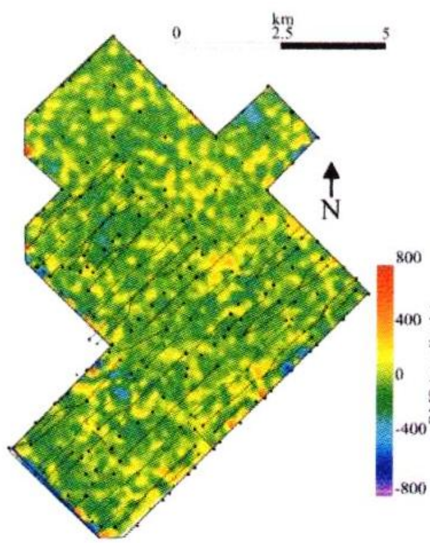

Figure 3.7: Amplitude difference map from the Lower Gravelbourg horizon, located above the Midale Marly horizon, from Monitor Survey 2. This horizon does not show any of the amplitude anomalies seen in the Midale Marly horizon (from White et al., 2004).

3.3.4 Time shifts

As the velocities in a formation change over time, the measured traveltimes through a formation change as well. The difference in the measured traveltimes between two surveys for a particular event is referred to as a time shift or time delay.

4D time shifts can be caused by acquisition and processing changes from survey to survey, changes in the velocity field over time, and production induced reservoir compaction. The velocity field in a survey area may vary because of reservoir depletion and compaction, changes in reservoir pressure, and changes in the fluid saturation in the reservoir. Large time shifts are generally observed in conjunction with reservoir compaction or with increases in reservoir pressure. Small time shifts are usually associated with fluid saturation changes and reservoir depletion.

At the Weyburn Field, small time shifts from 0.4 to 2 ms have been measured from the time-lapse surface seismic data and correlated to injected CO_2 volumes in the field (Figure 3.8). Landrø et al. (2005) and Meunier et al. (2000) have completed studies using VSPs and permanently emplaced receiver arrays that have measured time shifts on the order of 0.2 ms that were related to small pressure variations within the reservoirs. At a SAGD site in Alberta, Forgues et al. (2006) have measured traveltime differences of 0.036 ms over a three day period using a fixed geophone array in a monitor well and a fixed piezoelectric source at the surface.

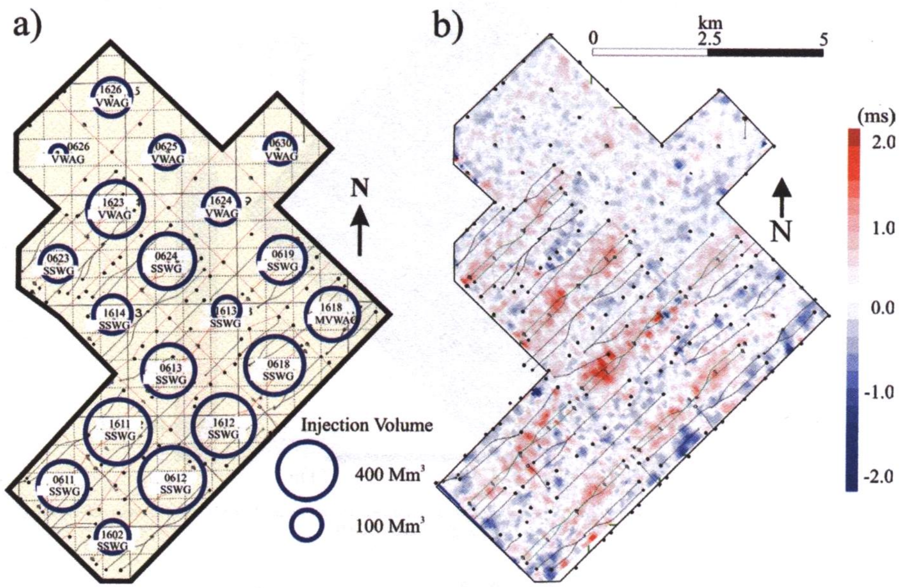

Figure 3.8: Comparison of the (a.) CO_2 injection volumes and (b.) the time delay anomalies at the time of the second monitor survey in 2002. The time delay anomalies correlate well with the injected volumes of CO_2 (from White et al., 2004).

Reflection traveltimes beneath a reservoir may be also affected when the velocity within the reservoir changes. When the traveltime in a formation increases, it results in a velocity push-down of events underneath the formation (Figure 2.10). Likewise, if the traveltime decreases, the reflections beneath the formation display velocity pull-up. These time shifts are not necessarily consistent with depth. In the Weyburn Field, the effect of the time shift decreases with depth (Li, 2003). This is probably due to the long offset shots undershooting the CO_2 plume. For large source-receiver offsets, the downgoing wave may travel through the reservoir well away from the CO_2 flood while the reflected wave passes through the CO_2 plume as it travels towards the geophones. The resulting time shifts may be too small to measure.

Small time shifts between surveys can make it difficult to identify meaningful changes when the difference displays are created. The magnitude of the time shift for an entire seismic section can be determined sample by sample using a sliding crosscorrelation window. A fixed crosscorrelation window can be used to calculate the time shift for a particular event (Tura et al., 2005; Landrø et al, 2005). Once the magnitudes of the time shifts have been determined, they should be stored as an interpretable attribute and removed from the data so that the amplitude comparisons can be optimized in the difference displays (Johnston and Terrell, 2006).

3.4 Anisotropy

3.4.1 The Basic Concepts

Anisotropy is the directional dependence of the physical properties measured at a particular location in a formation. It is caused by inhomogeneities in a rock body. If anisotropy is not taken into account when processing seismic data, it can lead to errors in velocity analysis, normal move-out (NMO), migration, time-to-depth conversion, and AVO analysis (Sayers, 1997). The causes of anisotropy in sedimentary rocks include: interlayering lithologies on a scale much finer than the seismic wavelength (Backus, 1962), preferred orientation of platelet minerals such as clay (Winterstein, 1990), oriented microcracks or fractures (Winterstein, 1990), in-situ stresses that modify pore shapes and pre-existing fractures (Winterstein, 1990), the presence of kerogen in shales (Vernik and Nur, 1992; Vernik and Liu, 1997), and physicochemical interactions with pore fluids (Vernik and Liu, 1997).

Transverse isotropy is the simplest type of anisotropy. In this case, the elastic properties differ in one distinct direction and are the same in the other two orthogonal directions (Thomsen, 1986). Transverse isotropy can be vertical (VTI) or horizontal (HTI) depending on whether the physical characteristics causing the anisotropy appear in the vertical or horizontal plane. VTI is most often associated with shales and small scale horizontal layering. HTI is typically referred to as azimuthal anisotropy and is related to vertical cracks and fractures within a formation (MacBeth and Lynn, 2000). For VTI rocks, the plane of symmetry is horizontal and parallel to the bedding planes, so waves propagating parallel to bedding planes have faster velocities than those travelling perpendicular to bedding. Jones and Wang (1981) found that P-wave velocities were always higher for propagation parallel to bedding than to propagation perpendicular to bedding (Figure 3.9). Similarly, Sh-waves propagating parallel to bedding had higher velocities than Sh-waves propagating perpendicular to the bedding or SV-waves propagating parallel to the bedding (Figure 3.9).

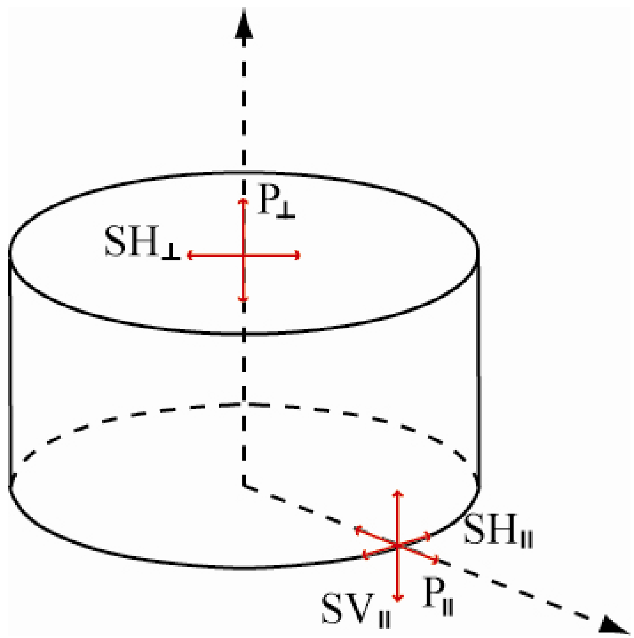

Figure 3.9: Modes of propagation for the P-, Sv-, and Sh-waves in a transversely isotropic medium (modified from Jones and Wang, 1981).

Shale formations constitute over 75% of the clastic fill in sedimentary basins and often act as the seal for hydrocarbon reservoirs (Jones and Wang, 1981). At the microscopic level, shale grains are flat and align in a preferential direction; this preferential alignment of clay platelets is believed to be the primary cause of anisotropy in shales (Hornby et al., 1994). Field and laboratory measurements show that VTI is most often associated with shales (Jones and Wang, 1981; Winterstein and Paulsson, 1990).

The measured velocity and anisotropy of shale has also been shown to increase with compaction and depth. Kaarsberg (1959) observed that the degree of velocity anisotropy increases with depth of burial. He attributed this to the increase in mineral alignment that results in an increase in bulk modulus. Anisotropy tests conducted in the laboratory using ultrasonic velocities on shale core from varying depths and locations show the same increase in velocity anisotropy with confining pressure (Jones and Wang, 1981; Vernik and Liu, 1997).

3.4.2 Elastic tensors for Isotropic vs. Anisotropic Media

An isotropic material is a material that has the same physical properties regardless of the direction in which those properties are measured. The isotropic medium is defined by the relationship between stress (σ) and strain (ε): **σ=cε** where the elastic modulus tensor **c** for isotropic media has the following form (Thomsen, 1986):

$$\mathbf{c} = \begin{pmatrix} c_{33} & (c_{33}-2c_{44}) & (c_{33}-2c_{44}) & & & \\ (c_{33}-2c_{44}) & c_{33} & (c_{33}-2c_{44}) & & & \\ (c_{33}-2c_{44}) & (c_{33}-2c_{44}) & c_{33} & & & \\ & & & c_{44} & & \\ & & & & c_{44} & \\ & & & & & c_{44} \end{pmatrix} \tag{3.5}$$

where each c component is an independent elastic constant. In the case of isotropic media, the following relationships are true (Thomsen, 2002):

$$\begin{aligned} c_{11} = c_{33} &= \lambda + 2\mu \\ &= K + \frac{4}{3}\mu \end{aligned} \tag{3.6a}$$

$$c_{44} = c_{55} = \mu \tag{3.6b}$$

$$\begin{aligned} c_{12} = c_{13} = c_{23} &= \lambda \\ &= c_{33} - 2c_{44} \end{aligned} \tag{3.6c}$$

where λ and μ are Lamé's parameters. μ also represents the shear modulus, and K is the bulk modulus.

For transverse isotropy, five independent elastic constants are needed to describe the medium as opposed to the three required for isotropy: c_{11}, c_{33}, c_{44}, c_{66}, and c_{13}. In this case, the elastic tensor has the following form (Carrion et al., 1992):

$$\mathbf{c} = \begin{pmatrix} c_{11} & (c_{11}-2c_{66}) & c_{13} & & & \\ (c_{11}-2c_{66}) & c_{11} & c_{13} & & & \\ c_{13} & c_{13} & c_{33} & & & \\ & & & c_{55} & & \\ & & & & c_{55} & \\ & & & & & c_{66} \end{pmatrix} \tag{3.7}$$

These elastic constants have the following physical representations (Leaney, 1994):

$C_{11}=V^2_{Pv}$	vertical P-wave velocity
$C_{33}=V^2_{Ph}$	horizontal P-wave velocity
$C_{13}=V^2$	oblique propagation of P- and S-waves
$C_{55}=V^2_{s}$	vertical and horizontal S-wave velocity

Walkaway VSP surveys record data from a variety of offsets and azimuths into 3-component geophones or accelerometers. This type of survey is ideal for determining anisotropy parameters because the horizontal and vertical slowness can be extracted from the data (Leaney, 1994). The resultant values of anisotropy can be used to improve seismic processing and the understanding of a reservoir as a whole (Winterstein and Paulsson, 1990; Leaney, 1994).

3.4.3 Thomsen's Parameters vs. Schoenberg's Parameters

The elastic tensor constants for transverse isotropy have been used to define two sets of dimensionless parameters for anisotropy: Thomsen's parameters and Schoenberg's parameters. Thomsen's parameters, ε_T and δ_T, can be defined as follows (Thomsen, 1986):

$$\varepsilon_T = \frac{c_{11} - c_{33}}{2c_{33}} \tag{3.8a}$$

$$\delta_T = \frac{(c_{13} + c_{55})^2 - (c_{33} - c_{55})^2}{2c_{33}(c_{33} - c_{55})} \tag{3.8b}$$

The subscript "T" has been added to ε and δ by the author to prevent confusion with Schoenberg's parameters, which will be introduced shortly. ε_T is controlled by the vertical and horizontal P-wave velocities while δ_T is affected by both the P- and S-wave velocity. These parameters are of the same magnitude and reduce to zero for isotropic media (Thomsen, 1986). They are expressed as a percentage.

Schoenberg's parameters were initially introduced by Carrion et al. (1992). They are otherwise known as ellipticity (ε_p) and anellipticity (ε_A) and are defined as follows:

$$-1 < \varepsilon_P = \frac{c_{11} - c_{33}}{c_{11} + c_{33}} < 1 \tag{3.9a}$$

$$\varepsilon_A = \frac{(c_{11} - c_{55})(c_{33} - c_{55}) - (c_{13} + c_{55})^2}{(c_{11} - c_{55})(c_{33} - c_{55})} < 1 \tag{3.9b}$$

ε_p is a measure of the elliptical component of P-wave anisotropy and is comparable to Thomsen's ε_T (Leaney, 1994). ε_A is analogous to, but not the same as δ_T (Carrion et al., 1992). ε_p and ε_A are related to ε_T and δ_T through the following equations as presented by Schoenberg and de Hoop (2000):

$$\varepsilon_P = \frac{\varepsilon_T}{1 + \varepsilon_T} \tag{3.10a}$$

$$\varepsilon_A = \frac{2c_{33}}{c_{11} - c_{55}}(\varepsilon_T - \delta_T) \tag{3.10b}$$

ε_p is usually positive for VTI media, such as shale formations or finely layered lithologies, where P-waves propagate faster in the horizontal plane than the vertical plane

(Carrion et al., 1992). When ε_A=0, the P-wave slowness curve is an ellipse in the slowness plane, and the S-wave slowness curve is a circle (Carrion et al., 1992). Therefore, ε_A measures the deviation of the slowness surfaces from the elliptical P-wave and circular S-wave slowness curves (Carrion et al., 1992). As an example, if ε_A is a positive number then the P-wave slowness curve will bulge outward and the S-wave slowness curve will bulge inward at 45^o (Leaney, 1994). The geometric expression of ε_A in slowness curves makes ε_A easier to interpret than Thomsen's δ_T (Horne and Leaney, 2000). Figure 3.10 illustrates the P- and S-wave slowness curves for isotropic media, elliptically anisotropic media, and a shale sample.

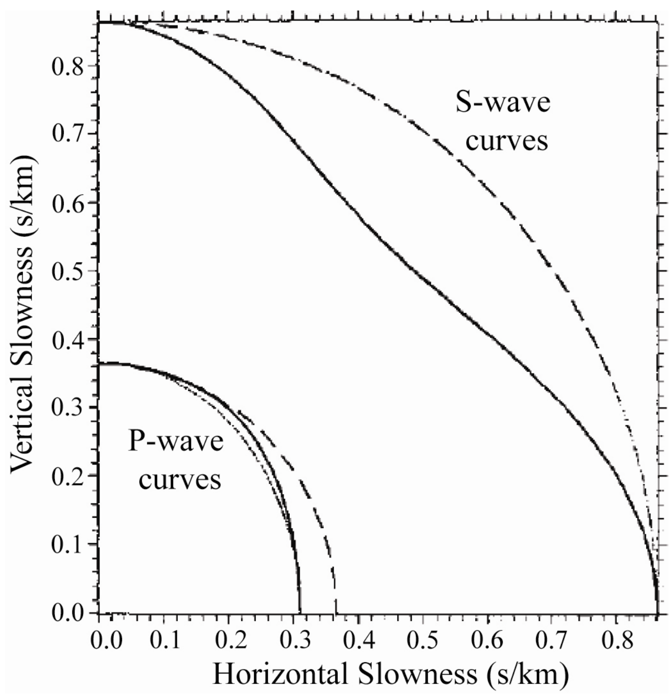

Figure 3.10: P- and S-wave slowness curves for an isotropic medium (dashed), elliptically anisotropic medium (dotted), and data measured from a shale sample (from Leaney, 1994).

Chapter Four: Baseline Vertical Seismic Profile Data Processing

4.1 Introduction

The VSP data were processed as three separate walkaway surveys using the same processing flow. Parameter testing was conducted on Line 3 because it passes closest to the monitor well (Figure 4.1). Hodogram analysis showed that the distribution of energy between the z-, y-, and x-components of the data were remarkably consistent. The data were rotated into a true earth frame prior to wavefield separation.

An anisotropic velocity model was created using well logs from a nearby production well and the local anisotropy parameters: ellipticity and anellipticity. The well logs were Backus averaged and blocked at 5 m intervals prior to inverting the model for anisotropy. The anisotropic velocity model was used both for the 3D wavefield separation and for the time migrations. The P- and Sv-wave data were processed through to pre-stack time migrations for all of the lines. Figure 4.2 illustrates the processing flow used for the VSP data.

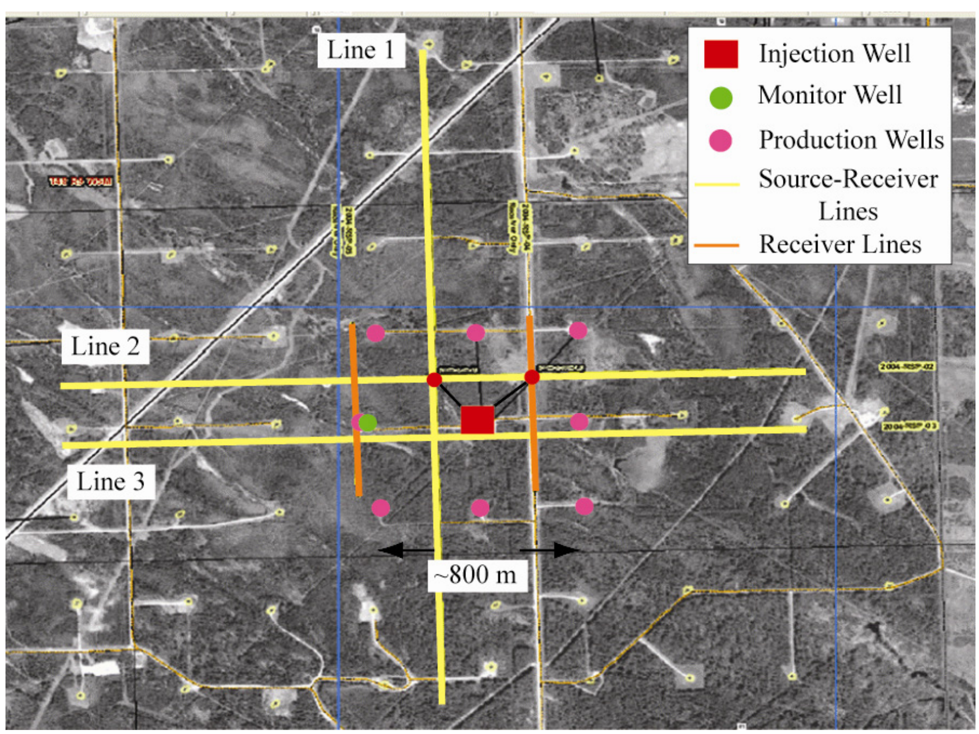

Figure 4.1: Aerial view of the Penn West CO_2 injection site.

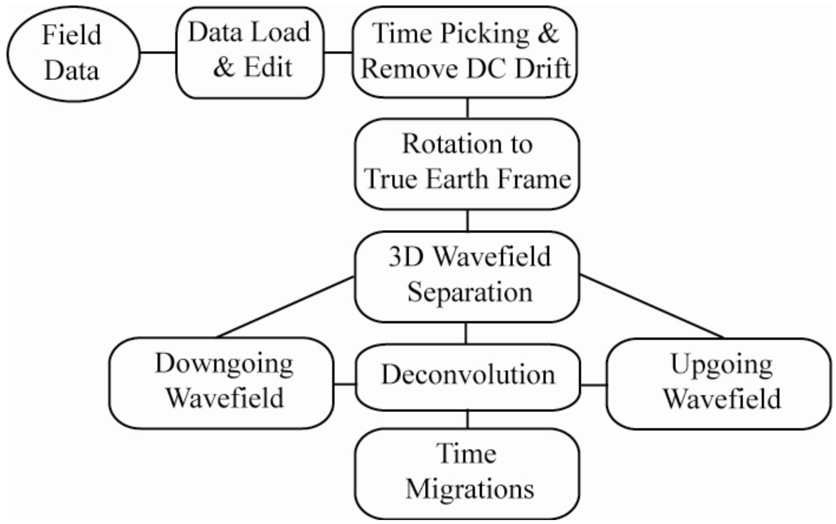

Figure 4.2: VSP processing flow.

4.2 Raw Data

The topography in the survey area ranges between 881 and 902 m above mean sea level. A datum of 910 m was used for the surface seismic data processing, so the VSP data was corrected to the same datum. A low-cut filter was used to remove the observed DC bias in the data, and then the direct arrival was picked on all three components. In this case, the direct arrival is defined as the first zero-crossing on a trace. The raw z-, y-, and x-components of the data for receivers 1, 4, and 8 from Lines 3, 2 and 1 can be seen in Figures 4.3, 4.4, and 4.5, respectively.

As was discussed in Section 3.4, components of P- and S-waves propagate parallel and perpendicular to bedding. In the case of flat-lying beds, a component of the waves will propagate perpendicular to bedding and travel in the vertical plane while another will propagate parallel to the bedding and travel in the horizontal planes. For near offset shots, the z-component of the data is predominantly composed of vertically propagating P-wave energy, and very little energy is recorded on the horizontal or y- and x-components of the data. In the case of far offset shots, the z-component of the data will contain vertically propagating P- and S-wave energy. The amplitudes recorded on the x- and y-components of the data are also much higher because of the contribution from vertically propagating S-wave energy and horizontally propagating P-wave energy.

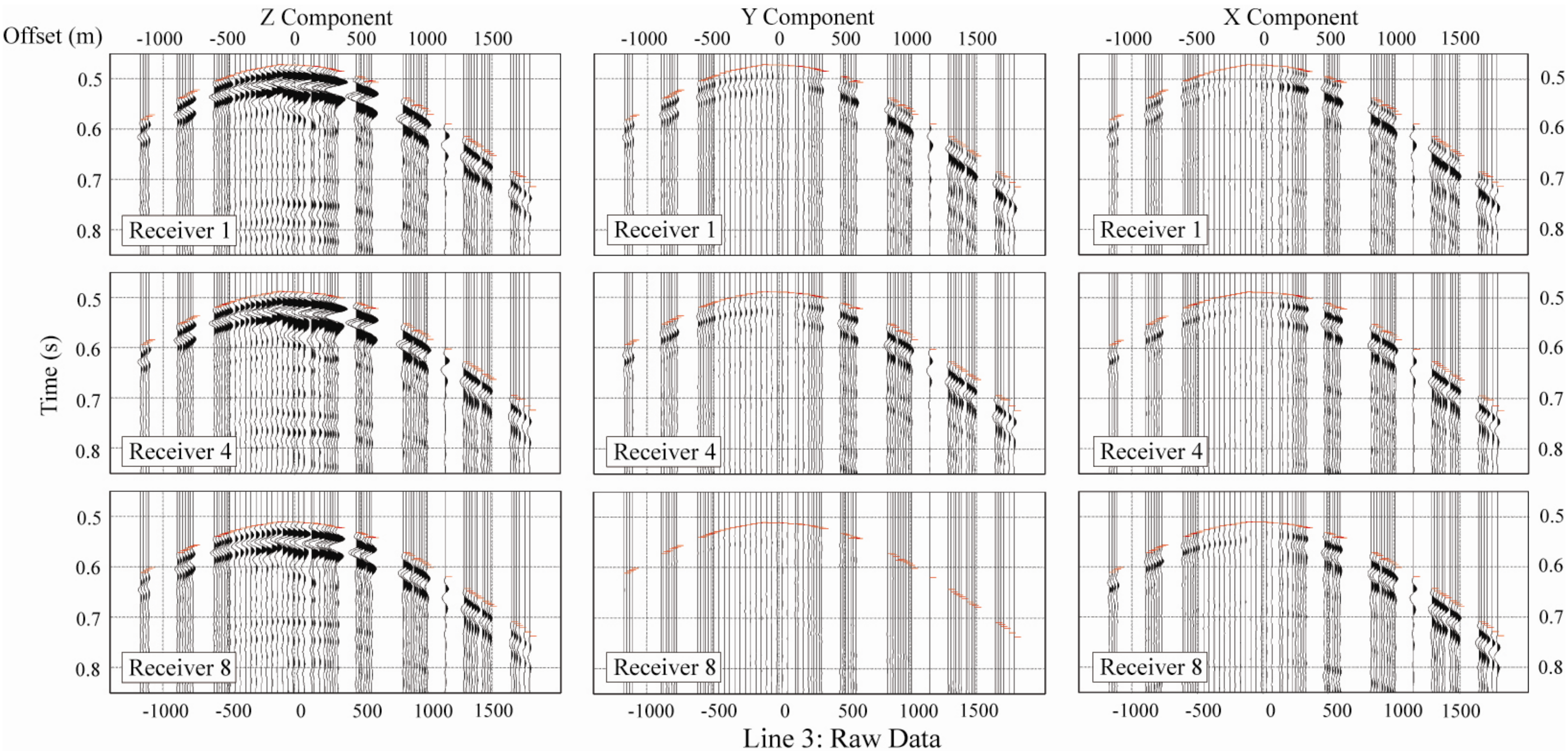

Figure 4.3: Raw z-, y-, and x-components from receivers 1, 4, and 8 for Line 3 in true amplitude display. Direct arrival time picks are in red. Note the low amplitudes at the near offsets for the x- and y-components.

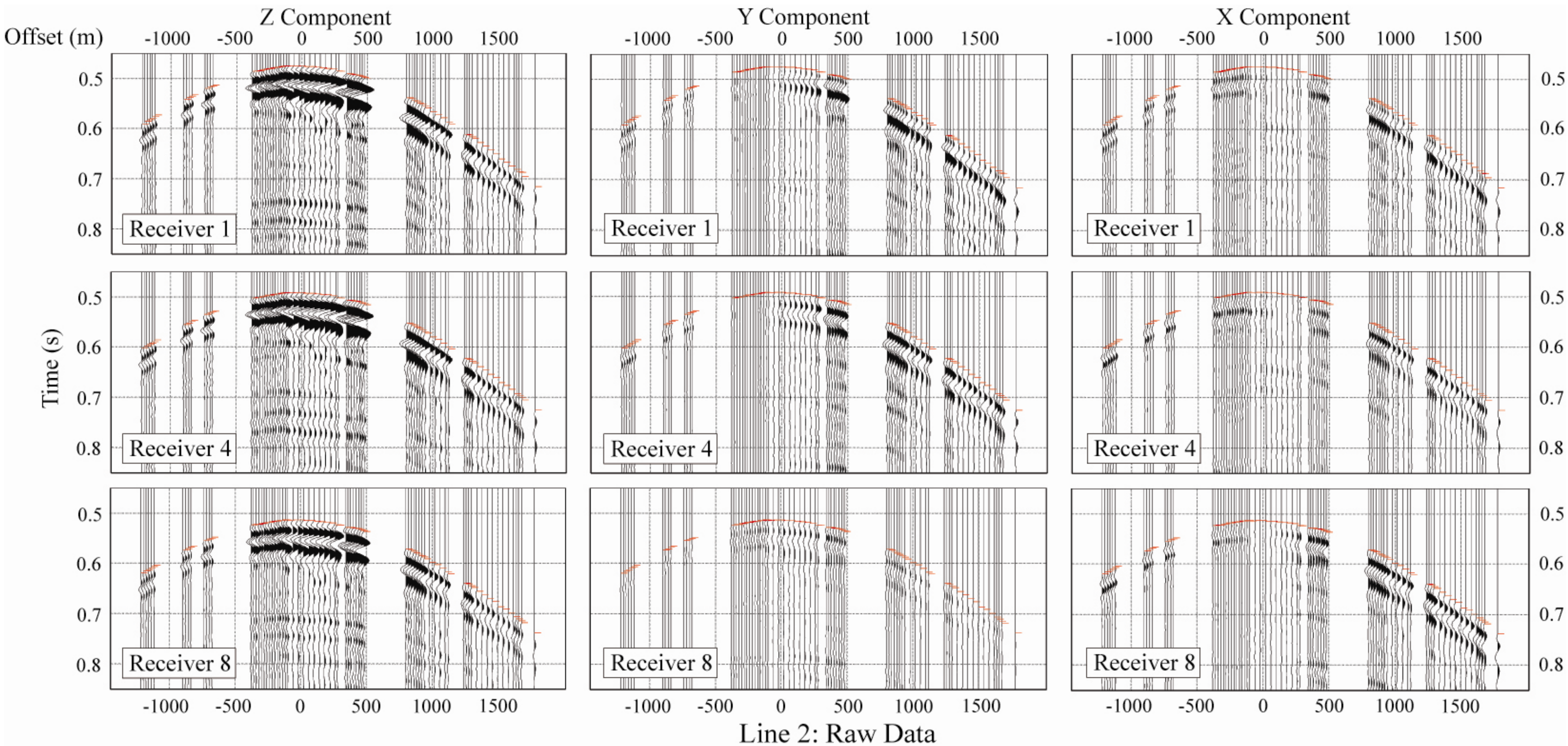

Figure 4.4: Raw z-, y-, and x-components from receivers 1, 4, and 8 for Line 2 in true amplitude display. Note the flip in the direct arrival orientation on the x- and y-components at zero offset.

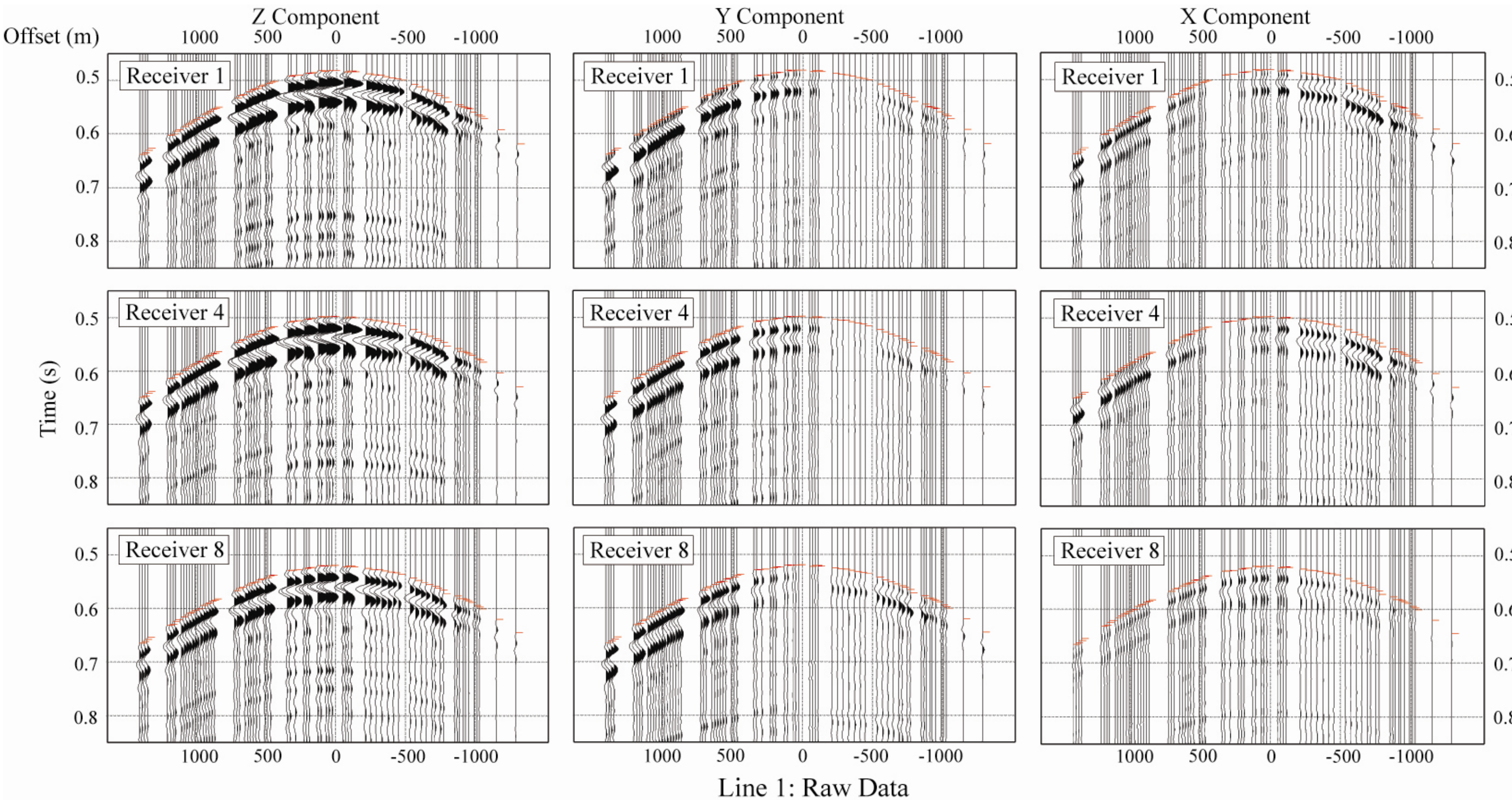

Figure 4.5: Raw z-, y-, and x-components from receivers 1, 4, and 8 for Line 1 in true amplitude display. Note the flip in the direct arrival orientation on the x- and y-components at zero offset.

4.3 Geophone Orientation

After the installation of the geophones in the well, the exact orientation of each geophone is unknown as was discussed in Section 1.2.3. In the case of a vertical well, this uncertainty does not have a strong effect on the vertical component of the data, but it does have a strong effect on the horizontal components. For initial processing, one of the horizontal components of the data must be aligned in the direction of the maximum energy, which is usually in the source-receiver plane for a particular shot.

Hodogram analysis uses the direct arrival P-wave energy to orient the horizontal components of the data to the source-receiver plane. Hodogram analysis determines the motion of the direct P-wave arrival within a small time window in the x, y, and z data; this information is used to orient the data to the source-receiver plane. The hodograms from the raw x-, y-, and z-components of the data demonstrated that the P-wave energy fell into distinct polarization planes (Figure 4.6). At the far offsets, the energy was evenly distributed between the vertical and horizontal components of the data while the energy at the near offsets fell almost entirely in the vertical component. This dataset shows remarkably consistent distribution of energy between the three components for each shot.

The 3D wavefield separation (Section 4.5) requires the input data be oriented to the true earth frame (north, east, and vertical components). The advantage of using the true earth frame over the standard hodogram analysis and data rotations is that it deals with 3D geometries better. Figure 4.7 illustrates how the dip and azimuth angles are calculated using the longitudinal and transverse components of the data; these angles are used to determine the relative bearing angle from north for each source-receiver pair. Figure 4.8 shows the average geophone orientations based on the relative bearing angle calculations from all three of the walkaway lines. The relative bearing angle, dip, and azimuth are input to trigonometric equations to rotate the data into the true earth frame.

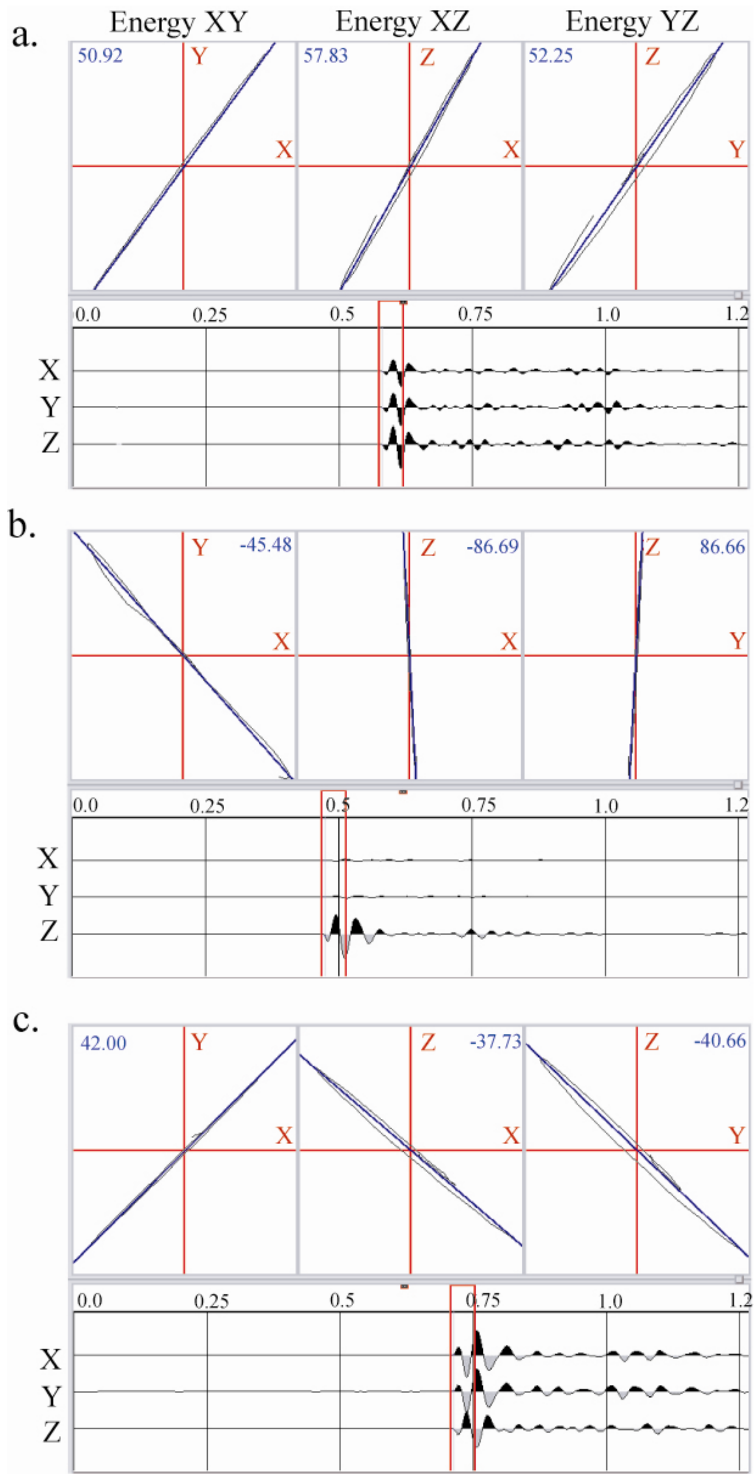

Figure 4.6: Hodogram analysis from three offsets along Line 3: (a.) -1170 m, (b.) -10 m, and (c.) 1788 m. The orientation of the direct P-wave arrival rotates as the source moves from west to east past the borehole. The numbers in blue represent the angle between the horizontal axis and the best fit line.

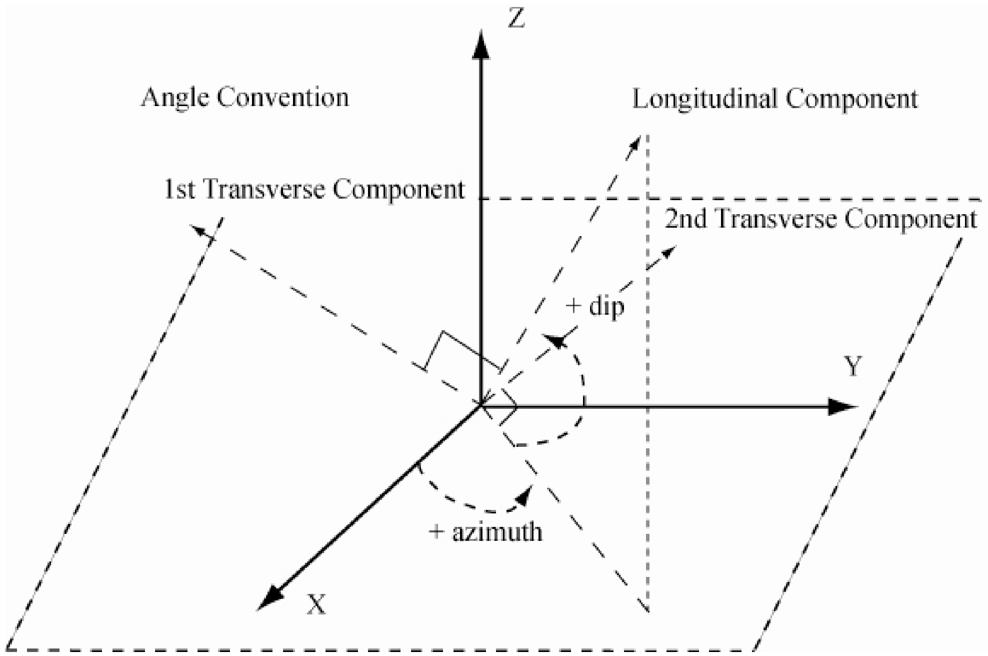

Figure 4.7: Angle convention for calculating dip and azimuth for each shot and receiver pair.

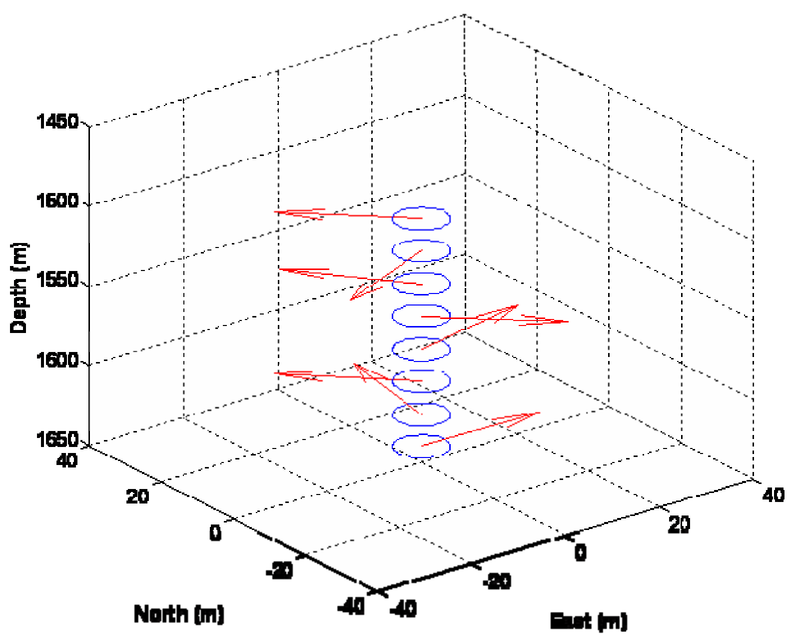

Figure 4.8: Average geophone orientations after installation as determined from the relative bearing calculations (Courtesy of H. Bland).

Figure 4.9 shows the z-, y-, and x-components of two common shot gathers from Line 3 before and after the data have been rotated into the true earth frame. Before rotation into the true earth frame, the horizontally propagating energy is clearly aligned in different directions. The traces have different orientations at each geophone, and the horizontally propagating energy is evenly divided between the x- and y-components of the data. After the data have been rotated into the true earth frame, the traces in the x- and y-components have consistent amplitudes. Line 3 strikes in an east-west direction, so the horizontally propagating energy primarily appears in the east-west component of the data for this line. As the distance from the monitor well increases, the amplitudes in the east-west component of the data increase, and the amplitudes in the north-south component decrease.

Figure 4.10a and b are examples of common shot gathers from Line 1. The common shot gather in Figure 4.10a is from a location very close to the gather in Figure 4.9a. When the rotated gathers are compared, they show similar amplitudes on the east-west and north-south components of the data. The traces in the east-west components of the data also share some of the same characteristics. The common shot gather in Figure 4.10b is located at the north end of the line. At this offset, the first arrival P-wave energy is predominantly on the vertical and north-south components of the data, as the source locations on Line 1 strike in a north-south direction.

Figure 4.11a and b are a comparison of two common shot gathers from similar east-west offsets on Lines 3 and 2. The horizontally propagating energy is primarily in the east-west component of the data. However, the orientation of the traces in the north-south component of the data is different for Lines 3 and 2 because the lines lie on opposite sides of the monitor well.

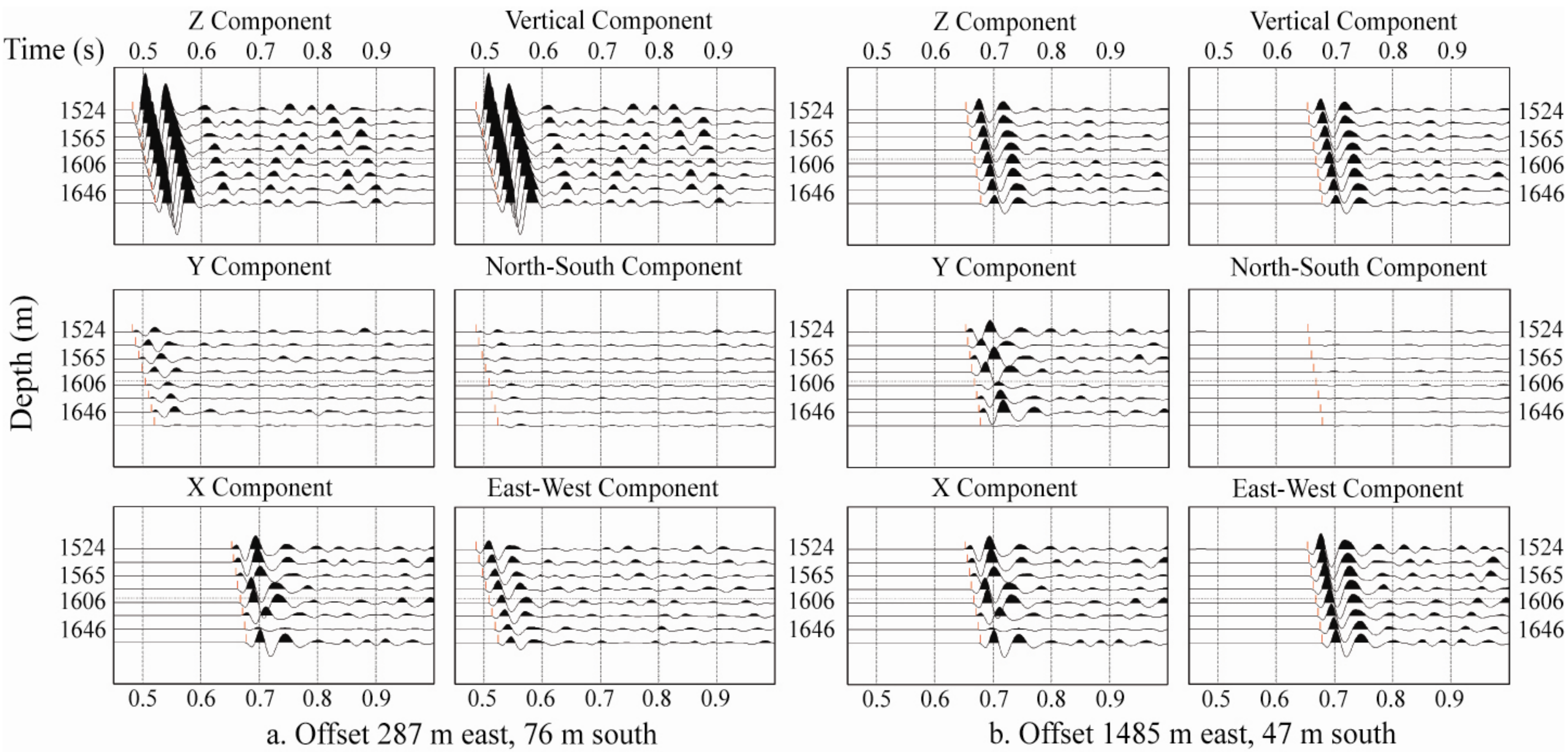

Figure 4.9: Comparison of common shot gathers from Line 3 before (left) and after (right) rotation to the true earth frame. (a.) offset 237 m east and (b.) offset 1485 m east. Line 3 strikes in an east-west direction, so the horizontally propagating energy lies primarily in the x- and east-west components of the data. True amplitude display.

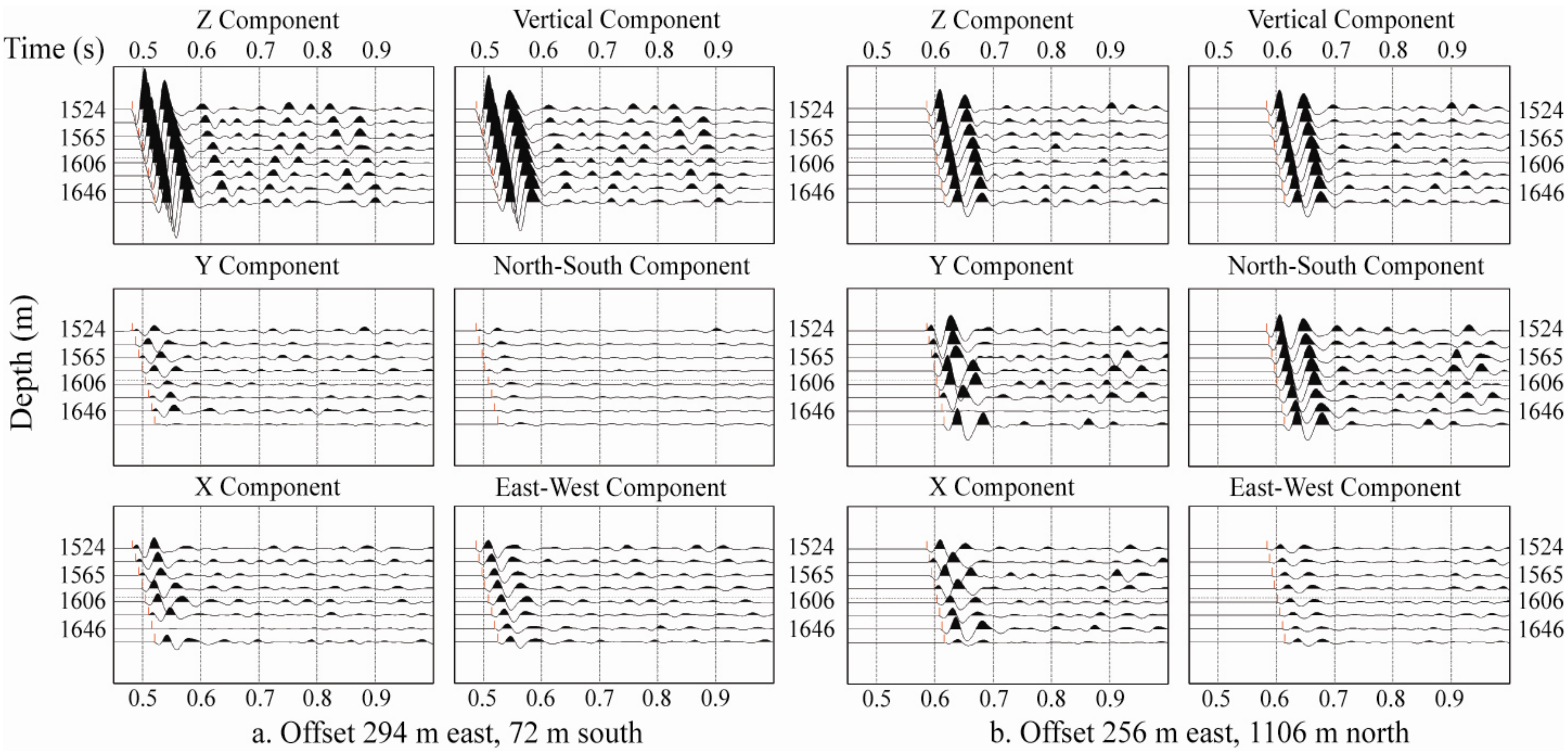

Figure 4.10: Comparison of common shot gathers from Line 1 before (left) and after (right) rotation to the true earth frame. (a.) offset 72 m south and (b.) offset 1106 m north. Figures 4.8a and 4.9a show very similar characteristics and amplitudes because the two source locations are very close to each other. True amplitude display.

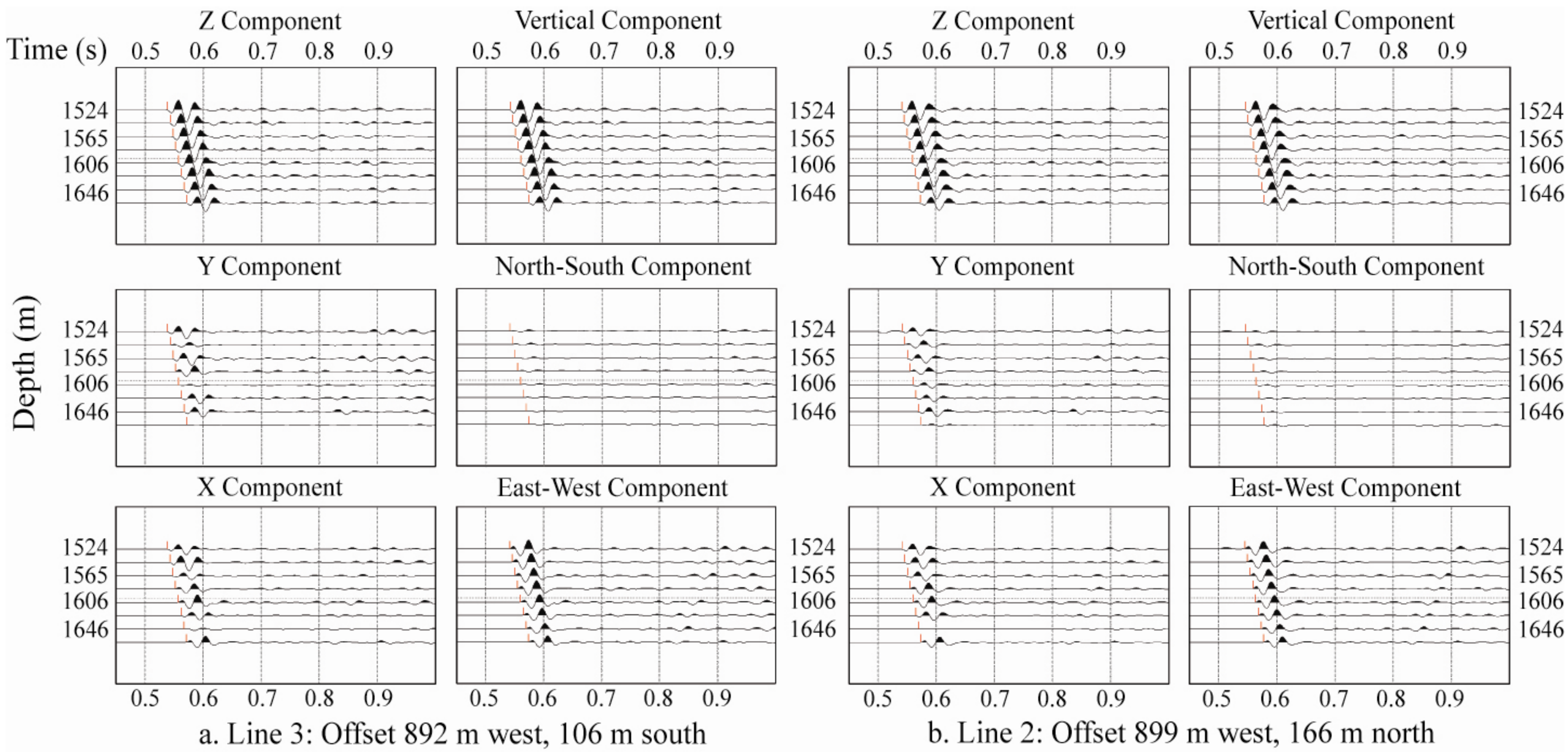

Figure 4.11: Comparison of common shot gathers from (a.) Line 3: offset 892 m west and (b.) Line 2: offset 899 m west before (left) and after (right) rotation to the true earth frame. The north-south components have different orientations after rotation because the lines are located on either side of the monitor well. True amplitude display.

4.4 Source Statics

Heterogeneities and velocity variation in the near surface, and rapid changes in ground elevation result in traveltime deviations that vary from source location to source location. Static corrections used to remove these traveltime variations from land and shallow marine seismic data. Reflection events should be more continuous and significant false structures should be eliminated once the static corrections have been applied (Yilmaz, 2001).

Veritas, the surface seismic contractor, calculated the 3D source statics for the surface seismic data. After the VSP data were rotated to the true earth frame, the 3D source statics were applied to the data. This is similar to the methodology used for the 3D VSP acquired for the Blackfoot Field (Gulati et al., 2004).

4.5 Velocity Modelling and Anisotropy Analysis

An anisotropic velocity model was built for the wavefield separation and migrations. P- and S-wave sonic logs from a production well about 60 m away from the observation well were used as a starting point for the initial velocity model. A density log was not acquired in the production well, so a density log was generated using Gardner's Equation (Gardner et al., 1974). The initial velocity model extended to 5000 m depth. However, the well logs were acquired to a depth of about 1660 m. Beneath 1660 m, the log values were made to increase linearly with depth. The P-wave sonic log was calibrated using the source location on Line 3 closest to the monitor well.

The logs were Backus averaged and blocked at 5 m intervals. The purpose of Backus averaging is to upscale the log measurements to seismic wavelengths while preserving the gradational changes in the logs themselves (Lindsay and Van Koughnet, 2001). Backus averaging averages the values of V_p, V_s, and density from a series of thin layers to a value that represents a single consolidated layer. Elastic moduli are then derived from the average values. The blocking interval should be between $1/10^{th}$ and $1/8^{th}$ of the wavelength at the reservoir (Tcherkashnev and Leaney, 2002). For this dataset, a dominant wavelength of 53 m was calculated based on a P-wave velocity of 3720 m/s at the reservoir and a dominant frequency of 70 Hz.

Comparisons of the direct arrival traveltimes calculated from the velocity model and the measured traveltimes from the data can be used to determine the accuracy of the velocities in a model for a particular dataset. Traveltime residuals are calculated by subtracting the modelled traveltimes from the measured traveltimes. If the velocities in the model satisfy the data then there should be zero traveltime residuals at all offsets. However, the traveltime residuals from Line 3 increase with offset. This indicates that the measured traveltimes are faster than the modelled traveltimes. Figure 4.12 demonstrates that there is zero traveltime residual at zero offset; this indicates that the vertical velocities in the model are accurate for this dataset. However, the residual traveltimes increase with offset indicating that anisotropy is affecting the data to some degree. Most of the receivers are located in the black shale of the Wapiabi Formation, and it is realistic to expect the shale to exhibit anisotropy (Section 3.4).

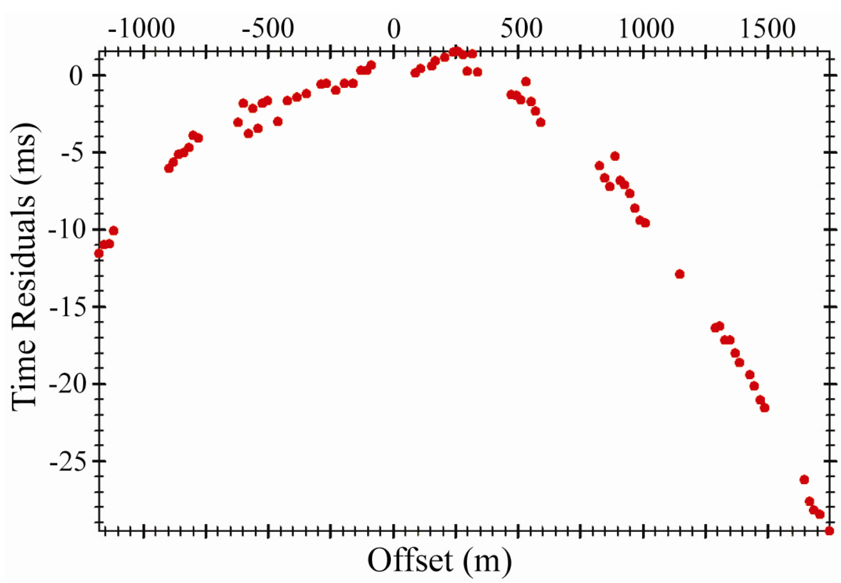

Figure 4.12: Traveltime residuals (measured – modelled) from Line 3 for the initial isotropic velocity model.

Slowness and polarization angles were used to determine local anisotropy at the receivers. If the parameters for local anisotropy could be established, they can be used to limit the values for anisotropy obtained in the inversion, and the resulting model will improve the wavefield separation (Leaney, 2002). The apparent slowness and polarization angles were derived from the data using parametric wavefield decomposition (PWD) as developed by Leaney and Emersoy (1990). PWD assumes that the data is composed a small number of local plane wavefields where the number of wavefields is less than the number of receivers. It works on the premise that the time shifts between receivers become linear phase shifts in the frequency domain as defined by Equation 4.1:

$$\exp(-i\omega \Delta z_m s_n) \tag{4.1}$$

where ω is angular frequency, Δz_m is the distance between receivers, and s_n is apparent slowness of the n[th] plane wave. Each phase shift of the data can be broken into x- and z-components by a unit projection vector $\mathbf{h}_n$ for P-waves:

$$h_n = \begin{pmatrix} \sin\theta_n \\ +-\cos\theta_n \end{pmatrix} \tag{4.2}$$

and for S-waves:

$$h_n = \begin{pmatrix} -\cos\theta_n \\ -+\sin\theta_n \end{pmatrix} \tag{4.3}$$

where the + and – indicate the upgoing and downgoing waves in the z-component of the data. In order to separate the wavefields, the following matrix is used:

$$\begin{pmatrix} h_1 e^{-i\omega\Delta z_1 s_1} \ldots\ldots\ldots\ldots h_N e^{-i\omega\Delta z_1 s_N} \\ \ldots\ldots\ldots\ldots\ldots\ldots\ldots\ldots\ldots\ldots \\ \ldots\ldots\ldots\ldots\ldots\ldots\ldots\ldots\ldots\ldots \\ h_1 e^{-i\omega\Delta z_M s_1} \ldots\ldots\ldots\ldots h_N e^{-i\omega\Delta z_M s_N} \end{pmatrix} \begin{pmatrix} w_1 \\ .. \\ .. \\ w_N \end{pmatrix} = \begin{pmatrix} d_1 \\ .. \\ .. \\ d_M \end{pmatrix} \tag{4.4}$$

where $d_1 \ldots d_M$ is the total wavefield recorded at the receivers 1 to M while $w_1 \ldots w_N$ represents the plane wavefields at frequency ω that are the desired output. Equation 4.4 is solved for all available frequencies, and an inverse Fourier transform is used to transform the separated wavefield back to the time domain.

Therefore, each shot processed with PWD yields a slowness component and a polarization angle for the downgoing and upgoing P-wave, and downgoing and upgoing converted S-wave. Once the slowness and polarization angles were obtained, slowness-polarization inversion, as defined by Horne and Leaney (2000), was used to determine the anisotropy parameters at the receivers. The inversion allowed the anisotropy parameters to increase with depth, thus honouring the assumption that anisotropy increases with compaction (Section 3.4).

Figure 4.13a and b show crossplots of the slowness and polarization components for each of the four wavefields at receiver 4; the phase of the S-wavefield has been rotated by 90^{o} for the purposes of display. The data points were initially inverted for an isotropic model and a second time for an anisotropic model. The program allowed outlying data points to be rejected from the analysis. It is clear from Figure 4.13b that the anisotropic model fits the data better than the isotropic model. The average values obtained for ellipticity and anellipticity based on the inversions from each of the receivers were 0.123 and 0.116; this translates to epsilon and delta values of 0.14 and 0.07. The values for ellipticity and anellipticity were then included in the velocity model for the inversion of first arrival times.

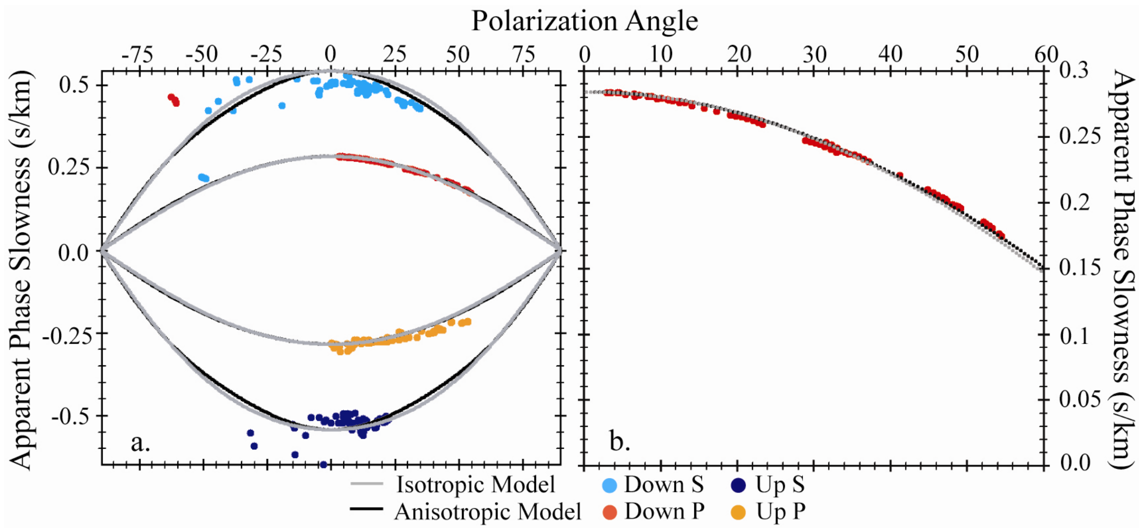

Figure 4.13: Example of the anisotropy inversion using the slowness and polarization measurements derived from the parametric inversion at receiver 4. The data points from the downgoing P-wave data tend to fall on the anisotropic model. (a.) all of the data points. (b.) detail of the downgoing P-wave data points.

Figure 4.14 is an example of the P-wave ray-tracing through the anisotropic velocity model for receiver 1 and an interface below the receiver array. The traveltime residuals were calculated for the anisotropic velocity model for comparison to the initial isotropic model (Figure 4.15). The traveltime residuals are now less than 3 ms across the entire line.

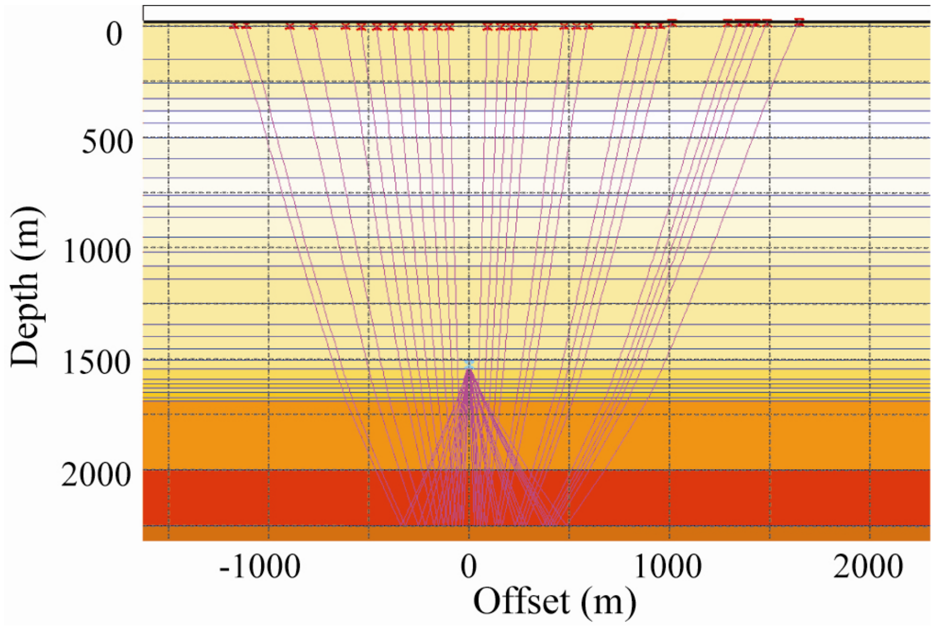

Figure 4.14: P-wave ray tracing through the anisotropic velocity model for receiver 1, Line 3.

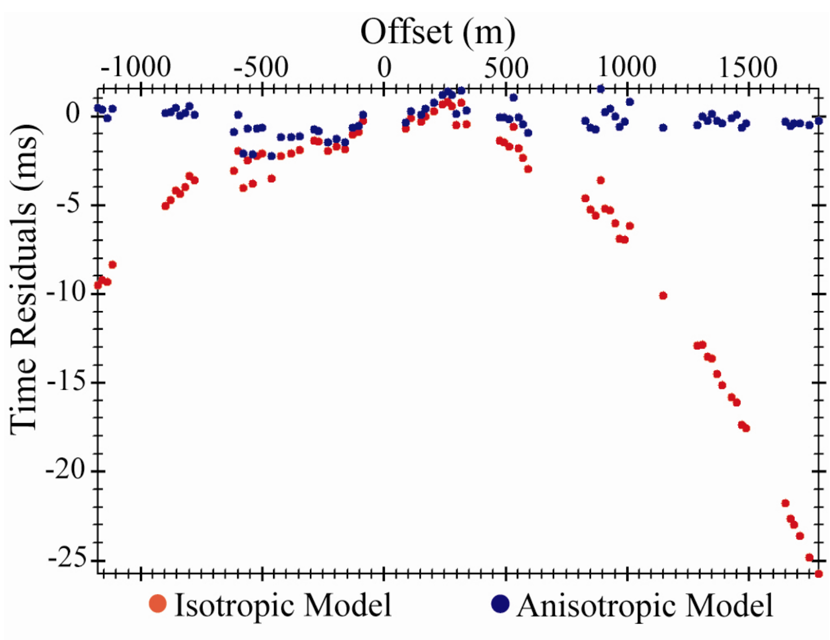

Figure 4.15: Traveltime residuals (measured – modelled) for the isotropic and anisotropic velocity models from Line 3. The residuals are less than 3 ms after inversion for anisotropy.

4.6 Wavefield Separation

The signal recorded by the geophones in a well-bore is a total wavefield that may consist of P-wave and converted S-wave direct arrivals, multiple energy, and upgoing P-wave and converted S-wave events (Figure 4.16). The reflected P-wave and converted wavefields provide the most information about the subsurface and must be separated from the downgoing wavefields early in the processing sequence.

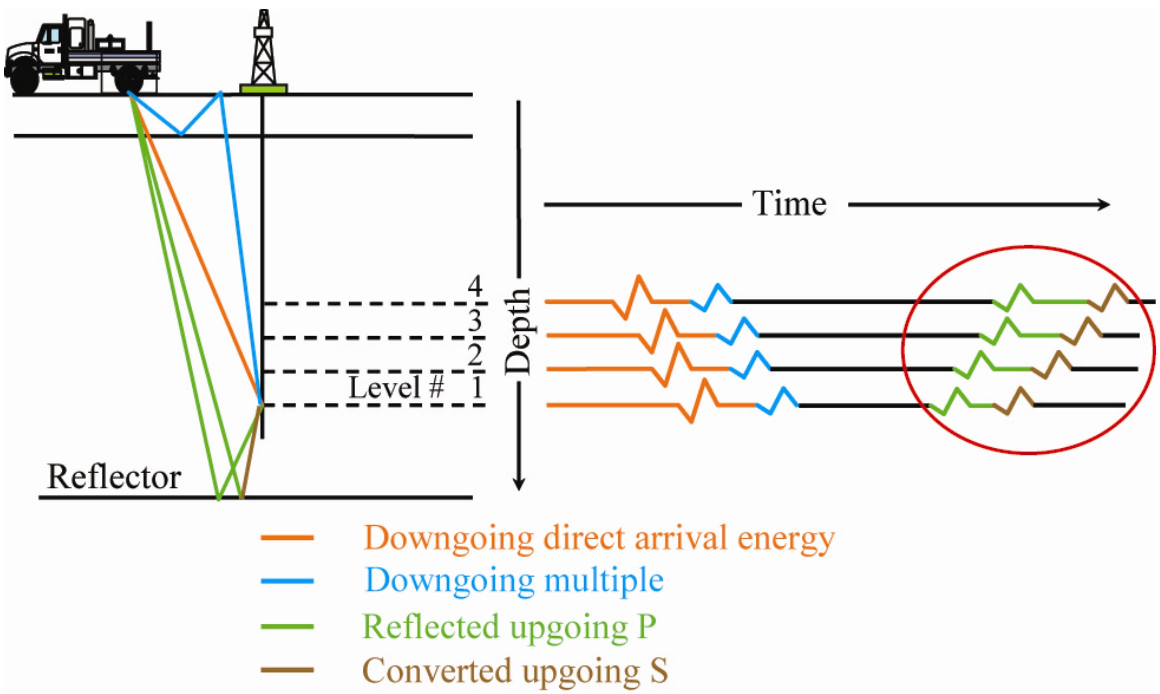

Figure 4.16: The total wavefield recorded by the geophones in a well. The upgoing P-wave and converted S-wave reflections provide the most information about the subsurface (Courtesy of Schlumberger).

A 3D wavefield separation method developed by Leaney (2002) was used in the main processing flow and is related to PWD. However, where PWD assumes that the total wavefield is made up of a small number of plane waves, the 3D technique assumes that the total wavefield is made up of the following scalar wavefield components: down and upgoing P, down and upgoing Sv, and down and upgoing Sh. Given the desired plane waves, their propagation angles, and an anisotropic velocity model, the slowness and polarization vectors are computed for each plane wave through forward modelling

(Leaney, 2002). A linear system is solved at each frequency to yield the scalar plane wave amplitudes, which are used to construct the separate wavefields.

Equation 4.5 is the basis for this method:

$$\mathbf{d}(\mathbf{x}_m, \omega) = \sum_{n=1}^{N} a_n \mathbf{h}_n e^{i\omega(s_n \bullet x_m)} \tag{4.5}$$

where **d** is the vector of 3C data, x_m is the mth 3C receiver in Easting, Northing, and depth, ω is angular frequency, s_n is the slowness vector, and a_n is complex amplitude.

The 3D wavefield separation has the following benefits over PWD: it can separate the Sv- and Sh-wavefields, it deals with irregular source-receiver geometries, and it can incorporate anisotropy into the wavefield separation. The frequency range used for the wavefield separation was 8 to 100 Hz. Figure 4.17 to 4.19 are examples of common receiver gathers for the separated upgoing P- and Sv-wavefields from Lines 3, 2, and 1. There is more energy at the near offsets in the Sv-data from Lines 2 and 1 because the data was rotated to the true earth frame and because these lines are further offset from the monitor well.

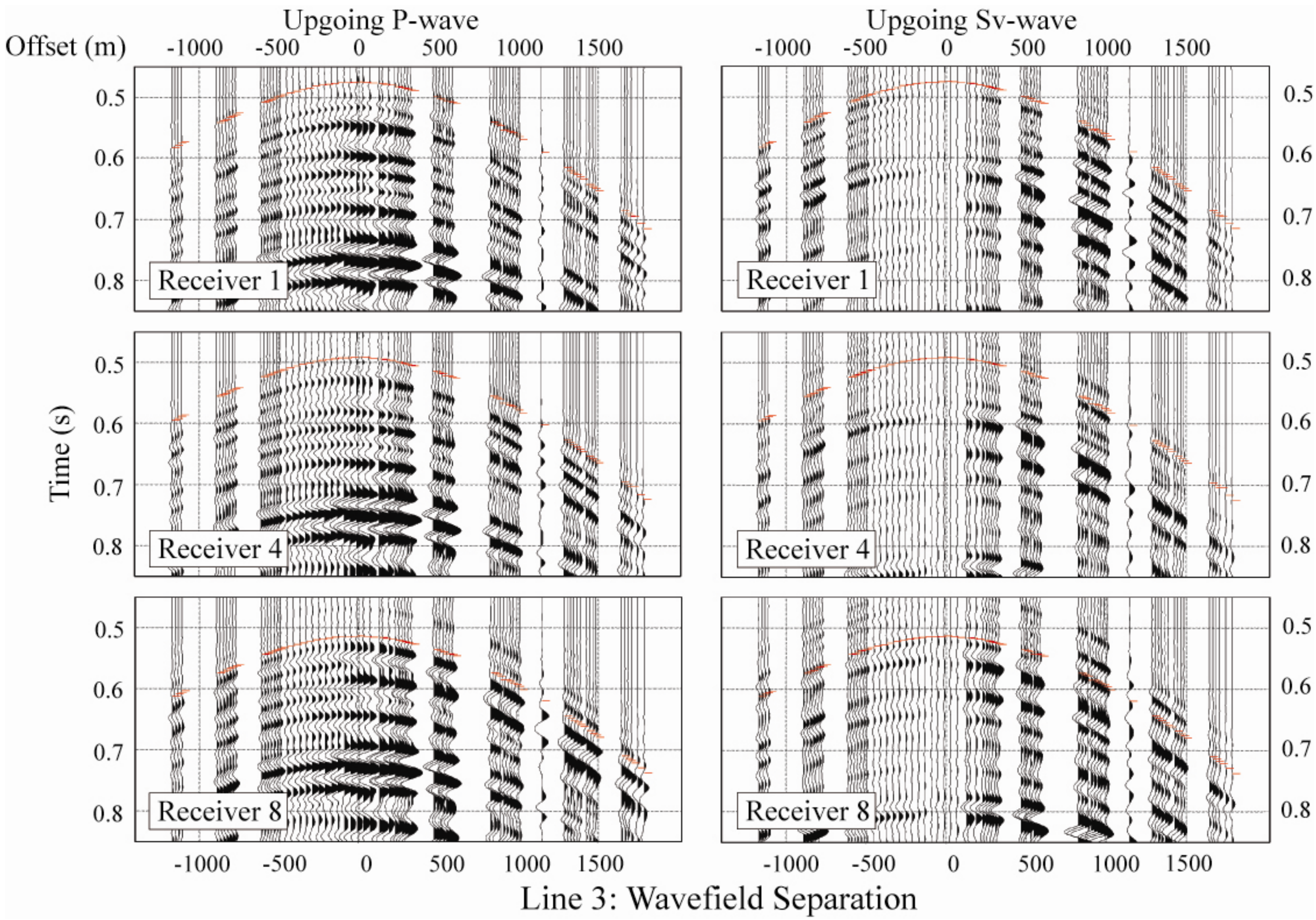

Figure 4.17: Upgoing P- and Sv-wavefields from receivers 1, 4, and 8 for Line 3 after wavefield separation. True amplitude display.

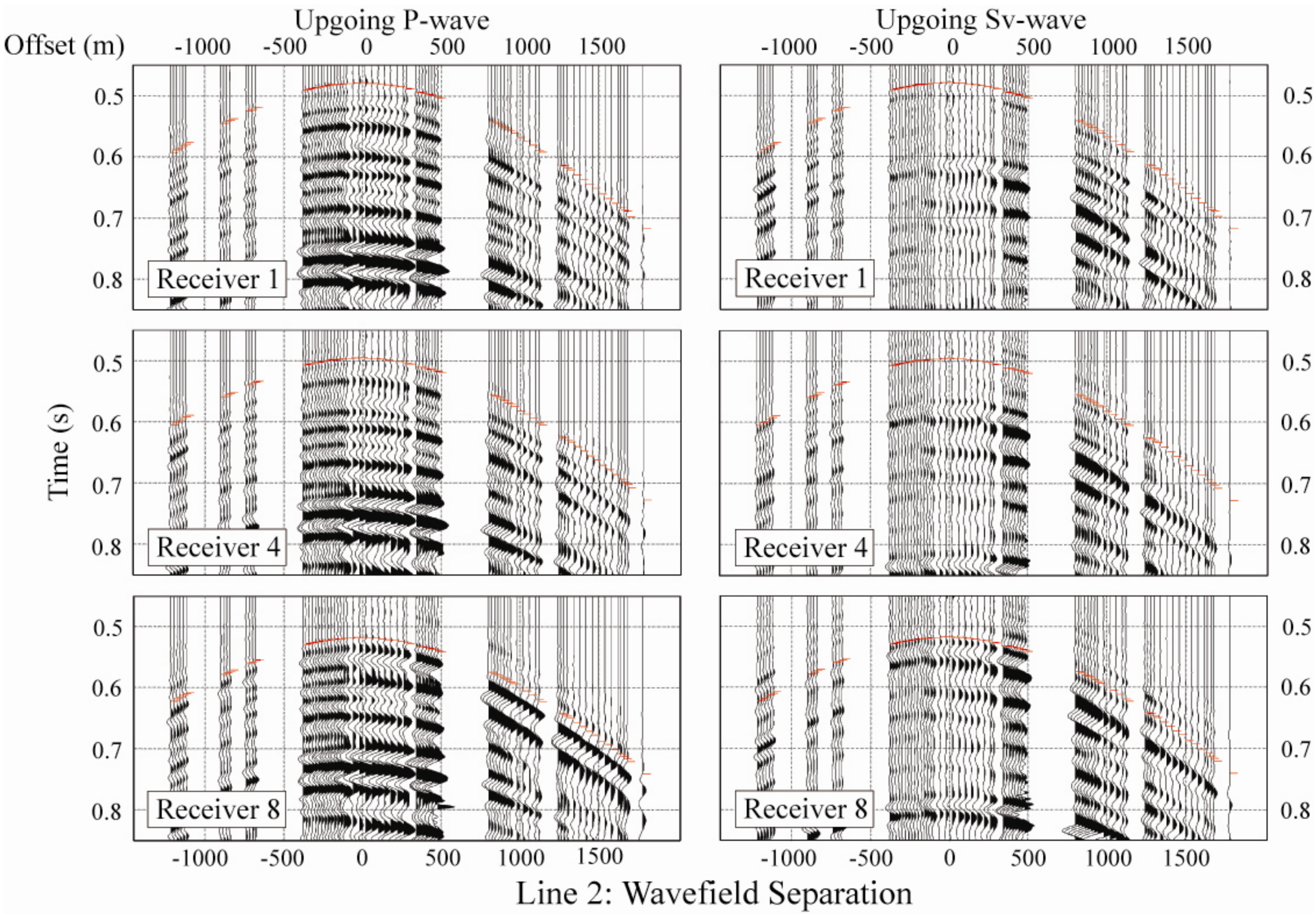

Figure 4.18: Upgoing P- and Sv-wavefields from receivers 1, 4, and 8 for Line 2 after wavefield separation. True amplitude display.

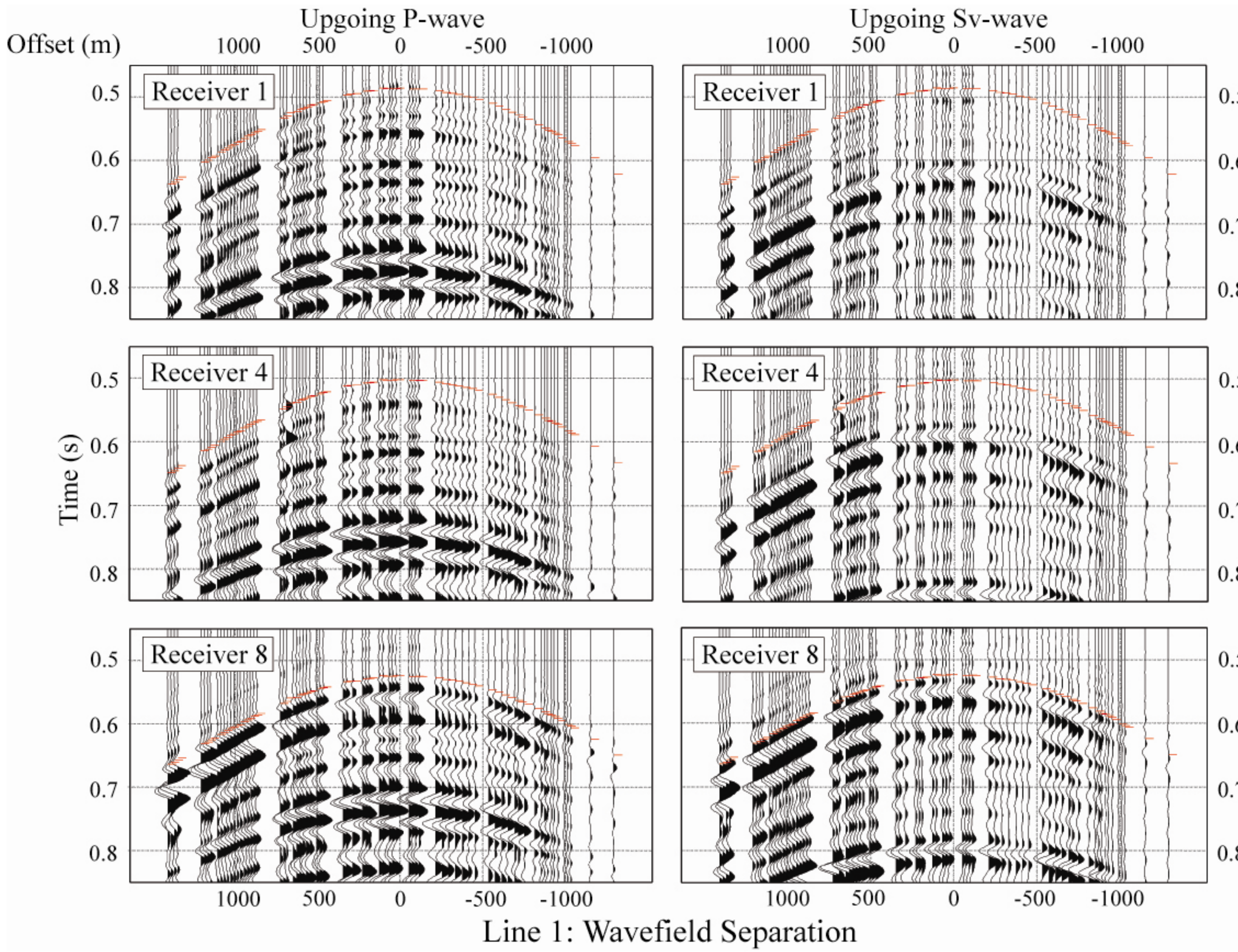

Figure 4.19: Upgoing P- and Sv-wavefields from receivers 1, 4, and 8 for Line 1 after wavefield separation. True amplitude display.

4.7 Deconvolution

The seismic wavefield that is recorded at the receivers is not simply the impulse response of the earth but rather a combination of effects including the earth's impulse response, multiple energy, the source signature, receiver coupling and response, and noise. Ideally, one would like to remove the filtering effects of earth and retain the reflectivity series, which can be modeled as the convolution of the earth's impulse response and the source wavelet (Yilmaz, 2001). Deconvolution attempts to remove the filtering effects of the earth and to output the original reflectivity series by compressing the effective source wavelet to a spike and removing multiples (Yilmaz, 2001). For this dataset, waveshaping deconvolution, or inverse filtering, was applied. This deconvolution operator attempts to collapse the direct downgoing wavefield to a spike and to remove the effect of the source signature from the upgoing wavefields as well as matching the amplitude-frequency response of adjacent traces. The deconvolution operator is not as effective for reflections from beneath the receiver array where no direct arrival has been recorded.

The P-wavefield was deconvolved using a frequency band from 8 to 100 Hz while the Sv-wavefield was deconvolved using a frequency band from 8 to 90 Hz. A window of 1.0 s and 1% whitening was used in the deconvolution process. The upgoing wavefields were normalized using the deconvolved downgoing P-wavefield. Both upgoing P- and Sv-wavefields were muted before the direct arrivals and resampled to 2 ms prior to migration. Figures 4.20, 4.21, and 4.22 are examples of the deconvolved upgoing P- and Sv-wavefields after normalization and muting from Lines 3, 2, and 1.

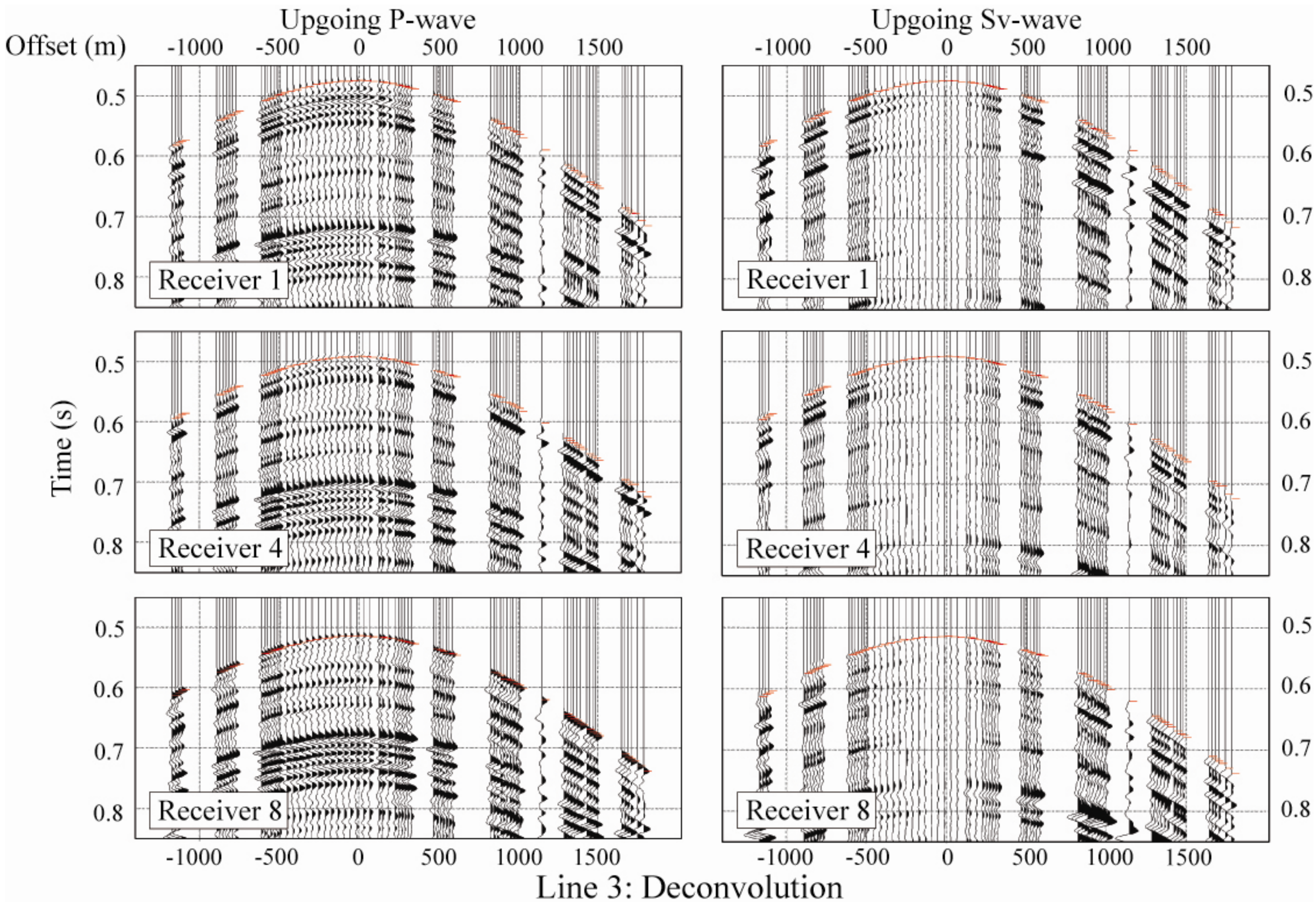

Figure 4.20: The deconvolved upgoing P- and Sv-wavefields from Line 3. Wavefields have been muted before the first arrival picks and normalized with the deconvolved downgoing P-wavefield.

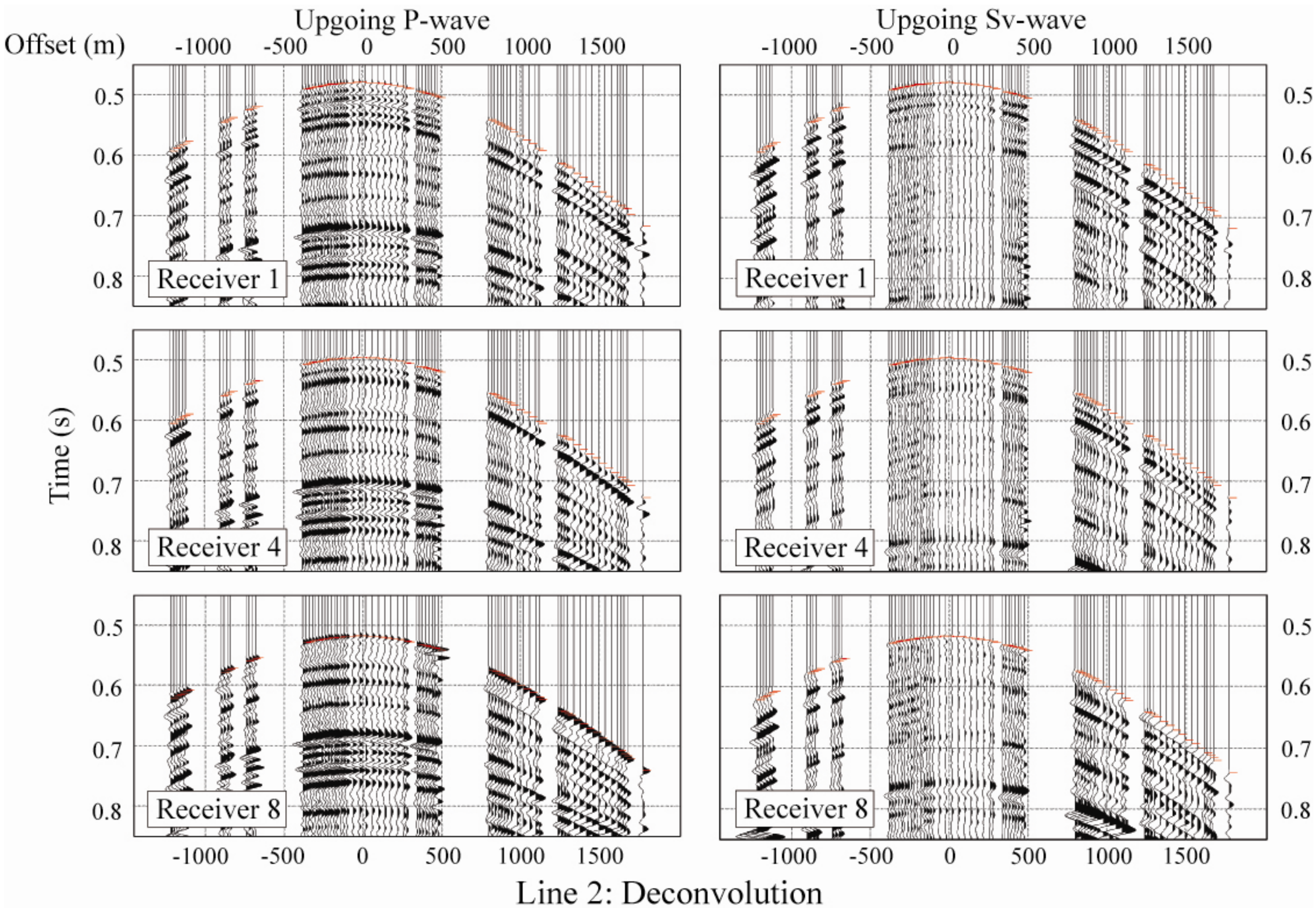

Figure 4.21: The deconvolved upgoing P- and Sv-wavefields from Line 2. Wavefields have been muted before the first arrival picks and normalized with the deconvolved downgoing P-wavefield.

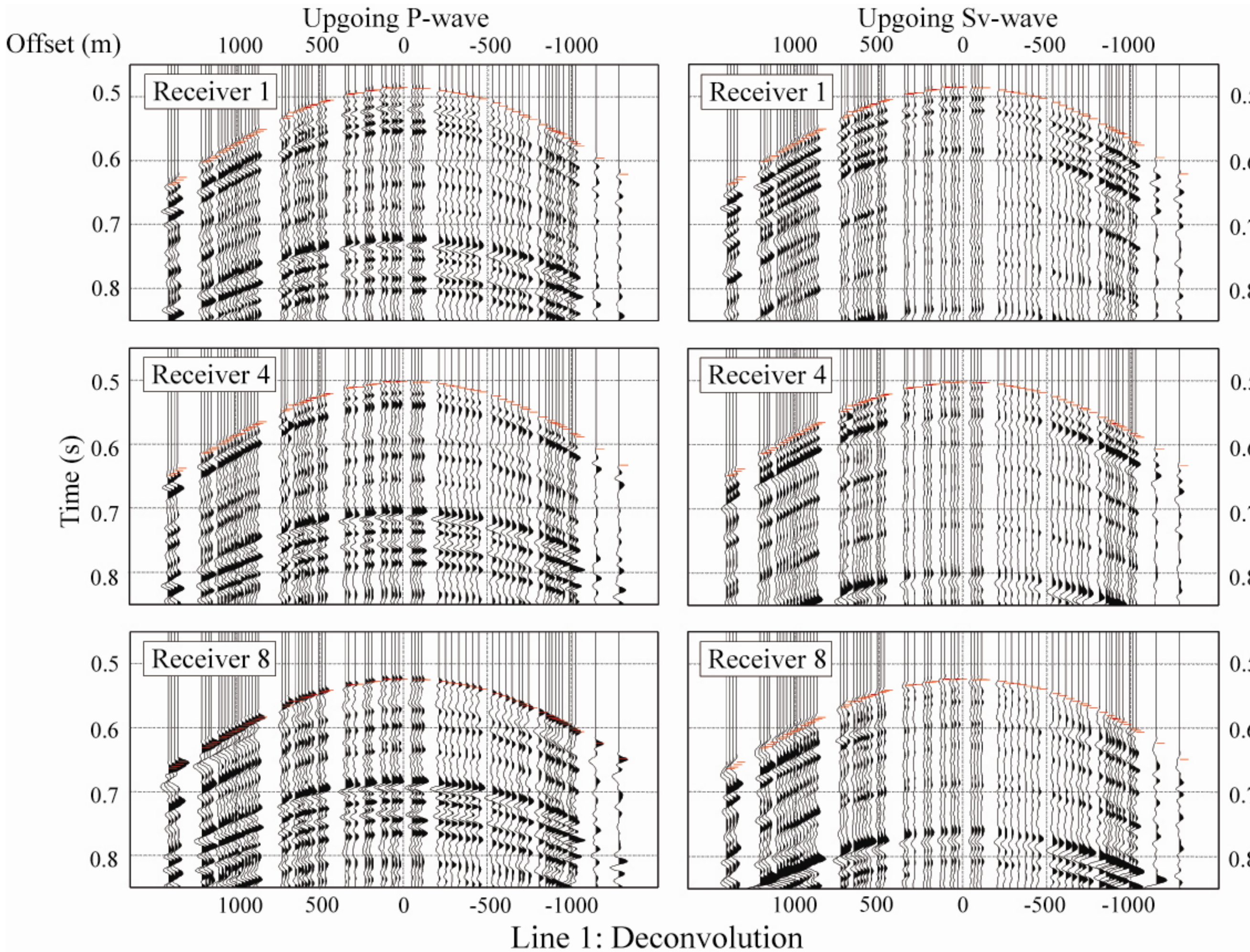

Figure 4.22: The deconvolved upgoing P- and Sv-wavefields from Line 1. Wavefields have been muted before the first arrival picks and normalized with the deconvolved downgoing P-wavefield.

4.8 Migration

Migration is used to move reflection events to their true subsurface positions and to collapse diffractions (Yilmaz, 2001). The upgoing P- and Sv-wavefields from each line were migrated with the anisotropic velocity model and a 1D VTI Kirchhoff migration algorithm. The Kirchhoff migration algorithm allows the user to define a central dip and dip aperture. The central dip is defined as the average dip of structures in the survey area, and the dip aperture is the symmetrical fan around the central dip. The formations in the Penn West site are flat-laying, so a central dip of 0^{o} and a dip aperture of 5^{o} were used for the migrations. In order to increase the frequency bandwidth of the migrated P- and Sv-wave images, the derivatives of the data were calculated and a -90^{o} phase rotation was applied to restore the original phase of the data.

Figure 4.23 shows the tie between the P-wave surface seismic and VSP data for Line 3. The VSP images show excellent ties to the surface seismic data as well as increased vertical and lateral resolution. The migrated VSP data images the Cardium Formation clearly for a radius of about 60 m around the observation well. Figure 4.24 is a comparison of the amplitude spectra from the surface seismic and VSP data. The surface seismic amplitude spectrum in Figure 4.24a appears to have been whitened up to 110 Hz.

Figure 4.25 is an L-plot of the surface seismic and VSP data. It includes the corridor stack from the zero-offset shot on Line 3 and synthetic seismogram generated from the well logs acquired in the Penn West well 1-11-48-9W5. The surface location of 1-11 is about 600 m southeast of the monitor well and is the deep well closest to the pilot site. It is a deviated well with a total depth of about 2188 m. The corridor stack ties the P-wave surface seismic data and migrated VSP image very well; however, there appears to be a small mis-tie between the synthetic seismogram and the seismic data.

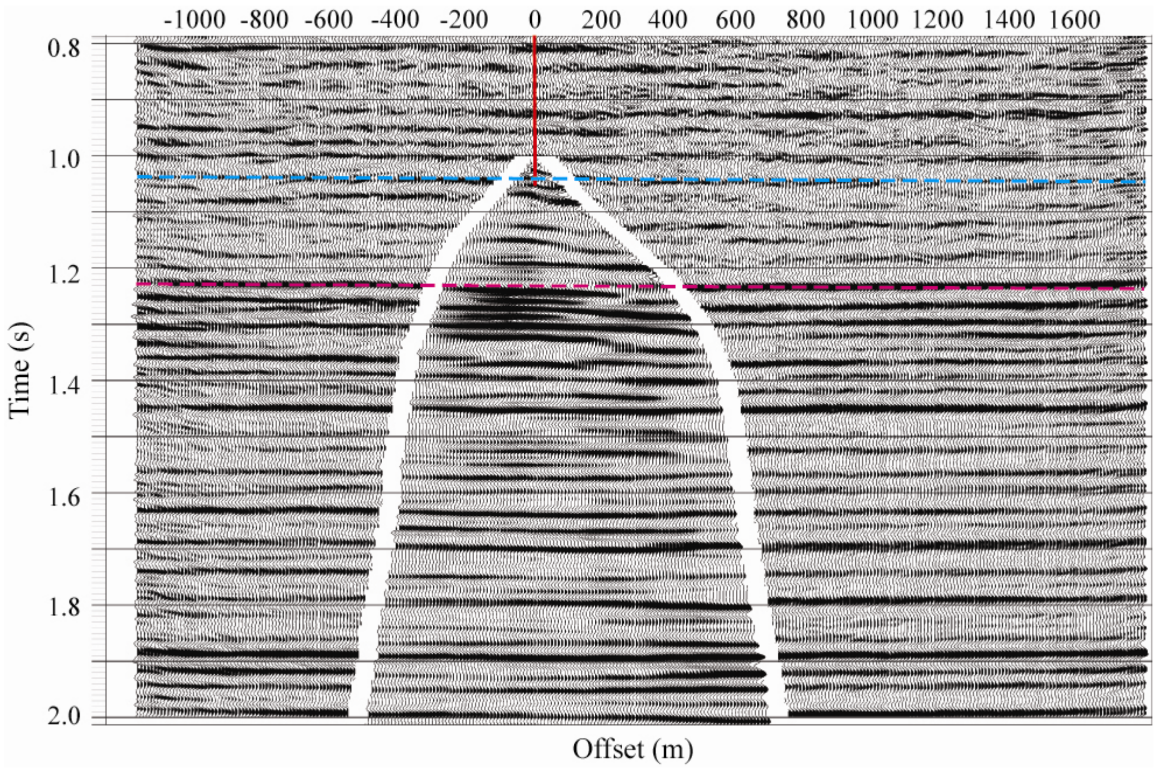

Figure 4.23: Tie between the migrated P-wave VSP data and the P-wave surface seismic data from Line 3. The Cardium Formation pick is in blue, and the Viking Formation pick is in red.

The migrated Sv-wave data were converted directly to P-wave time so that the section could be compared to the P-wave VSP and surface seismic images. In Figure 4.26, the Sv-wave events can be clearly tied to events on the P-wave surface seismic data. Some of the events on the Sv-wave image show more detail and higher resolution than the migrated P-wave VSP such as the event at 1.45 s.

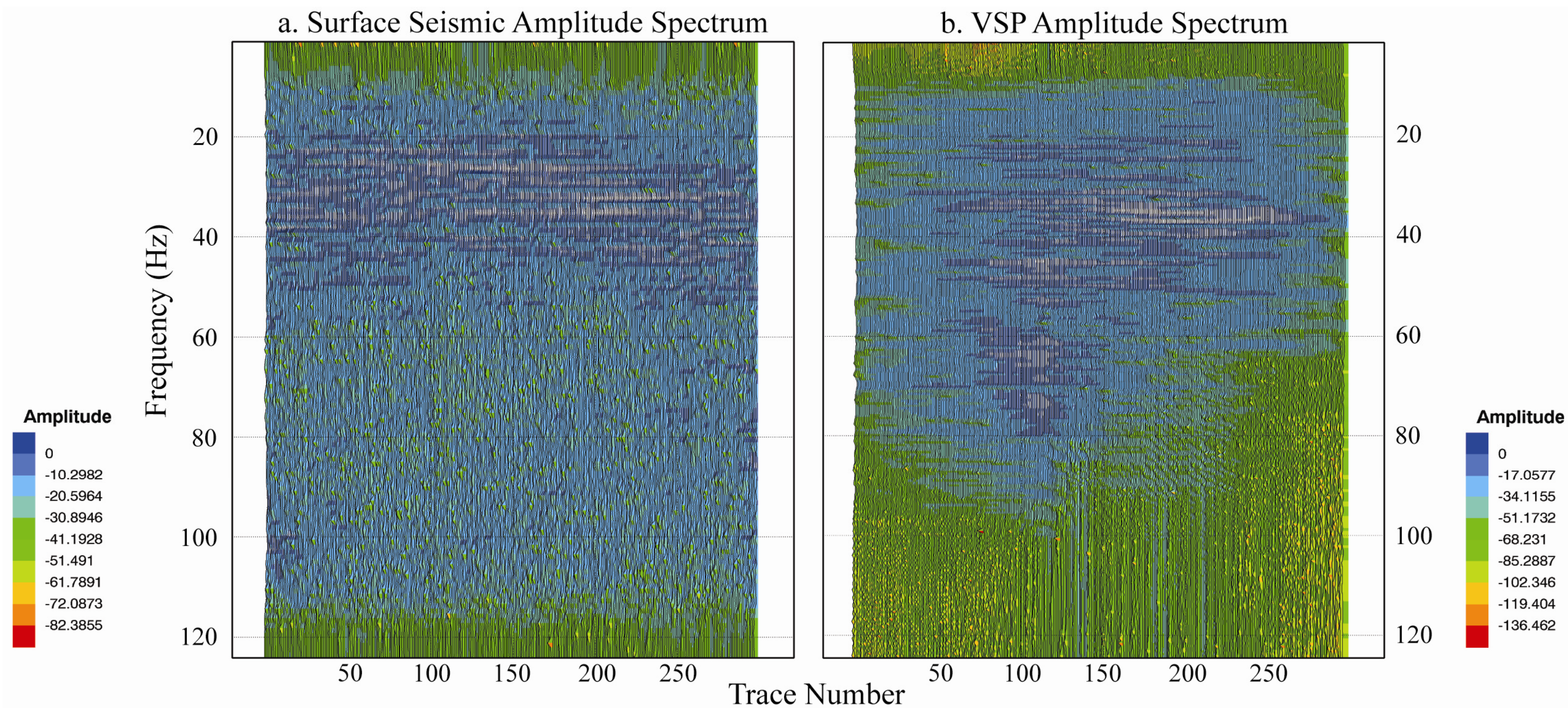

Figure 4.24: Amplitude spectra from Line 3 for the (a.) surface seismic data and (b.) the migrated VSP data.

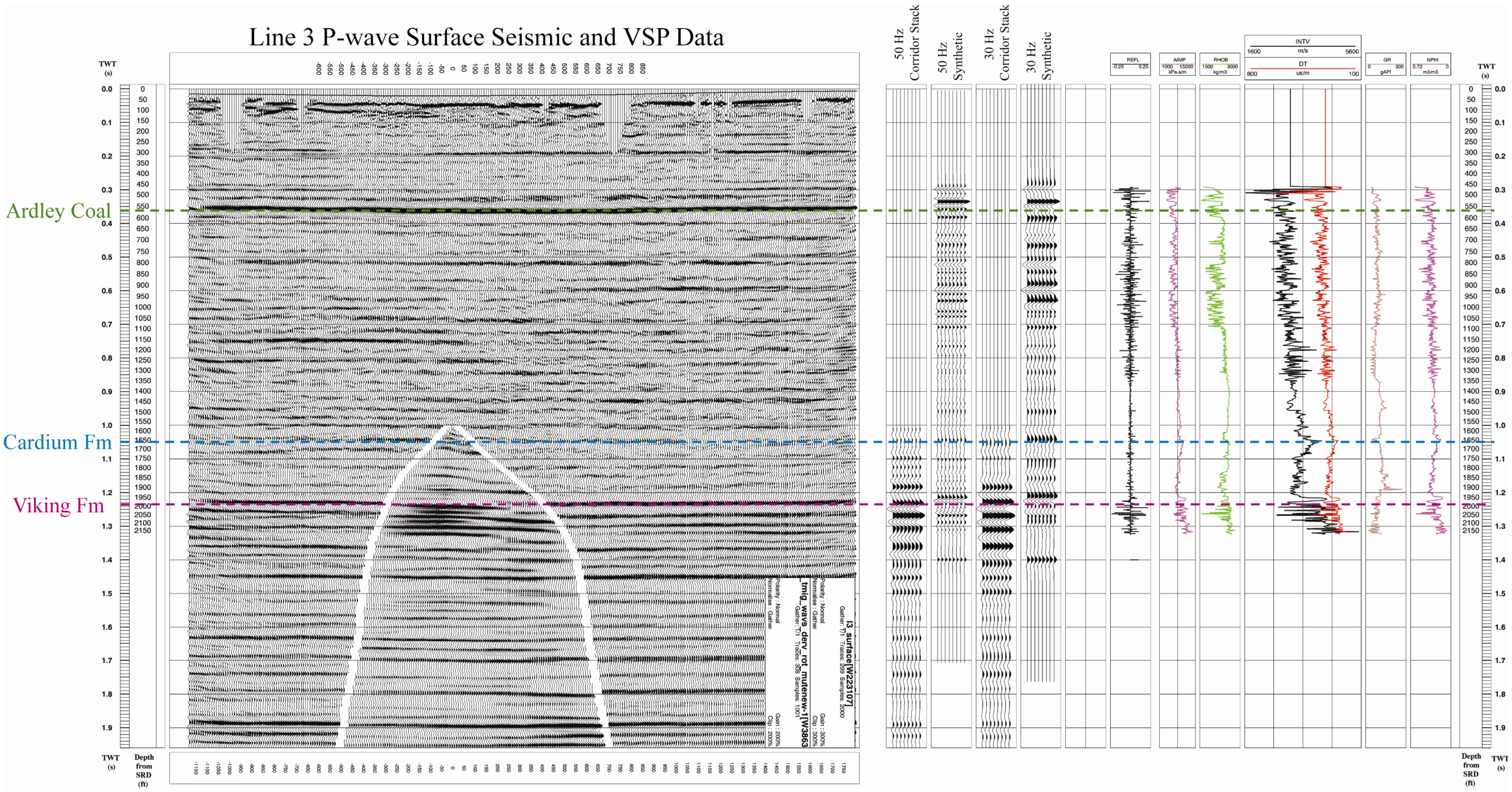

Figure 4.25: L-plot for the Line 3 surface seismic and VSP data.

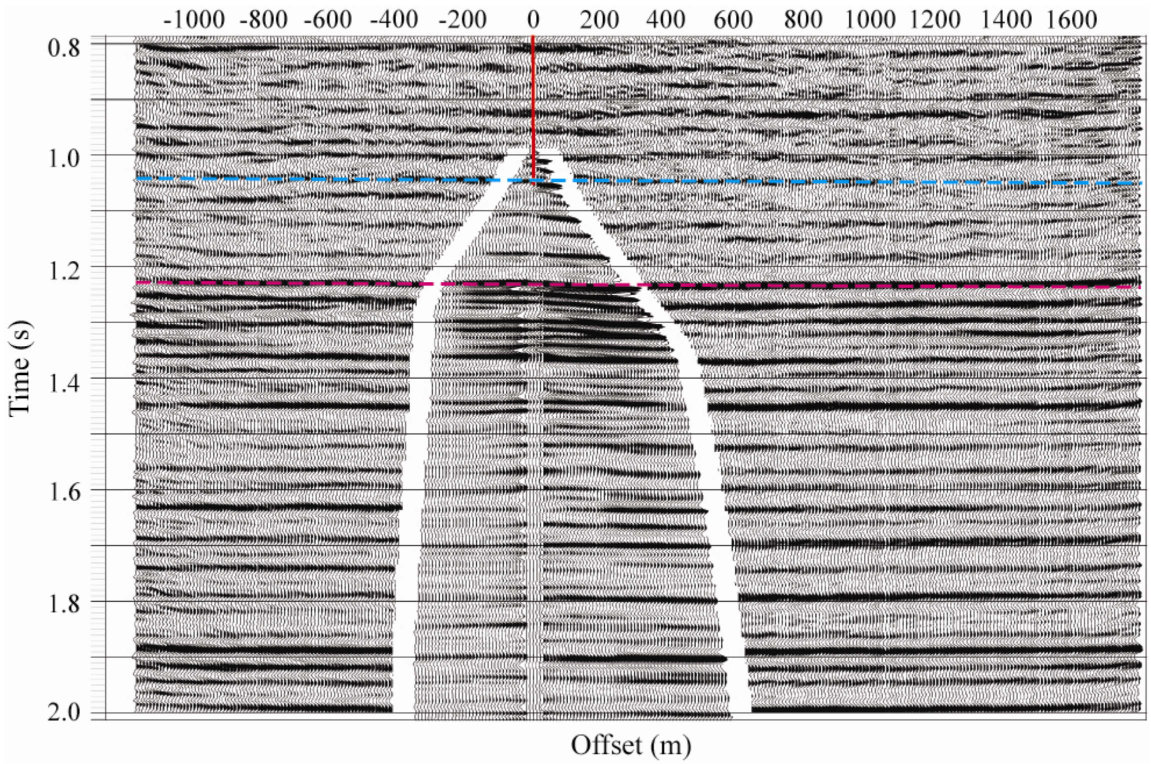

Figure 4.26: Tie between the migrated Sv-wave VSP data and the P-wave surface seismic data from Line 3. The Cardium Formation pick is in blue, and the Viking Formation pick is in red.

The converted shear-wave surface seismic data was converted to depth, and then converted to P-wave time using the anisotropic velocity model so that it could be compared to the Sv-wave VSP image (Figure 4.27). The tie here is much less obvious due to the poorer quality of the converted-wave surface seismic data. The original velocity model used by Veritas DGC for the surface seismic processing was not available to convert the S-wave surface seismic data to P-wave time. This means that the time tie with the Sv-wave VSP data is not absolute and may also be the reason for the poor ties between the two datasets. The clear ties between the Sv-wave VSP image and the P-wave images coupled with the well-constrained velocity model indicate that a high level of confidence can be placed on the Sv-wave VSP images.

Comparisons between the P- and Sv-wave migrated images for Lines 3, 2, and 1 can be seen in Figures 4.28, 4.29, and 4.30 respectively. The tie between the P- and Sv-wave images is excellent for the Cardium event and the reflections immediately beneath the Cardium event (Figures 4.28b, 4.29b, and 4.30b). However, the mis-tie between the 2 datasets increases with depth. A V_p/V_s ratio of 1.8 was used beneath the receiver array; this ratio was probably too high based on the mis-ties seen in Figures 4.28a, 4.29a, and 4.30a. Figure 4.31 shows the ties between Lines 3, 2, and 1 for the P- and Sv-wave migrated images. The migrated images from all of the lines tie each other very well.

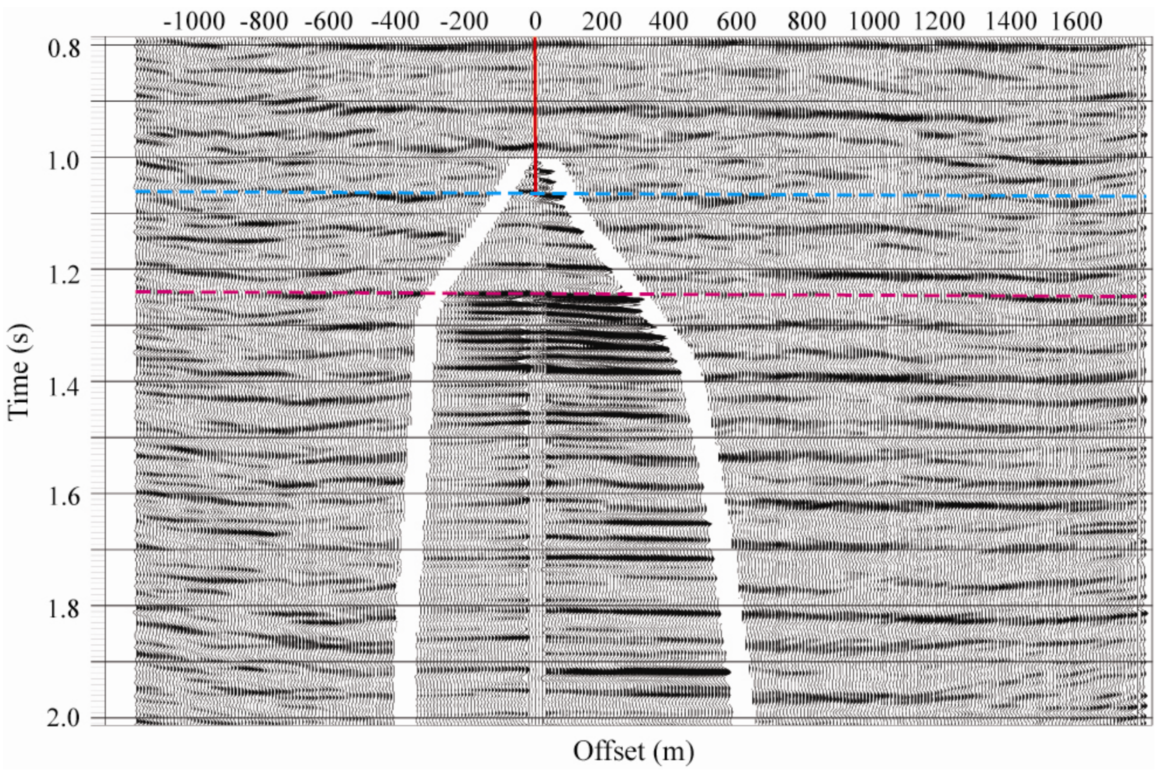

Figure 4.27: Tie between the migrated Sv-wave VSP and the converted shear wave surface seismic data from Line 3. The Cardium Formation pick is in blue, and the Viking Formation pick is in red.

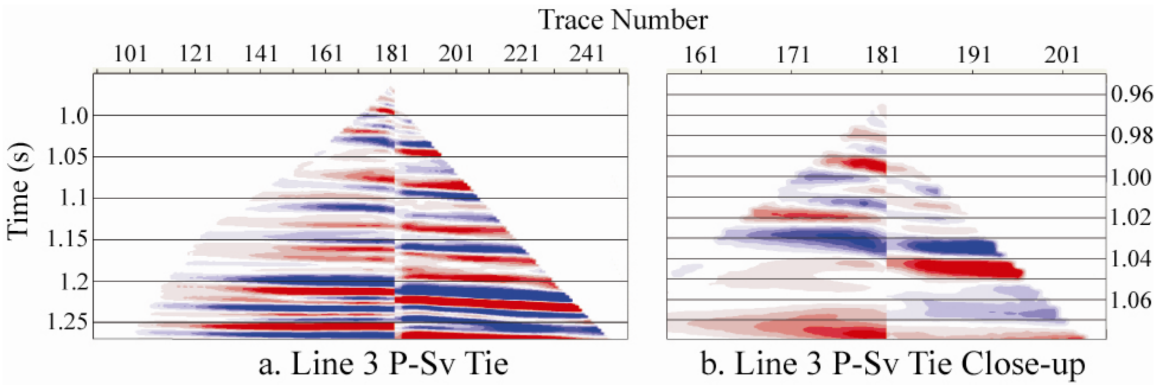

Figure 4.28: Overlay of the P-wave (left) and the Sv-wave (right) migrated images for Line 3. (a.) Large time window and (b.) a close-up of the Cardium event.

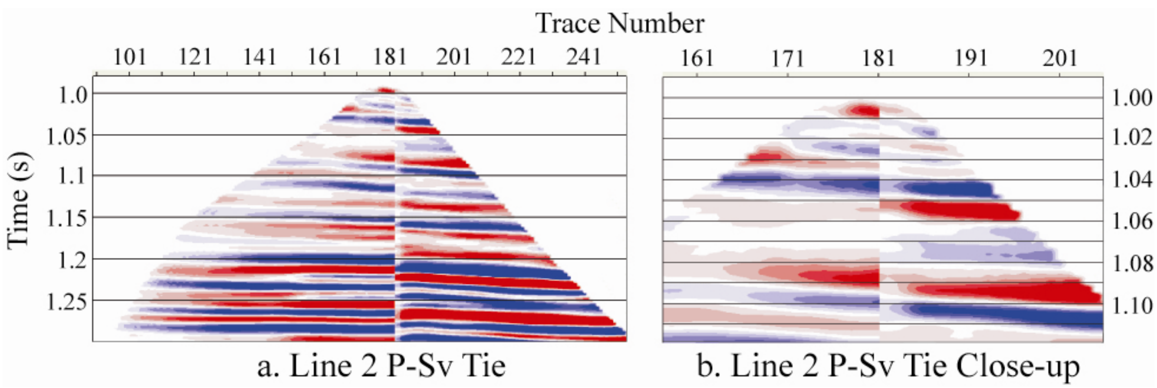

Figure 4.29: Overlay of the P-wave (left) and the Sv-wave (right) migrated images for Line 2. (a.) Large time window and (b.) a close-up of the Cardium event.

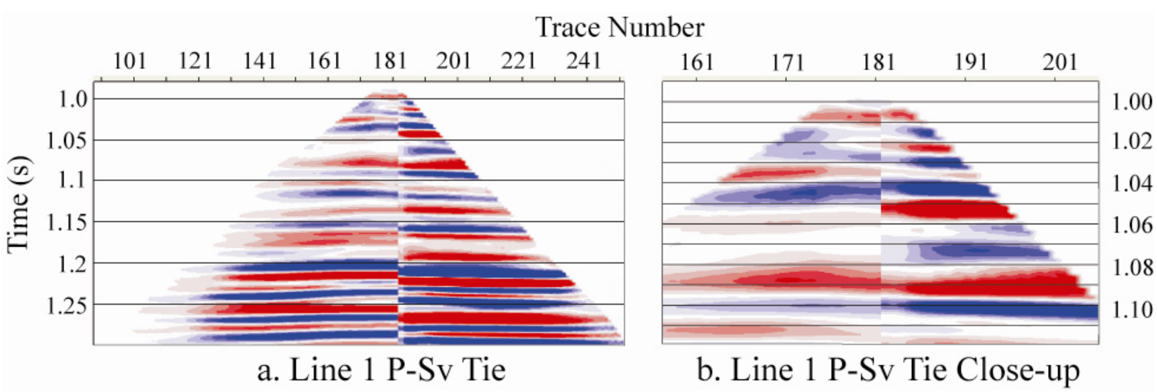

Figure 4.30: Overlay of the P-wave (left) and the Sv-wave (right) migrated images for Line 1. (a.) Large time window and (b.) a close-up of the Cardium event.

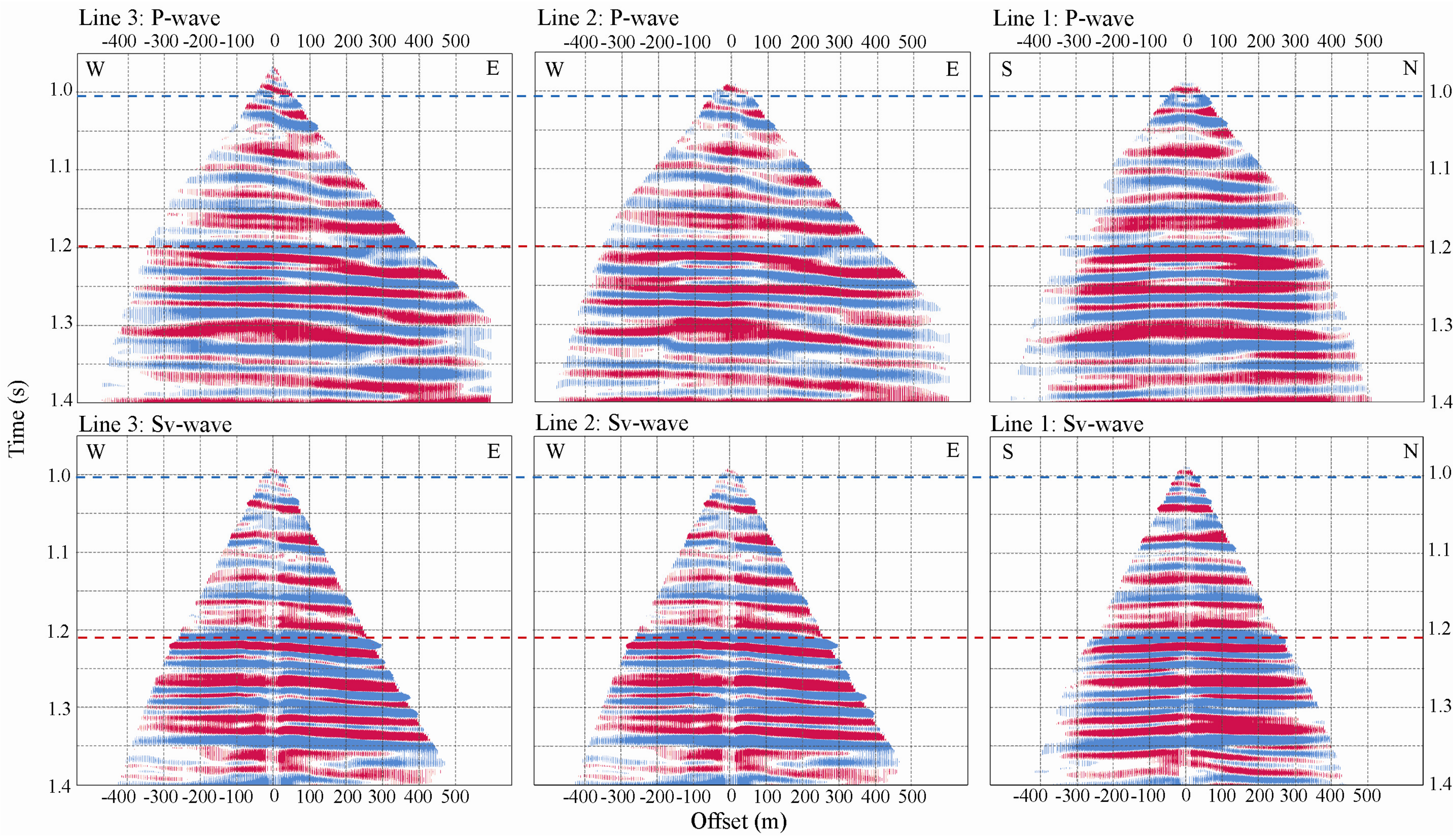

Figure 4.31: Ties between the P-wave and Sv-wave time migrated images from Lines 3, 2, and 1. The top of the Cardium Formation is in blue, and the Viking is in red.

Chapter Five: Time-lapse Processing and Results

5.1 Introduction

Chapter 5 presents the results from the time-lapse VSP surveys. A number of challenges were encountered with the time-lapse processing that would not normally be encountered with standard VSP datasets. There was a bulk static time shift between the two surveys that had to be resolved prior to wavefield separation. Non-repeated shots between the surveys also had to be removed prior to migration because repetition of source-receiver geometries is vital to the success of time-lapse analysis. Non-repeated shots that were not removed from the data were found to have an obvious effect that obscure true time-lapse change in the final difference displays. The results of the finite difference modelling using the source geometries from the baseline and monitor surveys on Line 2 support the results obtained from the survey data.

The time-lapse analysis involved comparisons of the baseline and monitor seismic data, the amplitude and phase spectra of the data, repeatability metrics, crosscorrelations in fixed windows, and creation of difference displays to identify and validate changes in the reservoir caused by the injected CO_2. In particular, the difference displays were used to detect increases in amplitude of the Cardium Formation reflection and crosscorrelations were used to identify time shifts at the base of the reservoir event.

5.2 Time-lapse Processing Issues

5.2.1 Static Shifts Between Surveys

A bulk time shift of 3 ms was observed between the baseline and monitor survey (Figure 5.1); a similar bulk shift was also identified in the surface seismic surveys. The bulk shift could not be caused by CO_2 in the reservoir because it extends to the surface, and the time shifts related to CO_2 injection should only occur at or below the depth of injection. The bulk time shift may have been caused by a number of factors such as differences in the near surface conditions or differences in the parameterization of the acquisition systems between the two surveys. For instance, the baseline survey was acquired in March 2005 at the end of the winter season when the ground was frozen hard. The second survey was acquired in December 2005 before there had been extended periods of cold weather, so the near-surface layers were probably not as deeply frozen.

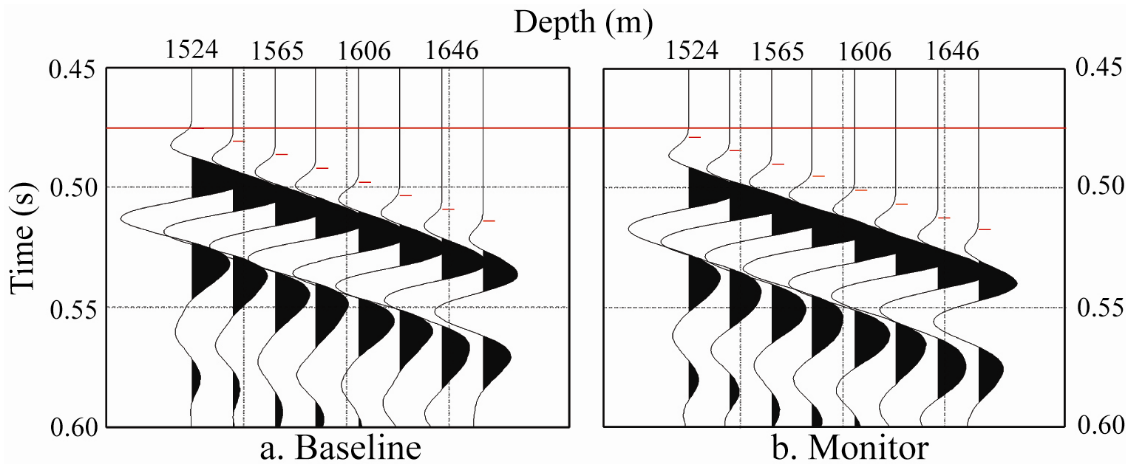

Figure 5.1: Comparison of the vertical components from a common shot gather at on Line 3 from the (a.) baseline survey and (b.) the monitor survey. The red line represents the first direct arrival time on the baseline survey. The monitor survey direct arrivals are about 3 ms later than the baseline arrivals.

The 3 ms time shift had to be removed from the monitor survey prior to the wavefield separation because the velocity model was based on the direct arrival times from the baseline survey. The bulk shift was removed by calculating the traveltime difference between the baseline and monitor survey at each shot for receiver 1 and removing that difference from all of the monitor survey traveltimes. Receiver 1 is located above the reservoir, so the direct arrival times will not be affected by the injected CO_2.

5.2.2 Effects of Non-repeated Shots

Section 3.2.1 discusses the importance of shot repeatability to time-lapse surveys. A total of eight shots, six on Line 2 and two on Line 1, were not repeated between the surveys. Originally, it was thought that all of the data should be used and that the migration would normalize the amplitudes of the non-repeated shots (Figure 5.2a and b). However, once the difference display was produced for Line 2, it was obvious that the non-repeated shots were producing differences that were overwhelming the more subtle changes in the data (Figure 5.2c). When the non-repeated shots were removed prior to migration, the differences caused by the migrated non-repeated shots disappeared (Figure 5.2d).

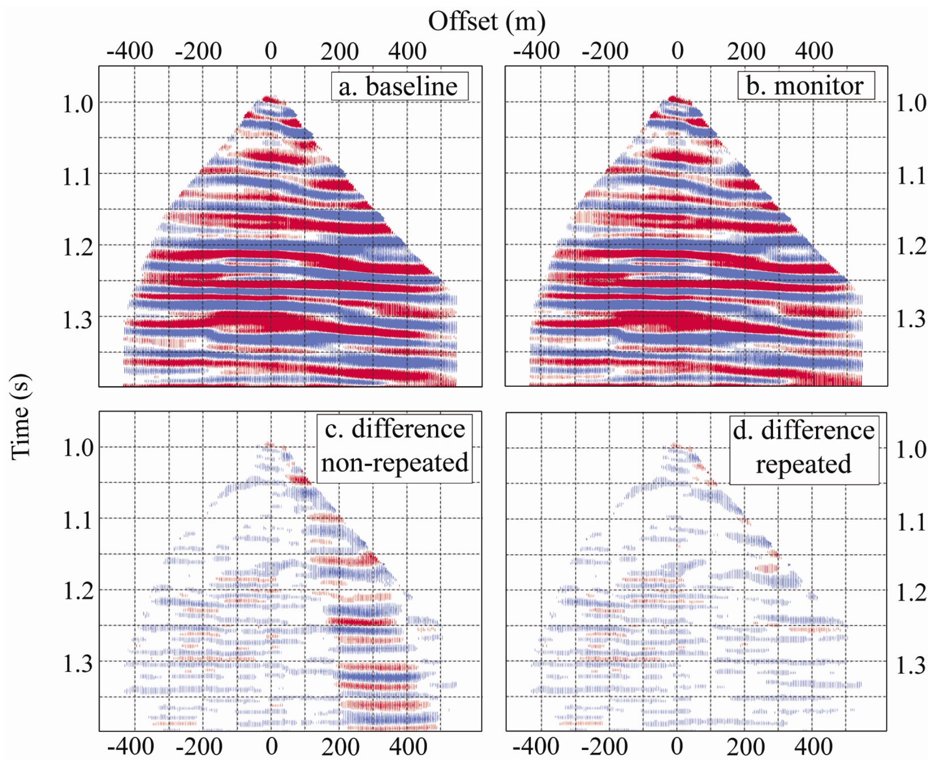

Figure 5.2: Time migrations from (a.) the baseline survey and (b.) the monitor survey. The difference display with (c.) non-repeated shots and (d.) repeated shots only. All displays use the same scaling.

To confirm the effects of non-repeated shots on the data, two finite difference models were created using the anisotropic velocity model and the baseline and monitor survey source geometries from Line 2. Initially, the two migrated synthetic datasets in Figure 5.3a and b appear to be very similar. However, the effect of the six non-repeated shots is obvious in the difference display (Figure 5.3c). These differences could potentially obscure true time-lapse changes in the data.

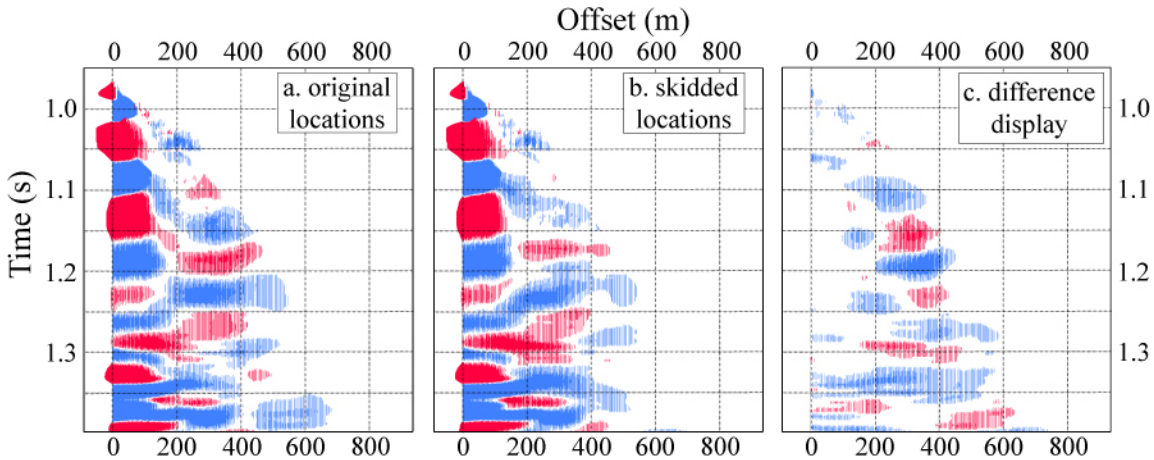

Figure 5.3: Results from the finite difference repeatability modeling. (a.) baseline survey geometry. (b.) monitor survey geometry. (c.) difference display.

In the final processing flow, all of the source locations that varied by more than 50 cm, or traces that were noisy, were removed from the datasets so that they would not affect the time-lapse analysis.

5.3 Time-lapse Results

Several tools can also be used to evaluate the quality of the time-lapse data such as comparisons of the seismic data from the two surveys at various points in the processing flow, comparisons of the amplitude and phase spectra of the surveys, and repeatability metrics. Changes in reservoir amplitudes and time shifts are both indicators of 4D changes within a reservoir (Sections 3.3.3 and 3.3.4).

5.3.1 Similarity of the Data

Figures 5.4 to 5.6 show the comparisons between the rotated datasets from the baseline and monitor surveys for Lines 3, 2, and 1. Figures 5.7 to 5.9 are comparisons of the baseline and monitor survey data after deconvolution. The data in all of the figures show a remarkable apparent degree of similarity considering the surveys were acquired eight months apart.

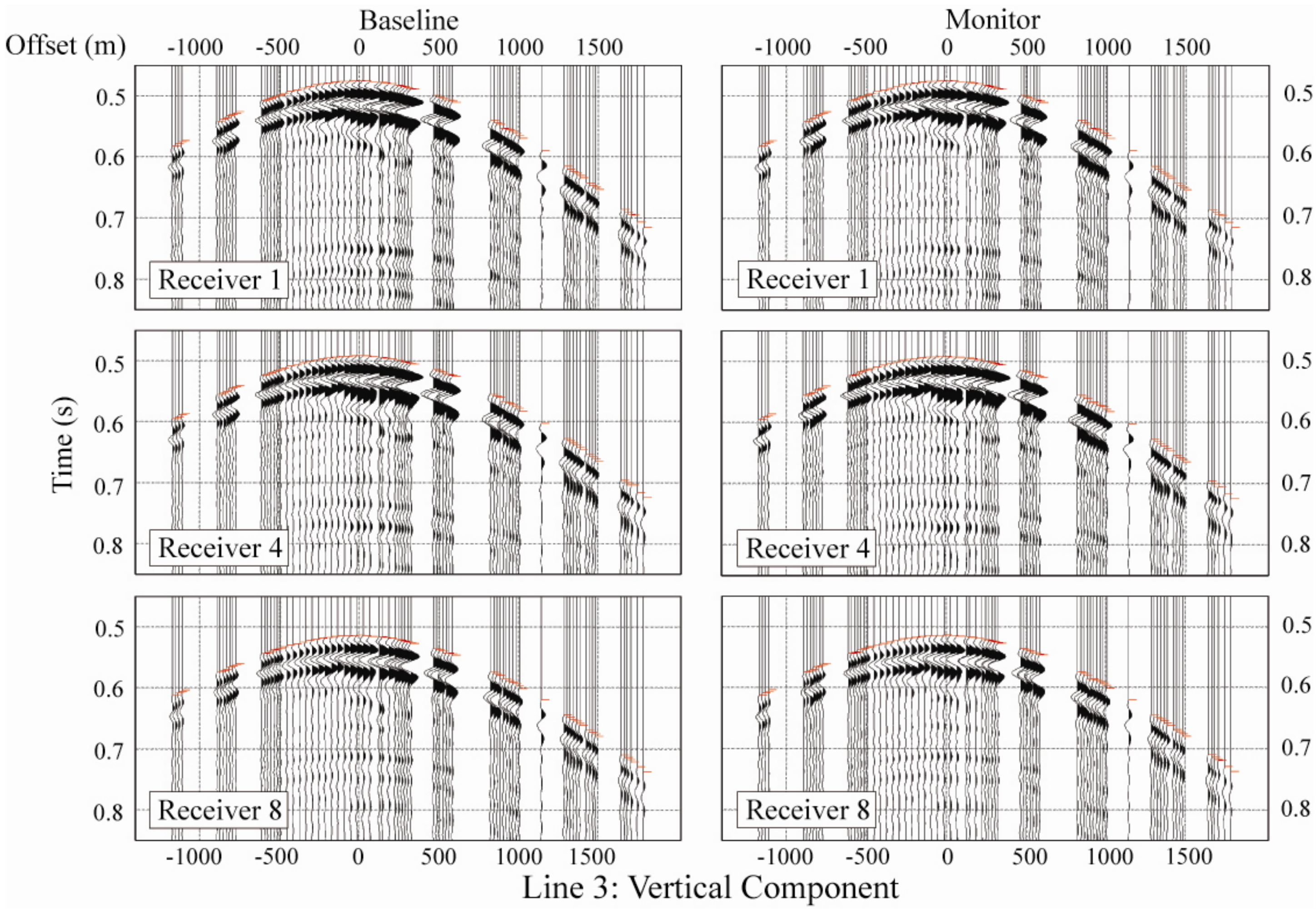

Figure 5.4: Comparison of the vertical component of the rotated data from receivers 1, 4, and 8 on Line 3. The two datasets show a remarkable degree of similarity. True amplitude display.

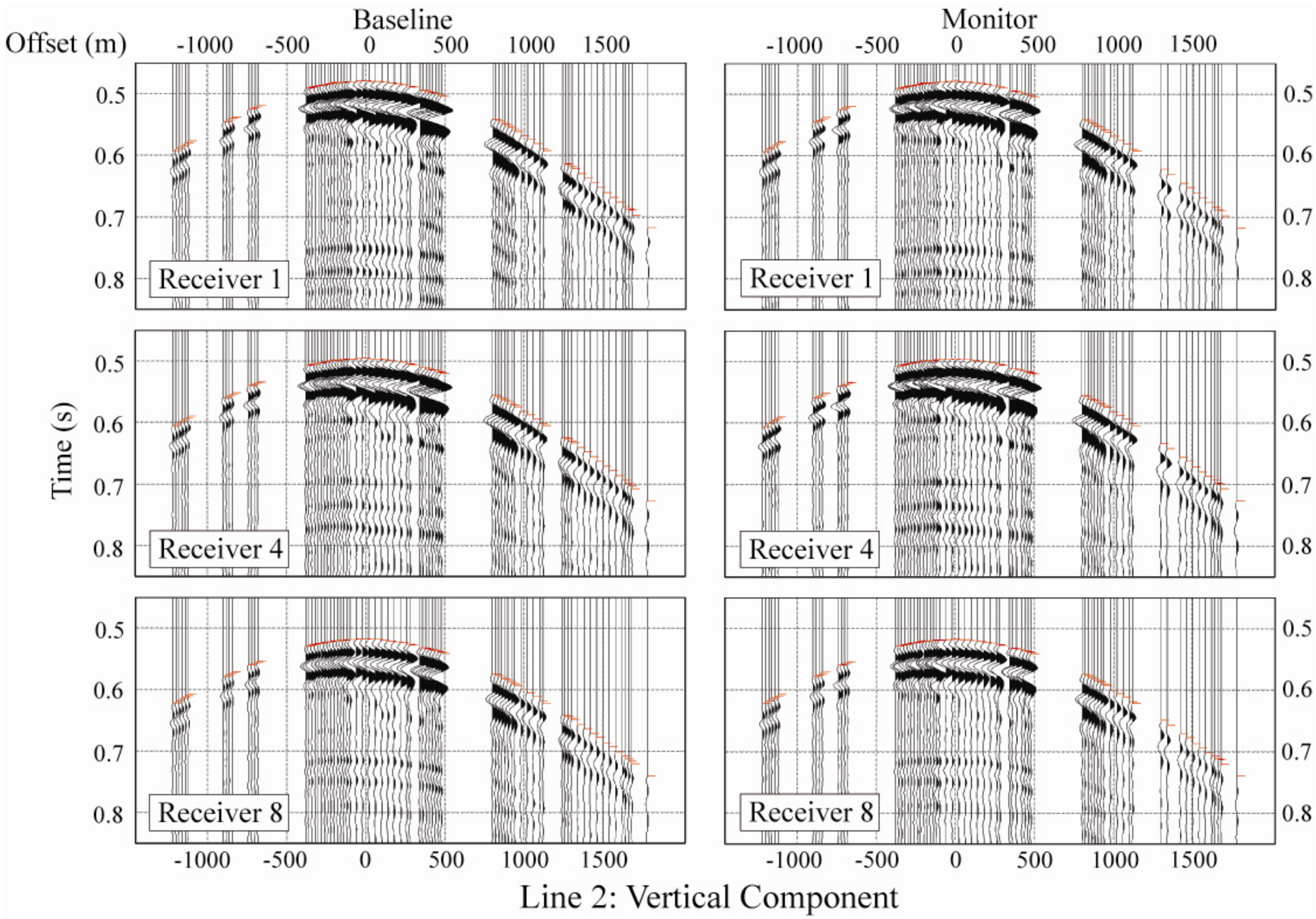

Figure 5.5: Comparison of the vertical component of the rotated data from receivers 1, 4, and 8 on Line 2. True amplitude display.

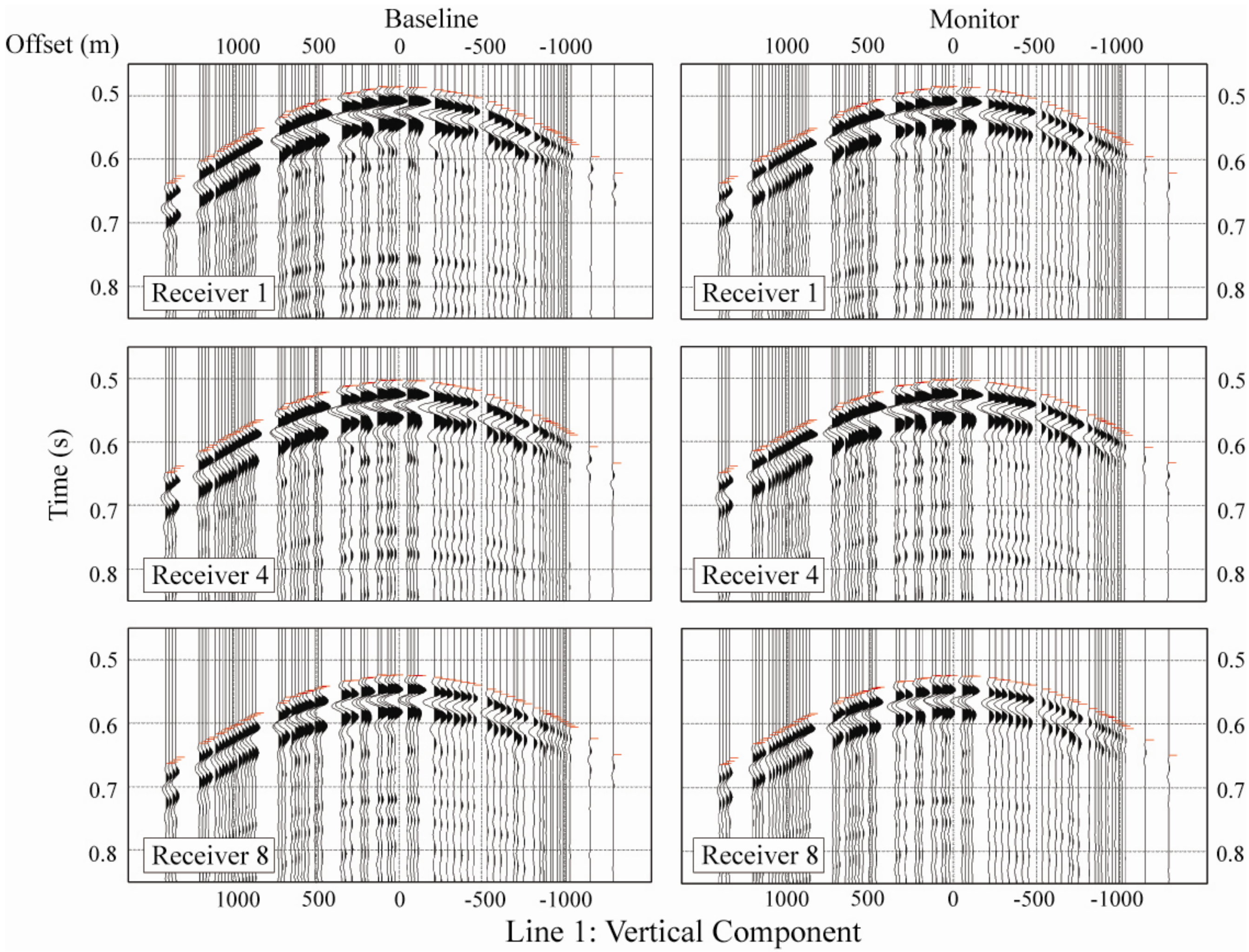

Figure 5.6: Comparison of the vertical component of the rotated data from receivers 1, 4, and 8 on Line 1. True amplitude display.

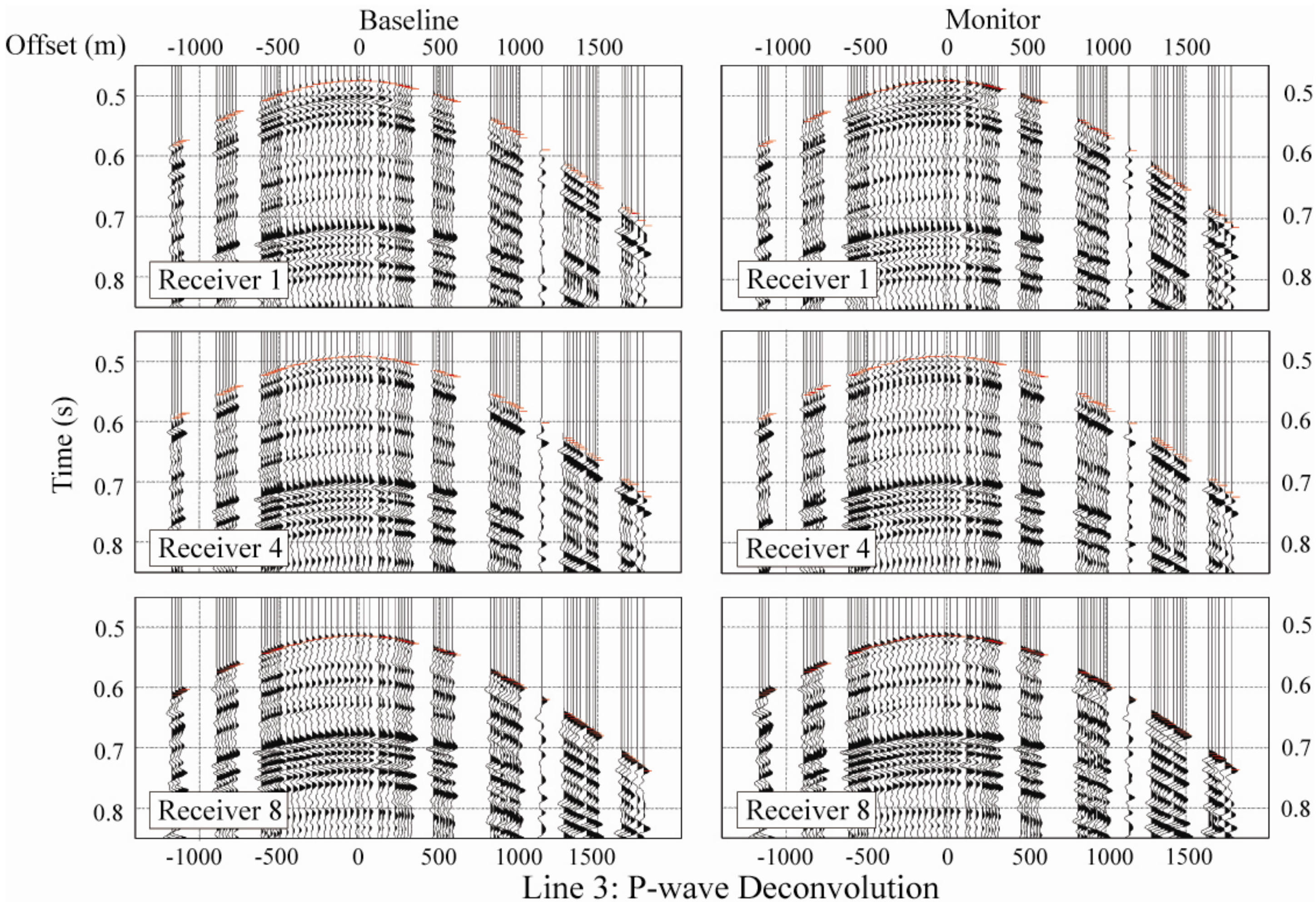

Figure 5.7: Comparison of the deconvolved upgoing P-wave data from receivers 1, 4, and 8 on Line 3. True amplitude display.

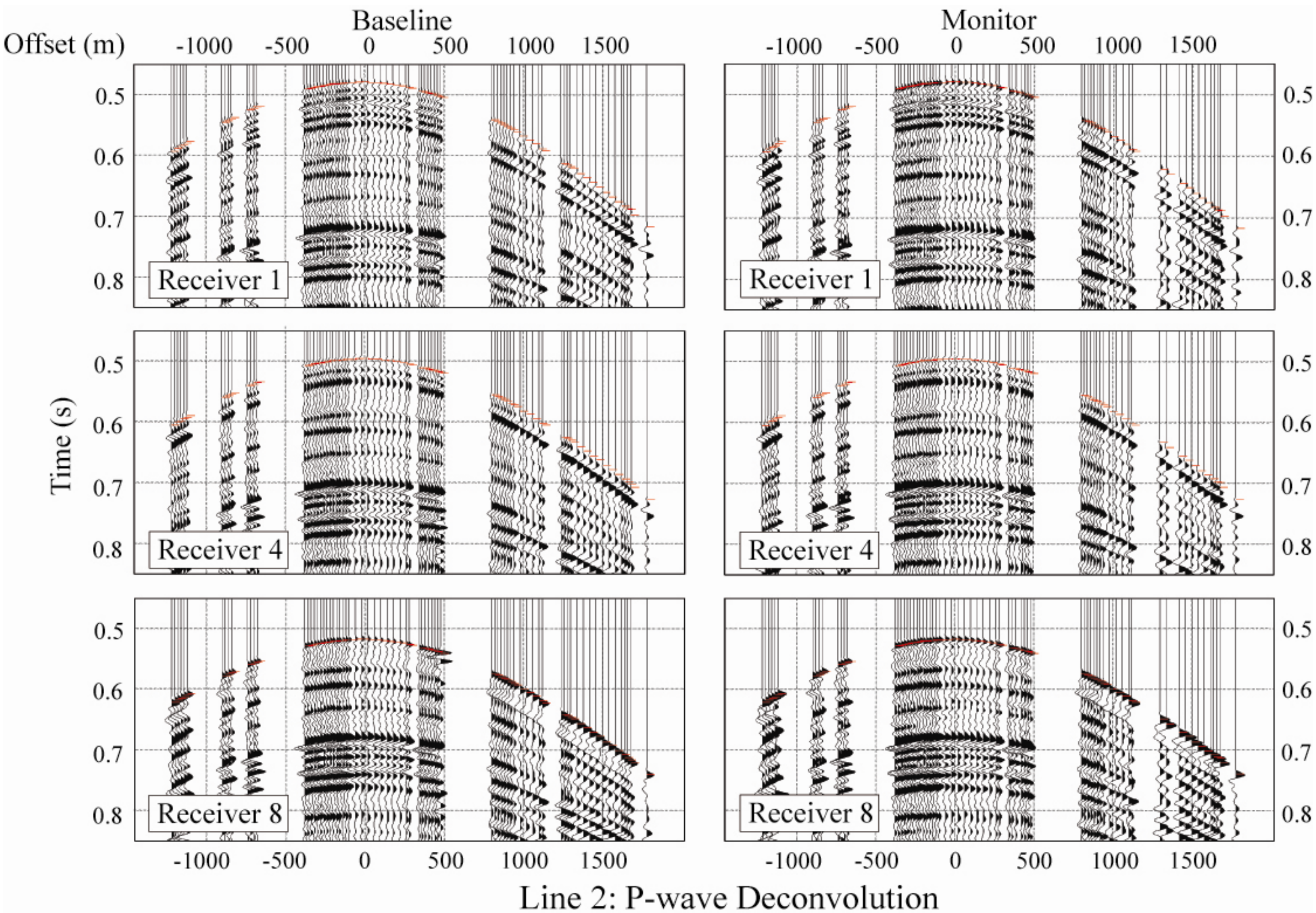

Figure 5.8: Comparison of the deconvolved upgoing P-wave data from receivers 1, 4, and 8 on Line 2. True amplitude display.

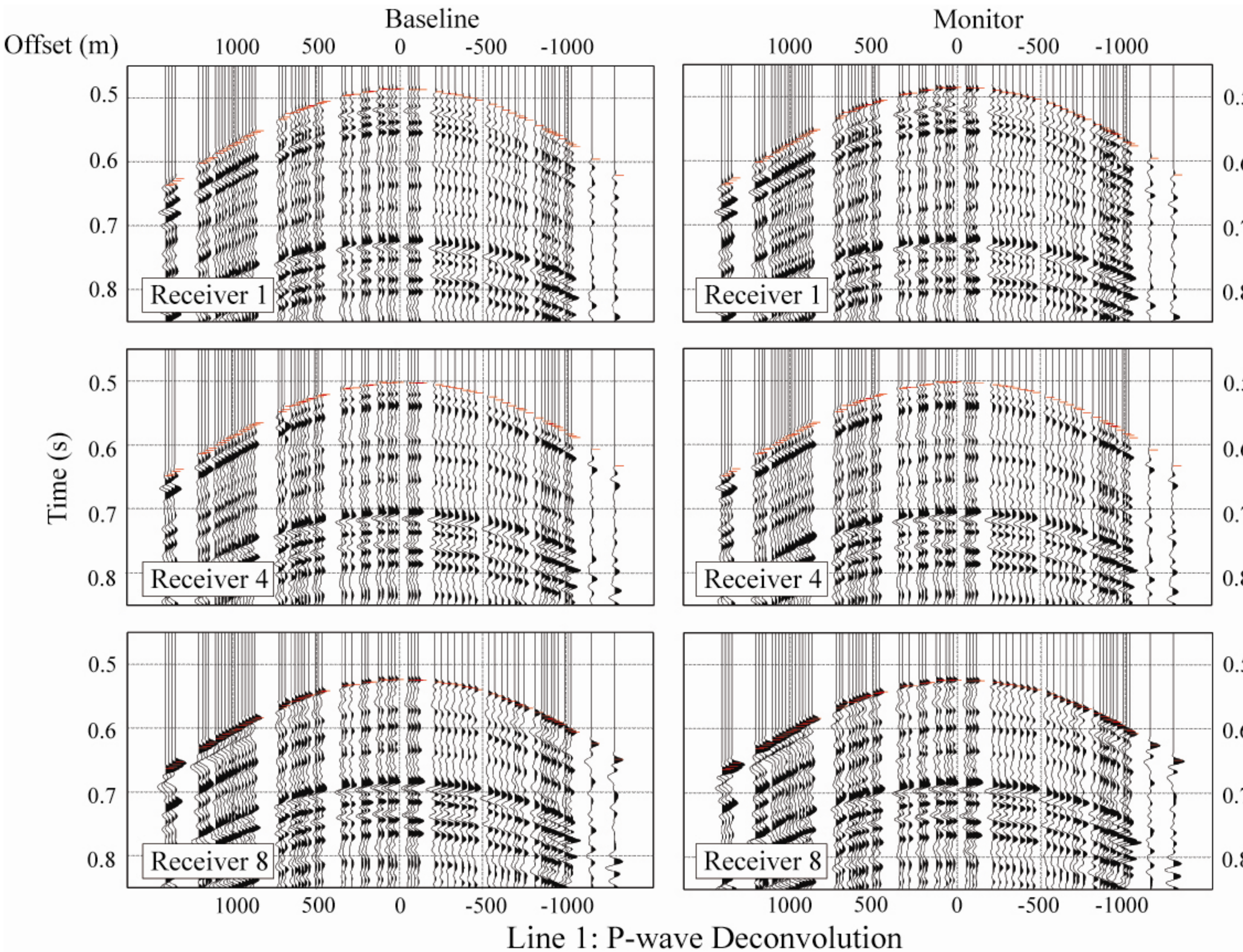

Figure 5.9: Comparison of the deconvolved upgoing P-wave data from receivers 1, 4, and 8 on Line 1. True amplitude display.

5.3.2 Amplitude and Phase Spectra

The average amplitude and phase spectra were calculated for the baseline and monitor survey data from Line 2 (Figure 5.10). The analysis window extends from 0.9 to 1.9 s and from trace 31 to 337 (Figure 5.10a). The amplitude and phase spectra were calculated for each trace in the window. Then, the spectra for all of the traces were stacked to produce the average phase and amplitude spectra (Figures 5.10b and c). Null values were rejected from the analysis.

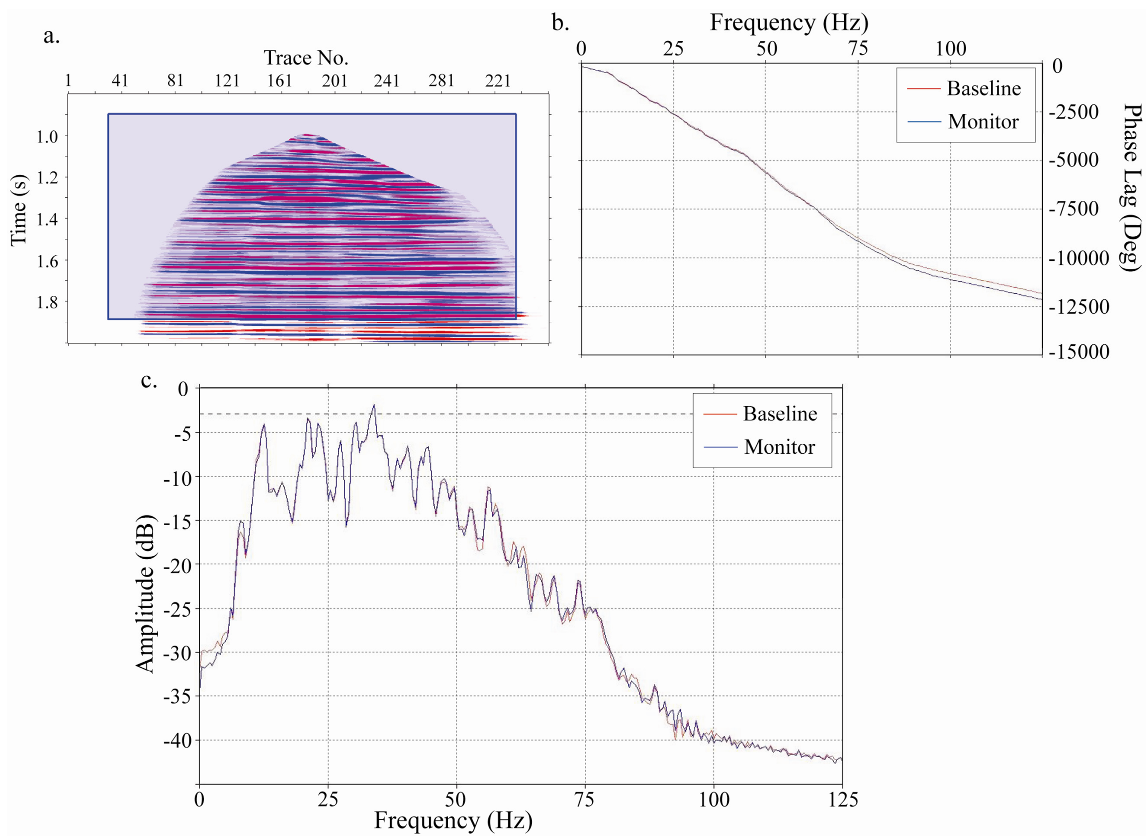

Figure 5.10: (a.) The window used to analyze the phase and amplitude spectra of the baseline and monitor surveys from Line 2. Comparison of (b.) the unwrapped stacked phase spectra and (c.) the stacked amplitude spectra of the baseline and monitor surveys.

While the overall stacked phase and amplitude spectra are very similar for the displayed frequency range, the small differences in the spectra may cause coherent events to appear beneath the Cardium event in the difference displays. Cross-equalizing the data should match the amplitude and phase spectra of the monitor survey to the baseline survey and remove time shifts between the surveys. This should reduce the number coherent events beneath the Cardium reflection.

When dynamite is used as a seismic source for time-lapse surveys, it can contribute to the differences in the amplitude and phase spectra between surveys. Other researchers have found that repeated dynamite surveys regularly have larger frequency bandwidth than the baseline surveys (P. McGillivray, personal communication, 2006). The first dynamite shot fired at a location consolidates the surrounding ground material. This leads to improved coupling with the ground for subsequent shots fired at that location. Ultimately, this leads to higher frequency bandwidth in the data; the Penn West data may be displaying this effect as well.

5.3.3 Repeatability Metrics and Cross-equalization Results

The repeatability metrics NRMS and predictability were calculated for the P-wave migration images for all of the lines in a window that extended from 1.03 to 1.885 s (Figures 5.11 to 5.13). The window did not include the reservoir interval. The NRMS values for the data between traces 150 and 300 on Lines 2 and 1 are at or below 10%; this trace range covers the bulk of the dataset (Figure 5.11a and 5.12a). For Line 3, the NRMS values ranged up to 15% (Figure 5.13a). The NRMS values increase up to 30% at the edges of each image, but this is probably due to a lack of data at the ends of each line. The predictability for the same trace range is above 99% for all of the lines (Figures 5.11b, 5.12b, and 5.13b). The NRMS and predictability values from the surface seismic data examples in Section 3.3.1 varied between 18 to 30% and 93 to 99% respectively. Based on the NRMS and predictability values from the examples, the results obtained for all of the VSP data are excellent. However, these results also suggest that cross-equalization will have little effect on the data.

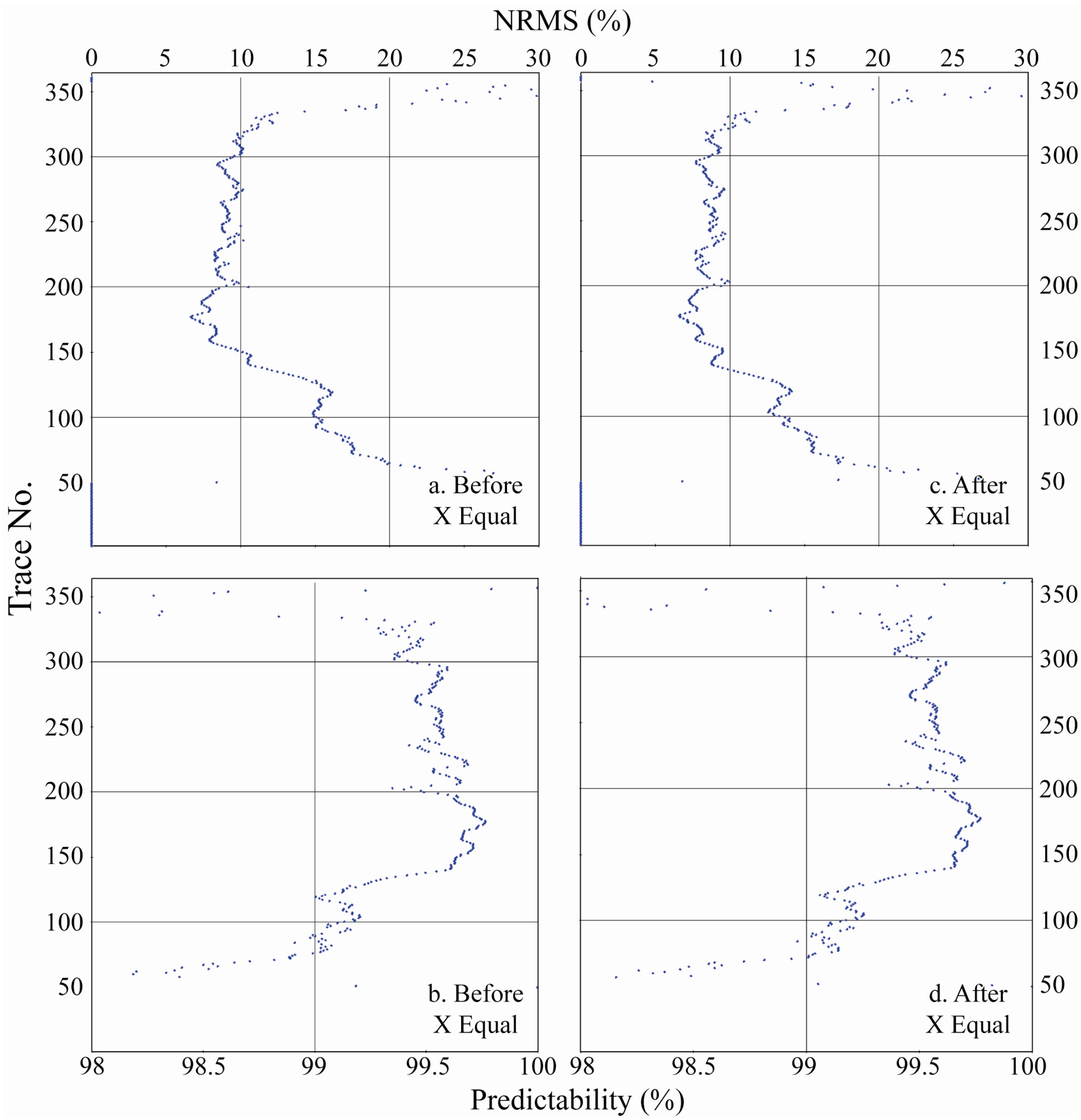

Figure 5.11: Repeatability metrics before and after cross-equalization. (a.) NRMS before cross-equalization. (b.) Predictability before cross-equalization. (c.) NRMS after cross-equalization. (d.) Predictability after cross-equalization.

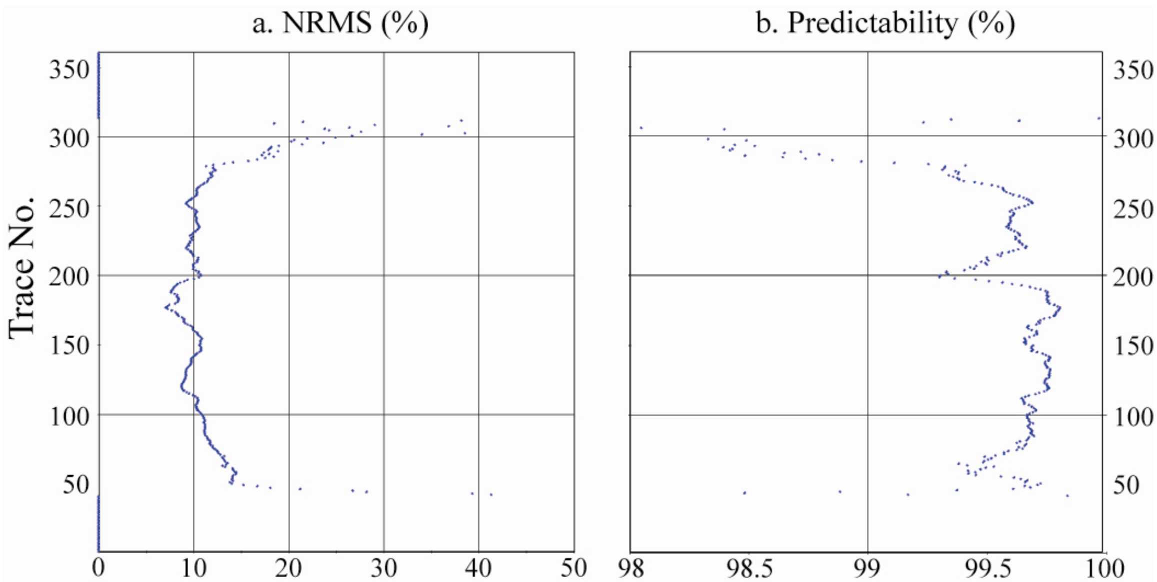

Figure 5.12: The NRMS and Predictability for Line 1.

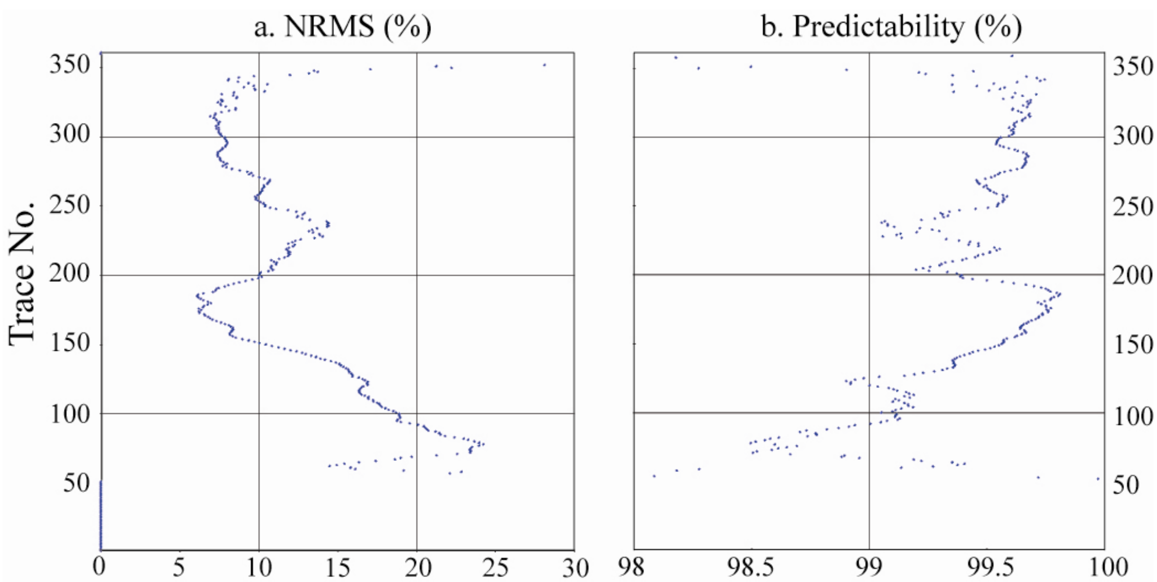

Figure 5.13: The NRMS and Predictability for Line 3.

The P-wave migrated images from Line 2 were used to test the effect of cross-equalization on the data. The cross-equalization operator was designed on a trace-by-trace basis using the predictability calculations. The operator should correct for amplitude, frequency, phase, and time shifts in the monitor survey. The repeatability metrics were recalculated after the monitor survey was cross-equalized and a new difference display was generated.

The new NRMS and predictability results show an incremental improvement between traces 100 and 150, but in general, there has not been a significant improvement in the repeatability metrics with cross-equalization (Figure 5.13c and d). Figure 5.14 is a comparison of the difference displays before and after cross-equalization. It appears that there has only been an incremental improvement in the coherent noise beneath the reservoir between traces 100 and 150 at time 1.24 s. The improvements in the cross-equalized difference display correlate to the improvements in the cross-equalized repeatability metrics (Figure 5.14b).

Arguably, the cross-equalization has been detrimental to the difference display. The software used for the cross-equalization was designed for large surface seismic datasets, and the cross-equalization operator has introduced the noise at the edges of the cross-equalized image. Cross-equalization was not used in the final processing flow.

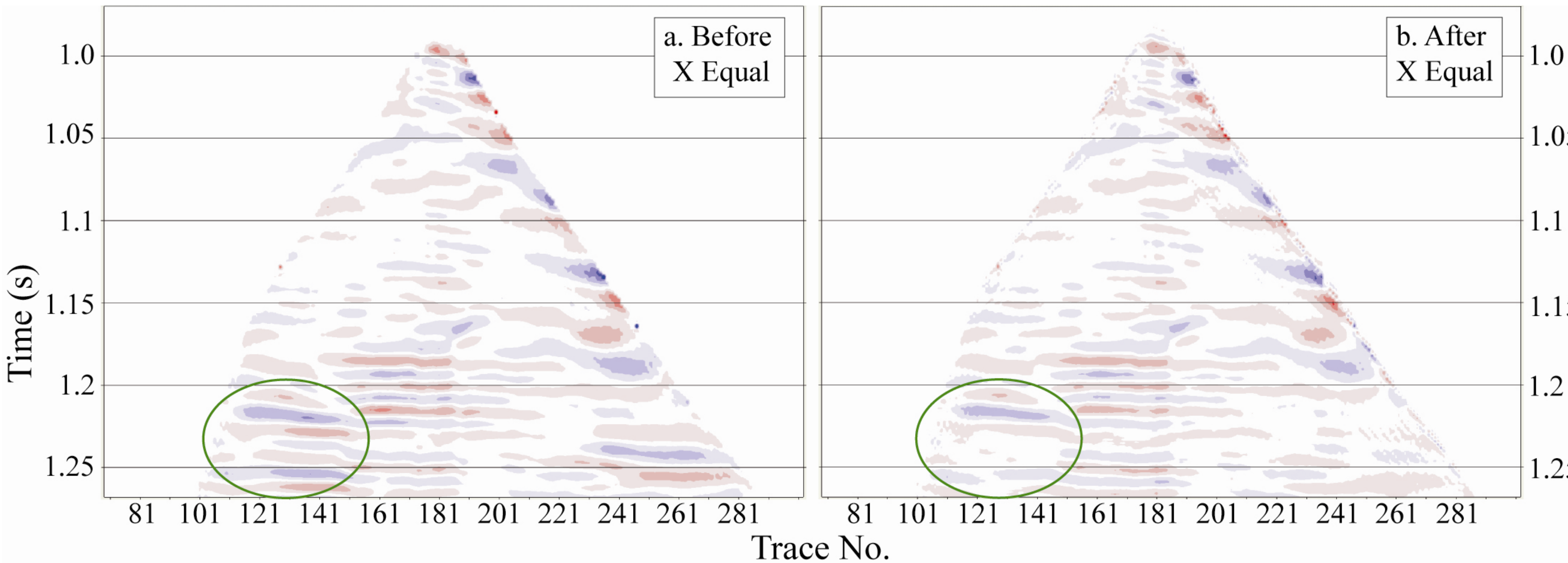

Figure 5.14: Comparison of the difference displays from Line 2 (a.) before cross-equalization and (b.) after cross-equalization. There has only been an incremental improvement in the difference displays between traces 100 and 150 at about 1.24 s.

5.3.4 Crosscorrelations

Crosscorrelations are used to identify time shifts related to particular events in the data. The time migration data was resampled to 0.25 ms prior to crosscorrelating the baseline and monitor datasets. The time migrated images from the each line and survey were crosscorrelated in three time windows: a 15 ms window around the base of the Cardium Formation reflection, a 30 ms window around the Viking Formation, and a 35 ms window around a deep event at 1.4 s. The results of the crosscorrelations for the P- and Sv-wave time migrated data have been summarized in Tables 5.1 and 5.2, respectively. The time picking algorithm used a sinc interpolator to pick times between the sample intervals.

Table 5.1: Time shifts from P-wave time migrations base on crosscorrelations between the baseline and monitor surveys.

Line No./Formation	Base Cardium Event	Viking Event	Deep Event (1.4s)
Line 1	0.2 ms decreasing to 0 at monitor well	0.3 ms decreasing to 0 at monitor well	0
Line 2	0.2 ms	0.2 ms	0
Line 3	inconsistent	inconsistent	0

Table 5.2: Time shifts from Sv-wave time migrations base on crosscorrelations between the baseline and monitor surveys.

Line No./Formation	Base Cardium Event	Viking Event	Deep Event (1.4s)
Line 1	inconsistent	0.3 ms decreasing to 0 at monitor well	0
Line 2	0.1 – 0.4 ms	0.1 - 0.2 ms	0
Line 3	0.2 ms decreasing to 0.1 ms at monitor well	0.2 ms decreasing to 0 at monitor well	0

The crosscorrelations for the P-wave time migrated data on Line 2 show a systematic increase in traveltime of 0.2 ms. The time shifts around the base of the Cardium event on Line 1 decrease from north to south approaching the monitor well. The crosscorrelations for Line 3 data do not show a consistent time shift. This may be due to the tuning effect between the top and base of the Cardium event on this line (Figure 5.15). Time shifts were not found for the event at 1.4 s on any of the lines. In general, the time shifts measured in the Sv-wave data do not show the consistent time shifts observed in the P-wave data. This may be a result of the low amplitudes at the near offsets in the Sv-wave images.

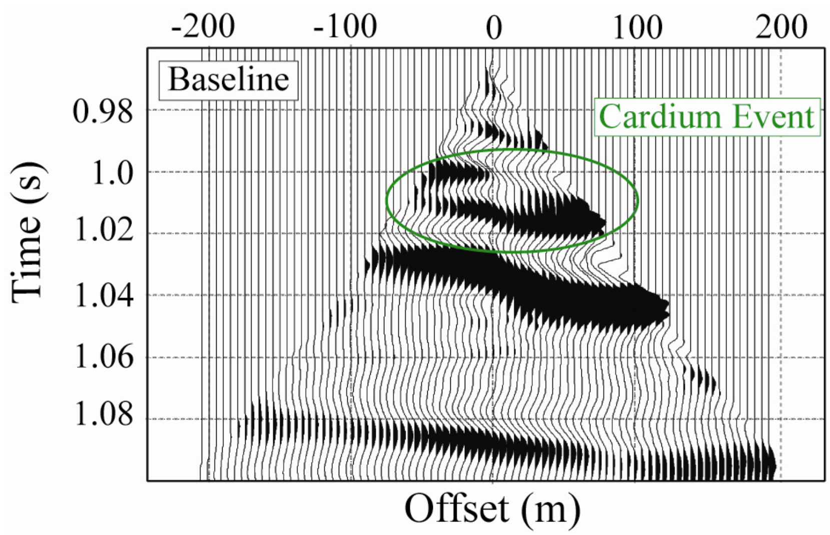

Figure 5.15: Detail of the Cardium event on the baseline time migrated image from Line 3. The tuning effect between the top and base of the Cardium formation make it difficult to measure meaningful time shifts.

5.3.5 Difference Displays

The difference displays were created by subtracting the baseline time migrated images from the monitor time migrated images. The difference displays make it easier to identify amplitude changes and time shifts in the data.

The P- and Sv-wave difference displays from Line 2 show the clearest time-lapse differences (Figure 5.16). The amplitudes associated with the Cardium event on this line have increased between the baseline and monitor surveys and correlate directly to the

Cardium event. Amplitude increases that correlate directly to seismic reflection events have not been identified below the Cardium event. On Line 1, the amplitude anomalies associated with the Cardium event are more subtle and only appear on the north end of the line (Figure 5.17). Amplitude anomalies have also been identified on the east end of the P-wave images from Line 3 (Figure 5.18).

The Sv-wave images show amplitude anomalies on all of the lines, and time shifts have been identified at the base of the Cardium event on Lines 2 and 3. However, the time-lapse changes in the Sv-wave data are less consistent than those found in the P-wave data.

Figure 5.19 displays the changes in amplitudes that have occurred on the Cardium and Viking events in the time between the baseline to the monitor surveys for the P- and Sv-wave migrated images on each line. Initially, it appears that the amplitudes on the Viking event show a similar degree of variation between the two surveys as the amplitudes on the Cardium event. However, when the percentage change in amplitude is calculated for both events, the change in amplitude on the Cardium event is more significant than the variation on the Viking event (Figure 5.20). On most of the lines, the percentage change in amplitude for the Viking event is less than 5 % while the P-wave amplitudes for the Cardium event on Line 2 have changed between 10 to 35% (Figure 5.20a).

Coherent events also appear on the difference displays below the Cardium event; however, they do not correlate directly to reflections in the baseline and monitor surveys. These events occur beneath the receiver array where the deconvolution operator is less effective. They are caused by small differences between the amplitude and phase spectra and by small time shifts on reflectors between the baseline and monitor surveys. The resulting differences in the wavelet appear as coherent events in the difference display.

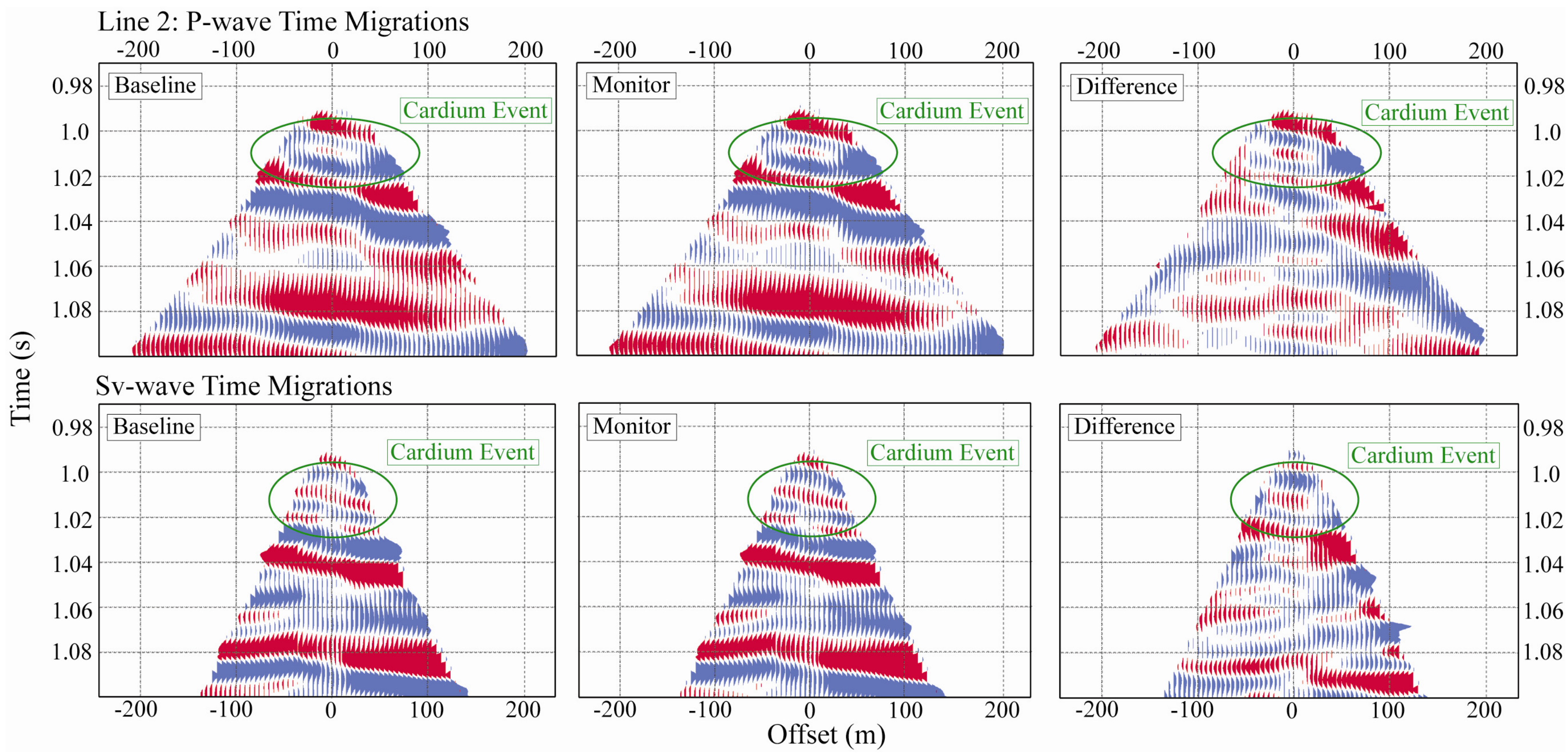

Figure 5.16: Baseline and monitor survey time migrated images and difference displays for the P- and Sv-wave data from Line 2. Amplitudes at the Cardium event have increased up to 35% on some traces. The difference display amplitudes are scaled up three times from the baseline and monitor displays. Events beneath the Cardium event are caused by small differences in the amplitude and phase spectra and small time shifts between the two surveys rather than the injected CO_2.

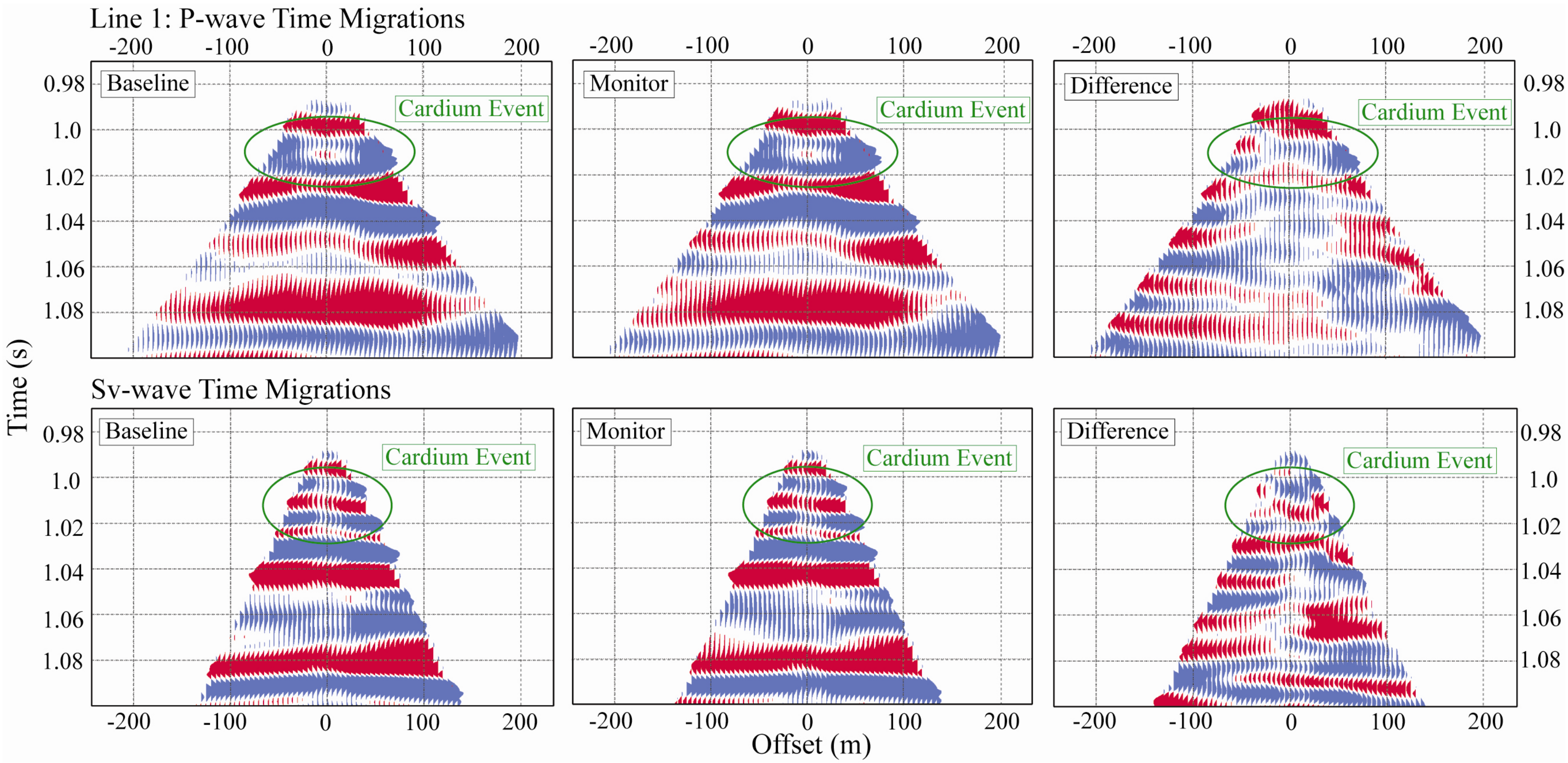

Figure 5.17: Baseline and monitor survey time migrated images and difference displays for the P- and Sv-wave data from Line 1. In this case, the amplitude anomaly is clearer on the Sv-wave difference display. The difference display amplitudes are scaled up three times from the baseline and monitor displays.

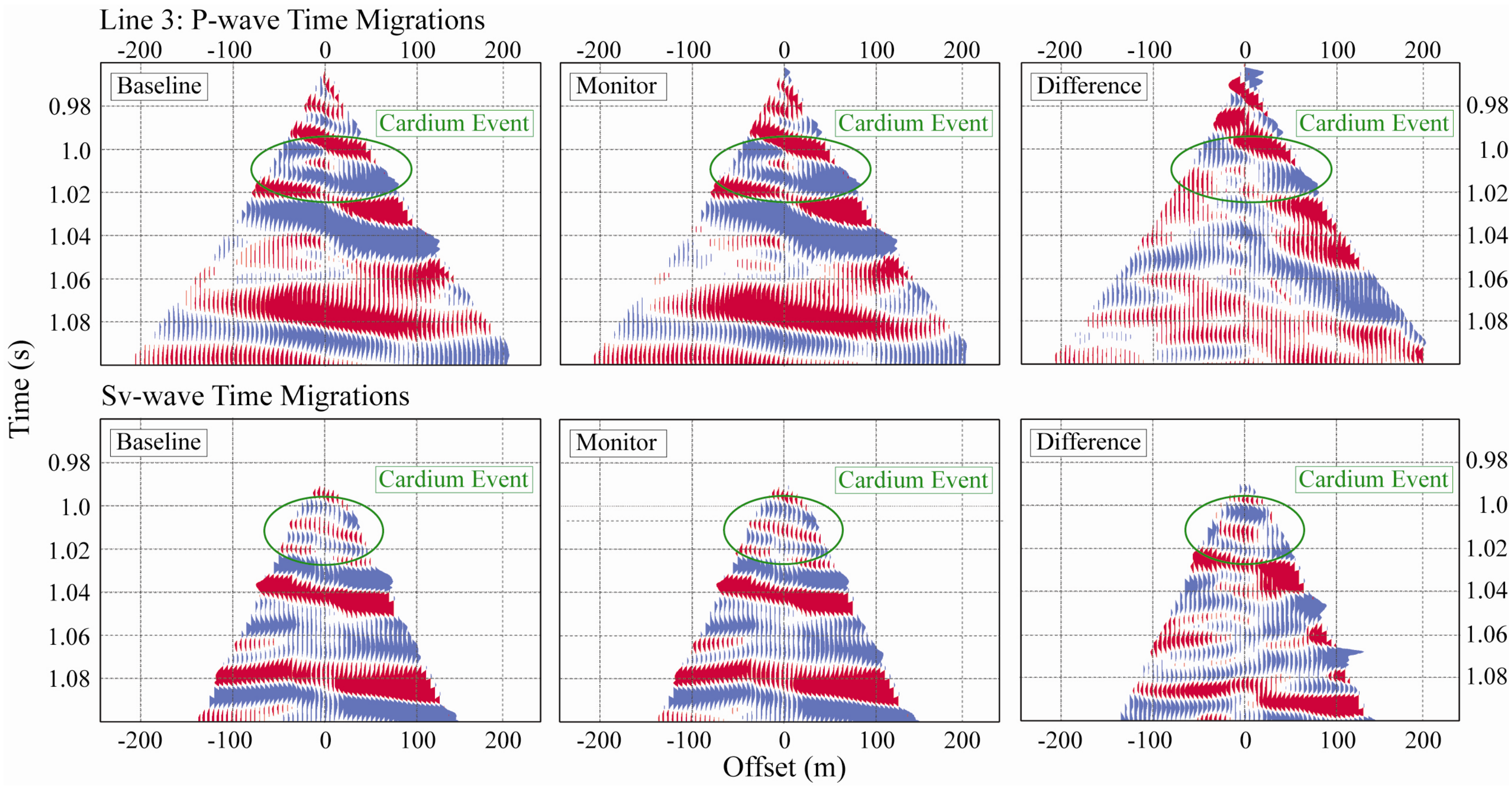

Figure 5.18: Baseline and monitor survey time migrated images and difference displays for the P- and Sv-wave data from Line 3. The difference display amplitudes are scaled up three times from the baseline and monitor displays.

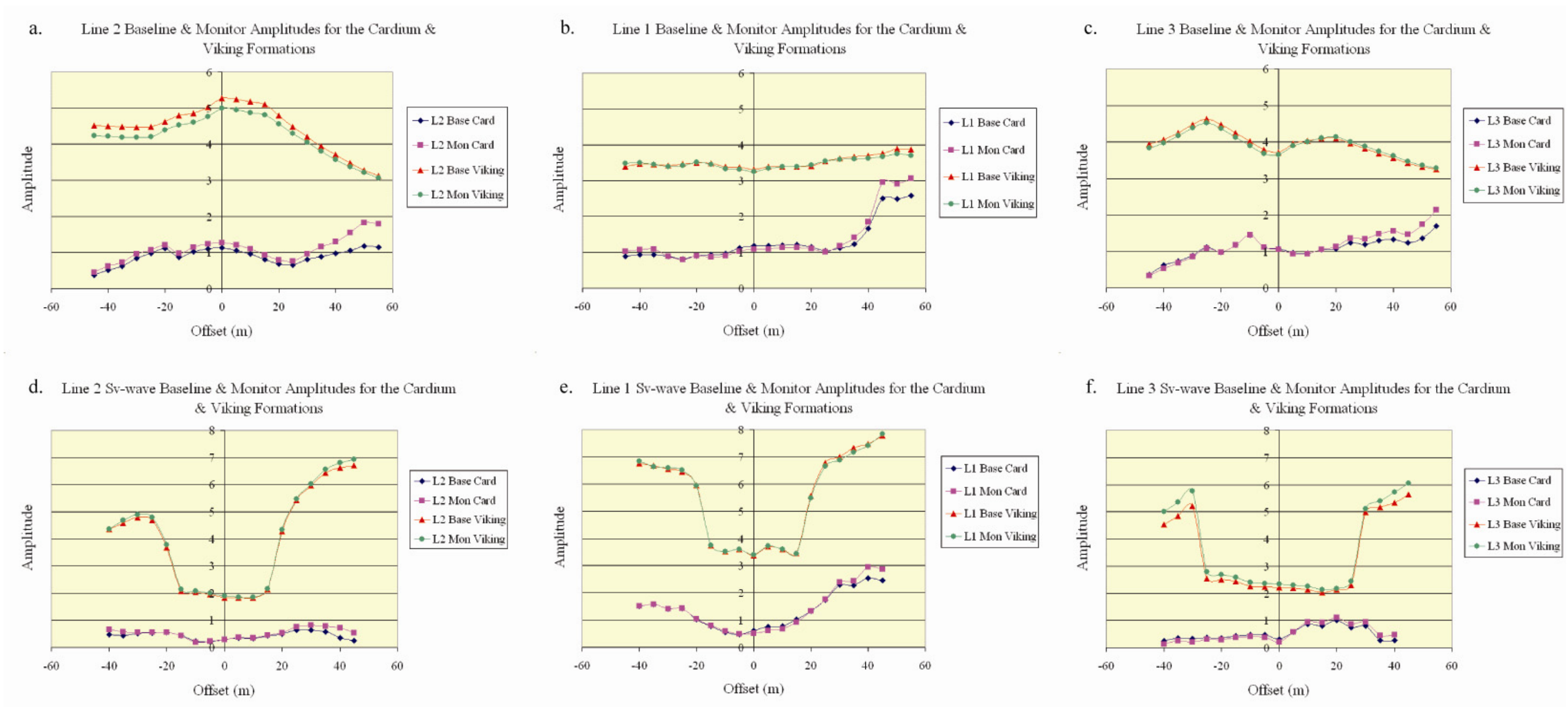

Figure 5.19: Comparison of the amplitudes from the baseline and monitor surveys for the Cardium and Viking events.

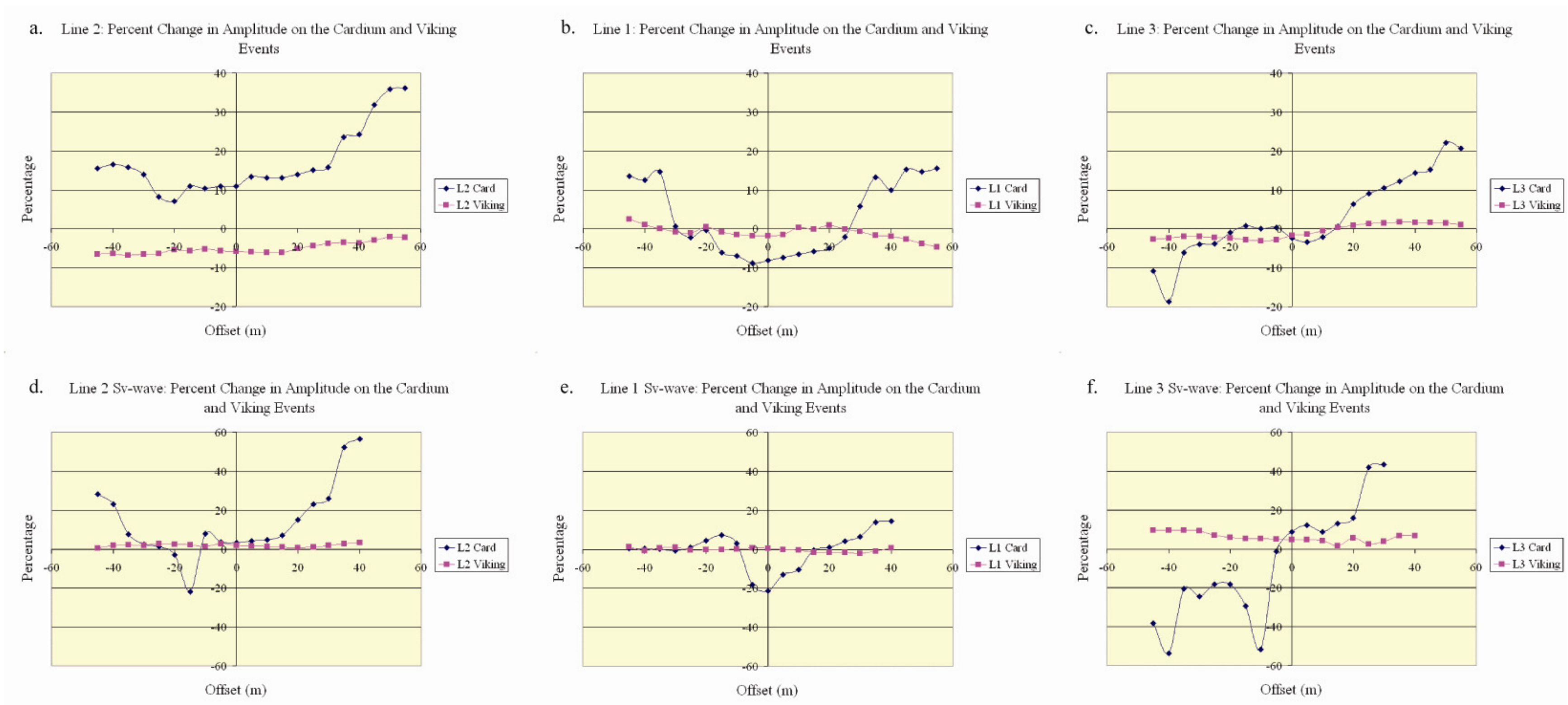

Figure 5.20: Percentage change in amplitudes from the baseline to the monitor survey for the Cardium and Viking events. In most cases, the percentage change in amplitude on the Cardium event is much larger than the change on the Viking event.

5.3.6 Discussion

The observed increase in amplitudes in the P-wave images at the Cardium event on Line 2, the north end of Line 1, and the east end of Line 3 suggest that the CO_2 is flowing southwest from the injector wells along the NE-SW fracture trend in the region (Figure 5.21). The monitor well is located about 400 m away from the closest CO_2 injector. Based on the time-lapse VSP data results, in the eight months between the baseline and monitor surveys the CO_2 has progress about 380 m towards the monitor well at a rate of about 47.5 m a month. At the Weyburn Project, CO_2 has progressed through the reservoir at a rate of about 15 to 20 m a month. The permeability of the Marly Formation is about 10 md (Li, 2003). This is comparable to the original permeabilities of the Cardium Formation sandstones which are estimated to be between 2 to 17 md. It is possible that the Cardium Formation sandstones have higher fracture densities and permeabilities than the Marly Formation due hydro-fracture of the reservoir. Alternately, the high flow rate may be an indication that the CO_2 has entered the conglomerate layer in the Pembina River Member, as this layer has an estimated permeability of 160 md (Krause et al., 1987).

The Sv-wave migrated images show changes in amplitude and small time shifts between the baseline and monitor surveys. The Sv-wave migrated images from Lines 2 and 3 show that there has been an increase in amplitude on the east end of each line. The time shifts measured on the Sv-wave migrated images from these two lines may be the result of an expanding pressure front related the CO_2 flood. Based on Equation 3.2 in Chapter 3, the shear modulus should not be affected by the fluid composition of the formation. However, the Sv-wave data suggests that shear modulus is being affected by the injected CO_2 at the Penn West site, so the Gassmann modelling may not be providing accurate predictions for this reservoir. As discussed in Section 3.2.1, the inject CO_2 may be reacting with minerals in the reservoir to produce a softening effect that impacts the shear modulus of the reservoir.

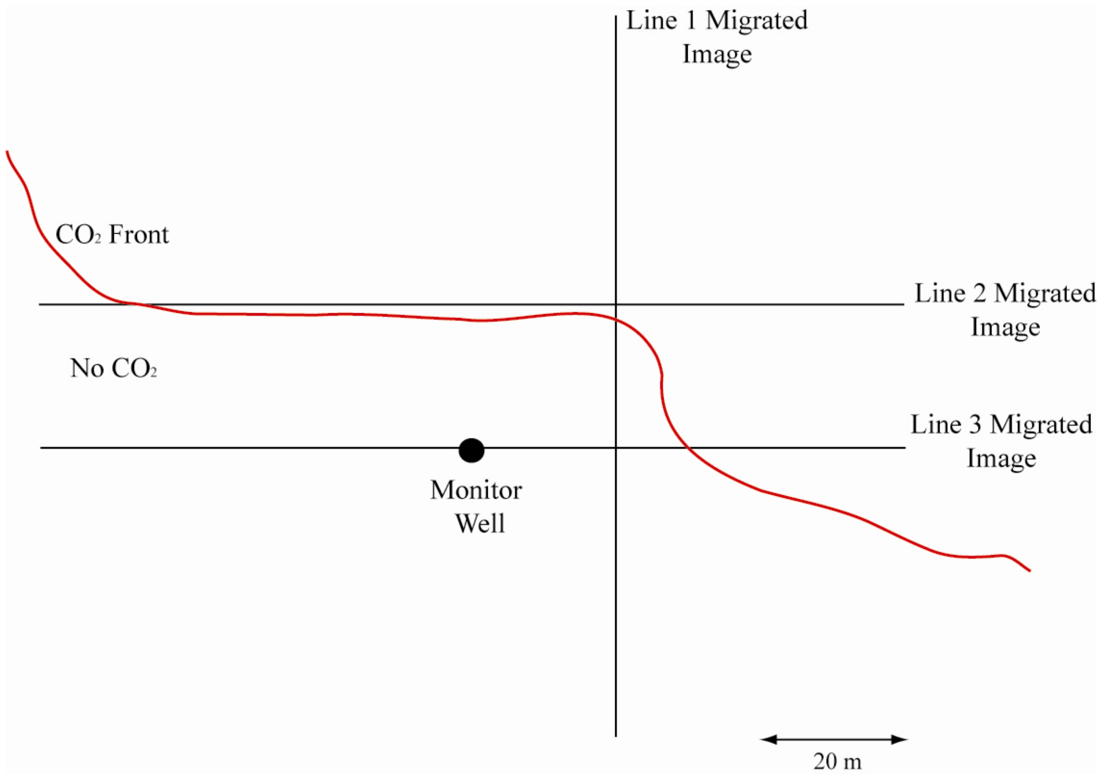

Figure 5.21: The leading edge of the CO_2 front at the time of the monitor survey based on the time-lapse VSP results. The CO_2 front is likely moving along the NE-SW fracture trend in the formation.

The increase in traveltimes measured by the crosscorrelations is small; however, they are on the same order as the time shifts measured by other researchers working with VSP data (Section 3.3.4). The measured time shifts are also similar to those predicted with Gassmann modelling. The modelling predicts that a 10% saturation of CO_2 should cause a decrease in P-wave velocities of about 5% and result in time shifts of less than 1 ms (Chen, 2006).

Overall, comparisons of the baseline and monitor survey data show the high degree of similarity of the seismic traces at several points in the processing flow. The amplitude and phase spectra of the baseline and monitor surveys are nearly identical. The repeatability metrics demonstrate the VSP data from the permanently emplaced receivers is highly repeatable. The percentage changes in amplitudes for the Cardium event are significantly higher than the Viking event. These facts indicate that the differences identified in the data at the Cardium event are true time-lapse changes caused by the injected CO_2.

It is expected that greater time-lapse effects will be observed when the next time-lapse survey is acquired because of the increase in volume of the CO_2 in the reservoir. The next survey is due to be acquired in March 2007.

Chapter Six: Conclusions and Future Work

6.1 Conclusions

6.1.1 Non-repeated Shots

- The data example and finite difference modelling from Line 2 illustrate the importance of source repeatability in time-lapse surveys. Ideally, all of the shot locations should be repeated from survey to survey; however, there will probably always be a certain number of non-repeated shots between surveys. Non-repeated shots must be removed from the processing flow prior to migration of the data because the changes caused by the non-repeated shots may overwhelm the subtle differences that the time-lapse surveys are attempting to identify.

- Source repeatability is particularly important for VSP surveys because VSP datasets tend be much smaller than surface seismic datasets, and the effect of the non-repeated shots is more noticeable.

6.1.2 Data Comparisons and Repeatability Metrics

- Overall, comparisons between the baseline and monitor survey data show a high degree of similarity at multiple points in the processing flow.

- The amplitude and phase spectra of the baseline and monitor surveys are nearly identical.

- Comparisons of the percentage change in amplitude show that the percentage change in amplitude has been minimal for the Viking event (below 5%) and significant for the Cardium event (10 – 35%).

- The repeatability metrics, NRMS and predictability, indicate that the data from the permanently emplaced receivers is highly repeatable. The results for NRMS and predictability for all of the P-wave time migrated images were below 15% and above 99% respectively for most of the dataset.

- The excellent repeatability metrics suggested that cross-equalization would not have a large effect on the P-wave time migrated images. Nonetheless, the monitor survey data was cross-equalized to match the baseline survey data on Line 2. The resulting difference display showed an incremental improvement in the trace range from 100 to 150. The improvements correlated to the changes seen in the NRMS and predictability metrics after cross-equalization.

- The similarity of the dataset, the amplitude and phase spectra, percentage change in amplitude, and the repeatability metrics confirm that the changes that have been identified at the Cardium event are true time-lapse changes caused by the injected CO_2.

6.1.3 Time-lapse Results

- The observed increase in amplitudes in the P- and Sv-wave images at the Cardium event on Line 2, the north end of Line 1, and east end of Line 3 suggest that the CO_2 is flowing southwest from the injector wells along the dominant fracture trend (NE-SW) in the region. Based on the time-lapse results the CO_2 is moving at a rate of about 47.5 m per month.

- The time shifts measured across the base of the Cardium event on the migrated P-wave datasets support the interpretation that the CO_2 is moving SW towards the monitor well. The crosscorrelations across the base of the Cardium event on Line 2 show a systematic increase in traveltimes of 0.2 ms while the crosscorrelations on Line 1 show a traveltime increase of 0.2 ms at the north end of the line that decreases to 0 ms just south of the monitor well. The measured time shifts are on the order of that predicted by modelling with the Gassmann equations, which show that a 10% saturation of CO_2 should cause a decrease in V_p of about 5% and result in time shifts of less than 1 ms (Chen, 2006).

- The time shifts on the Sv-images are less consistent than those observed on the P-wave images. The time shifts on Line 2 ranged between 0.1 and 0.4 ms, and the time shifts on Line 3 were 0.2 ms at the east end of the line decreasing to 0 at the monitor well. Sv-wave data is more sensitive to pressure changes than P-wave data, so it is possible that the Sv-wave data on Line 3 has detected the expanding pressure front related to the injected CO_2. On Line 1, the Sv-wave data does not show a consistent time shift.

- The Gassmann equation presented in Equation 3.2 indicates that the shear modulus should not be affected by fluids in the formation. However, the amplitude changes and time shifts observed in Sv-wave VSP results suggest that the shear modulus is sensitive to the CO_2 that has been injected into the reservoir.

- It is expected that greater time-lapse effects will be observed when the next time-lapse survey is acquired because of the increase in volume of the CO_2 in the reservoir. The next survey is due to be acquired in March 2007.

Ultimately, the results from the Penn West project have important ramifications for other projects of this type, such as the Otway Basin Pilot Project in Australia (Dodds, et al., 2006). The surface seismic time-lapse surveys did not display any clear time-lapse anomalies related to the CO_2 injection; this may be because the CO_2 has been confined to a thin bed or because the volume of injected CO_2 is still below the level of seismic detectability for this site. To date the VSP data is the only geophysical method that has proved successful in monitoring the CO_2 plume at the Penn West site.

6.2 Future Work

The VSP walkaway dataset acquired for the Penn West CO_2 Pilot Project is a rich dataset that represents a variety of opportunities for future work. A second monitor survey is scheduled to be acquired in March 2007.

- The data from the monitor surveys could be used to assess the effects of processing on the repeatability metrics. Several authors have found that processing can improve the repeatability of seismic data (Eiken et al., 1999; Calvert, 2005). NRMS and predictability should be calculated after each point in the processing flow to determine how each stage of the processing flow affects data repeatability.

- A number of the parameters obtained from the VSP processing can be used to re-process the surface seismic. For example, information from the anisotropic velocity model could be incorporated into the surface seismic processing and may result in an improved surface seismic image.

- These datasets also present a number of opportunities to study anisotropy. The data from Line 3 was used to analyze for anisotropy because that was the line that ran closest to the monitor well. The anisotropic inversion also assumed VTI media. The multi-offset VSP data offers an excellent chance to analyze for azimuthal anisotropy. The data could also be examined for shear wave splitting.

- Finally, S-wave polarization vectors and anisotropy have been observed to change over time as CO_2 was injected into a reservoir in the Central Vacuum Field in New Mexico (Davis and Roche, 2006). The data from all three of the surveys should be analyzed to see if a similar effect can be identified at the Penn West site.

References

Alberta Energy and Utilities Board, 2002, Table of Formations, Alberta: http://www.eub.ca/portal/server.pt/gateway/PTARGS_0_212_1730905_0_0_18/

Arts, R., and P. Winthaegen, 2005, Monitoring Options for CO_2 Storage. In Carbon Dioxide Capture for Storage in Deep Geologic Formations, Volume 2. Eds. D.C. Thomas and S.M. Benson. Amsterdam: Elsevier, 2005.1001-1013.

Backus, G., 1962, Long-wave elastic anisotropy produced by horizontal layering: Journal of Geophysical Research, 67: 4427-4440.

Bachu, S., 2002, Sequestration of CO_2 in geologic media in response to climate change: road map for site selection using the transform of the geological space into the CO_2 phase space: Energy Conservation and Management, 43: 277-289.

Bachu, S., and J.C. Shaw, 2005, CO_2 storage in oil and gas reservoirs in Western Canada: effect of aquifers, potential for CO_2-Flood enhanced oil recovery and practical capacity: In 7th International Conference on Greenhouse Gas Technologies. Eds. E.S. Rubin, D.W. Keith, C.F. Gilboy. Amsterdam: Elsevier; Vol. 1, 361-69.

Bell, J.S. and S. Bachu, 2003, In situ stress magnitude and orientation estimates for Cretaceous coal-breaing strata beneath the plains area of central and southern Alberta: Bulletin of Canadian Petroleum Geology, 51; 1: 1-28.

Benson, S.M., 2005, Overview of Geologic Storage of CO_2. In Carbon Dioxide Capture for Storage in Deep Geologic Formations, Volume 2. Eds. D.C. Thomas and S.M. Benson. Amsterdam: Elsevier, 2005. 665-671.

Carrion, P., J. Costa, J.E.F. Pinheiro, and M. Schoenberg, 1992, Short Note: Cross-borehole tomography in anisotropic media: Geophysics, 57; 9: 1194-1198.

Chadwick, R.A., P. Zweigel, U. Gregersen, G.A. Kirby, S. Holloway, and P.N. Johannessen, 2003, Geological Characterization of CO_2 Storage Sites: Lessons from Sleipner, Northern North Sea: In 6th International Conference on Greenhouse Gas Technologies. Eds. J. Gale and Y. Kaya. Amsterdam: Pergamon.

Chadwick, R.A., D. Noy, E. Lindeberg, R. Arts, O. Eiken, and G. Williams, 2006, Calibrating reservoir performance with time-lapse seismic monitoring and flow simulations of the Sleipner CO_2 plume: 8th International Conference on Greenhouse Gas Control Technologies, Trondheim, Norway, June 19-22.

Chen, F, 2006, Interpretation of Time-lapse Surface Seismic Data at a CO_2 Injection Site, Violet Grove Alberta. Calgary: unpublished Msc. Thesis, University of Calgary.

Dahowski, R. and S. Bachu, 2006, Timing of reservoir availability and impacts on CO_2 storage in the Alberta Basin, Canada: 8th International Conference on Greenhouse Gas Control Technologies, Trondheim, Norway, June 19-22.

Daley, T.M., L.R. Myer, G.M. Hoversten, and J.E. Peterson, 2006, Borehole Seismic Monitoring of Injected CO_2 at the Frio Site: 8th International Conference on Greenhouse Gas Control Technologies, Trondheim, Norway, June 19-22.

Davis, T., and S. Roche, 2006, Time-lapse, Multicomponent Seismology – Application to Dynamic Reservoir Characterization. Tulsa: SEG 2006 Short Course.

Dodds, K., D. Sherlock, M. Urosevic, D. Ethridge, D. de Vries, S. Sharma, 2006, Developing a Monitoring and Verification Scheme for a Pilot Project, Otway Basin, Australia: 8th International Conference on Greenhouse Gas Control Technologies, Trondheim, Norway, June 19-22.

Ebrom, D., D. Buddery, G. Watts, and B. Taylor, 2006, Monitoring Activities at In Salah: 8th International Conference on Greenhouse Gas Control Technologies, Trondheim, Norway, June 19-22.

Eiken, O., P. Waldemar, M. Schonewille, G. Haugen, and A. Duijndam, 1999, A proven concept for acquiring highly repeatable towed streamer data: 61st Conf. & Tech. Exhib. EAGE, Expanded Abstracts, 1-40.

Forgues, E., J. Meunier, FX. Grésillon, C. Hubans, and D. Druesne, 2006, Continuous High-Resolution Seismic Monitoring of SAGD: 76th Ann. Internat. Mtg., Soc. Of Expl. Geophys., Expanded Abstracts, 3165-3169.

Gardner, G.H.F., L.W. Gardner, and A.R.Gregory, 1974, Formation Velocity and Density – The Diagnostic Basics for Stratigraphic Traps: Geophysics, 39; 6: 770-780.

Gulati, J.S., R.R. Stewart, J.M. Parkin, 2004, Analyzing three-component 3D vertical seismic profiling data: Geophysics, 69; 2: 386-392.

Hatchell, P., and S. Bourne, 2005, Rocks under strain: Strain-induced time-lapse time shifts are observed for depleting reservoirs: The Leading Edge, 24: 1222-1225.

Hornby, B.E., L.M. Schwartz, and J.A. Hudson, 1994, Anisotropic effective-medium modeling of the elastic properties of shales: Geophysics, 59; 10: 1570-1583.

Horne, S., and W.S. Leaney, 2000, Short Note: Polarization and slowness component inversion for TI anisotropy: Geophysical Prospecting, 48: 779-788.

Hoversten, G.M., E. Gasperikova, and S.M. Benson, 2006, Theoretical Limits for Seismic Detection of Small Accumulations of Carbon Dioxide in the Subsurface: 8th International Conference on Greenhouse Gas Control Technologies, Trondheim, Norway, June 19-22.

IEA Greenhouse Gas R & D Programme, 2001, Putting Carbon Back Into The Ground, J. Davison, P. Freund, and A. Smith, 32 pp.

Jammes, L., 2006, Logging techniques for CO_2 Saturation and well integrity evaluation: 3rd Monitoring Network Meeting, IEA GHG R&D Programme, Melbourne, Australia, October 30 – November 2, 2006.

Johnston, D., and M. Terrell, 2006, 4D Seismic Analysis and Interpretation. Tulsa: SEG 2006 Short Course.

Jones, L.E.A., and H.F. Wang, 1981, Ultrasonic velocities in Cretaceous shales from the Williston basin: Geophysics, 46; 3: 288-297.

Kaarsberg, E.A., 1959, Introductory studies of natural and artificial argillaceous aggregates by sound-propagation and x-ray diffractions methods: J. Geology, 67: 447-472.

Koster, K., P. Gabriels, M. Hartung, J. Verbeek, G. Deinum, and R. Staples, 2000, Time-lapse seismic surveys in the North Sea and their business impact: The Leading Edge, 19: 286-293.

Kragh, E., and P. Christie, 2002, Seismic repeatability, normalized rms, and predictability: The Leading Edge, 21: 640-647.

Krause, F.F., H.N. Collins, D.A. Nelson, S.D.Machemer, and P.R. French, 1987, Multiscale Anatomy of a Reservoir: Geological Characterization of Pembina-Cardium Pool, West-Central Alberta, Canada: The American Association of Petroleum Geologists Bulletin, 71; 10: 1233-1260.

Kristiansen, P., P. Christie, J. Bouska, A. O'Donovan, P. Westwater, and E. Thorogood, 2000, Foinaven 4D: processing and analysis of two designer 4Ds: 70th Ann. Internat. Mtg., Soc. Of Expl. Geophys., Expanded Abstracts, 1456-1459.

Landrø, M., 1999, Repeatability issues of 3-D VSP data: Geophysics, 64; 6: 1673-1679.

Landrø, M., P. Digranes, and L.K. Strønen, 2005, Pressure depletion measured by time-lapse VSP: The Leading Edge, 24: 1226-1232.

Leaney, W.S., 1994, Anisotropy and AVO from walkaways: 64th Ann. Internat. Mtg., Soc. Expl. Geophys., Expanded Abstracts, 105-109.

Leaney, W. S., 2002, Anisotropic vector plane wave decomposition of 3D VSP Data: 72nd Ann. Internat. Mtg., Soc. Expl. Geophys., Expanded Abstracts, 2369-2372.

Leaney, W. S. P., and C. Esmersoy, 1989, Parametric decomposition of offset VSP wave fields: 59th Ann. Internat. Mtg., Soc. Of Expl. Geophys., Expanded Abstracts, 1097-1100.

Li, G., 2003, 4D seismic monitoring of CO_2 flood in a thin fractured carbonate reservoir: The Leading Edge, 22; 7: 690-695.

Lindsay, R. and R. Van Koughnet, 2001, Sequential Backus Averaging: Upscaling well logs to seismic wavelengths: The Leading Edge, 20: 188-191.

MacBeth, C., and H.B. Lynn, 2000, Applied Seismic Anisotropy: Theory, Background, and Field Studies. Ed. C. MacBeth and H.B. Lynn. Series Ed. D.A. Ebrom. Tulsa: Society of Exploration Geophysicists.

Majer, E.L., T.M. Daley, V. Korneev, D. Cox, J.E.Peterson, and J.H. Queen, 2006, Cost-effective imaging of CO_2 injection with borehole seismic methods: The Leading Edge, 25: 1290-1302.

Meunier, J., F. Huguet, and P. Meynier, 2000, Reservoir Monitoring using Permanent Sources and Vertical Receiver Antennae: 70th Ann. Internat. Mtg., Soc. Of Expl. Geophys., Expanded Abstracts, 1619-1622.

O'Brien, J., F. Kilbride, and F. Lim, 2004, Time-lapse VSP reservoir monitoring. The Leading Edge, 23; 11: 1178-1184.

Sayers, C.M., 1997, Determination of anisotropic velocity models from walkaway VSP data acquired in the presence of dip: Geophysics, 62; 3: 723-729.

Schoenberg, M.A., and M.V. de Hoop, 2000, Approximate dispersion relations for qP-qSV-waves in transversely isotropic media: Geophysics, 65; 3: 919-933.

Schütt, H., M. Wigand, and E. Spangenberg, 2005, Geophysical and geochemical Effects of Supercritical CO_2 on Sandstones. In Carbon Dioxide Capture for Storage in Deep Geologic Formations, Volume 2. Eds. D.C. Thomas and S.M. Benson. Amsterdam: Elsevier, 2005.767-786.

Smit, F., M. Ligtendag, P. Wills, and R. Calvert, 2005, Permanent seismic reservoir monitoring using the sparse OBC concept: 75th Ann. Internat. Mtg., Soc. Of Expl. Geophys., Expanded Abstracts, 2402-2405.

Tcherkashnev, S. and W.S. Leaney. Avolog Manual. Gatwick: Internal Schlumberger Publication, 2002.

Terrell, M.J., T.L. Davis, L. Brown, and R. Fuck, 2002, Seismic monitoring of a CO_2 flood at Weyburn field, Saskatchewan, Canada: demonstrating the robustness of time-lapse seismology: 72nd Ann. Internat. Mtg., Soc. Of Expl. Geophys., Expanded Abstracts, 1673-1676.

Thomsen, L, 1986, Weak elastic anisotropy: Geophysics, 51; 10: 1954-1966.

Thomsen, L, 2002, Understanding Seismic Anisotropy in Exploration and Exploitation. Tulsa: SEG 2002 Distinguished Instructor Short Course.

Tura, A., T. Barker, P. Cattermole, C. Collins, J. Davis, P. Hatchell, K. Koster, P. Schutjens, and P. Wills, 2005, Monitoring primary depletion reservoirs using amplitudes and time shifts from high-repeat seismic surveys: The Leading Edge, 24: 1214-1221.

Vernik, L., and X. Liu, 1997, Velocity anisotropy in shales: A petrophysical study: Geophysics, 62; 2: 521-532.

Vernik, L., and A. Nur, 1992, Ultrasonic velocity and anisotropy of hydrocarbon source rocks: Geophysics, 57; 5: 727-735.

Wang, Z., 2001, Fundamentals of seismic rock physics: Geophysics, 66; 2: 398-412.

White, D.J., K. Hirsche, T. Davis, I. Hutcheon, R. Adair, G. Burrowes, S. Graham, R. Bencini, E. Majer, and S.C. Maxwell, 2004, Theme 2: Prediction, Monitoring, and Verification of CO_2 Movements. In IEA GHG Weyburn CO_2 Monitoring & Storage Project Summary Report 2000-2004. Eds. M. Wilson and M. Monea. Regina: Petroleum Technology Research Centre, 2004. 73-148.

Whittaker, S., B. Rostron, D. Khan, Z. Hajnal, H. Qing, L. Penner, H. Maathuis, and S. Goussev, 2004, Theme 1: Geological Characterization. In IEA GHG Weyburn CO_2 Monitoring & Storage Project Summary Report 2000-2004. Eds. M. Wilson and M. Monea. Regina: Petroleum Technology Research Centre, 2004. 15-69.

Winterstein, D.F., 1990, Velocity anisotropy terminology for geophysicists: Geophysics, 55; 8: 1070-1088.

Winterstein, D.F., and B.N.P. Paulsson, 1990, Velocity anisotropy in shale determined from crosshole seismic and vertical seismic profile data: Geophysics, 55; 4: 470-479.

Yilmaz, Ö. Seismic Data Analysis: Processing, Inversion, and Interpretation of Seismic Data. Tulsa: Society of Exploration Geophysicists, 2001.